Soliton dynamics in fiber lasers : from dissipative soliton to dissipative soliton resonance

Georges Semaan

UNIVERSITE BRETAGNE LOIRE

université angers

Thèse de Doctorat

Georges SEMAAN

Mémoire présenté en vue de l'obtention du
grade de Docteur de l'Université d'Angers
sous le sceau de l'Université Bretagne Loire

École doctorale: *ED-3MPL*

Discipline: *30 – Milieux dilués et Optique*
Spécialité: *Physique*
Unité de recherche: *LphiA- EA 4464*

Soutenue le *17-11-2017*
Thèse N°: *(10)*

Soliton dynamics in fiber lasers:

From dissipative solitons to dissipative soliton resonance

JURY

Rapporteurs :	**M. Guy Millot**, Professeur, Université de Bourgogne **M. Pascal Besnard**, Professeur, Université de Rennes I
Examinateurs :	**M. Benoit Boulanger,** Professeur, Université de Grenoble **M. Andrey Komarov**, Docteur ès Sciences, Université de Novosibirsk
Directeur de Thèse :	**M. François Sanchez**, Professeur, Université d'Angers
Co-encadrant de Thèse :	**M. Mohamed Salhi**, MCF, Université d'Angers

"Τα άτομα και το κενό είναι η αρχή των πάντων και τα υπόλοιπα είναι κατασκευάσματα του νου"

"Nothing exists except atoms and empty space, everything else is just opinion"

Democritus

To my wife, Χριστίνα

Acknowledgements

The last 3 years during which I was enrolled as a PhD student and working at the Laboratoire de Photonique d'Angers were a blast. Scientifically speaking, I explored new aspects of physics especially in optics, that I was never exposed to before. On a social scale, this adventure allowed to meet new people with different perspectives and to have new friends; friends to keep. This whole combination of circumstances forged me with broader skills at distinct levels and I grew into what I believe to be a plump scientist. It had been a great learning and a challenging experience which I would not be able to achieve without being well surrounded and wisely advised during my studies. Therefore, I would like to express my deepest gratitude to the people who helped and participated in the fulfillment of this thesis.

Firstly, I would like to express my sincere gratitude to my main advisor Prof. François Sanchez for his continuous support, patience, motivation, sense of humor and immense encyclopedic knowledge of the matter. His guidance helped me during my research and writing of this thesis, and his tips and tricks arouse in me a deep sense of curiosity I did not have before. I could not have imagined having a better advisor and mentor for my Ph.D. study, and a better person when needed the most.

I am also thankful to Dr. Mohamed Salhi my second advisor. He supported this work, advised me on experimental and theoretical issues and provided all the help needed when problems occurred. I would like to thank him for the various discussions we had in the office we shared, no matter what the subject was. Being an easy-going person, he made me feel comfortable in tackling the issues I was facing, knowing that I would rely on his expertise.

Besides my advisors, I would like to thank the rest of my thesis committee: Prof. Guy Millot, Prof. Pascal Besnard, Prof. Benoit Boulanger and Dr. Andrey Komarov, for their insightful comments and remarks which incented me to widen my research from various perspectives. Dr. Andrey Komarov represents a very important part of this thesis. He helped in the numerical and analytical assessments and has offered his experience and knowledge to make my experiments more complete.

My sincere thanks also go to Dr. Alioune Niang, who helped me from the very first days in understanding the subject and the instruments and provided with all the information needed to succeed. He has been a good friend and without his precious support, it would not be possible to conduct this research.

My deepest gratitude goes to the technical team at the Physics Department (Christophe Cassagne, Leo Monnereau, Alain Mahot, Dominique Guichaoua, and Christian Auguste). They provided all the help and effort needed for the success of this research.

I thank my fellow lab mates for the stimulating discussions and for all the fun we had in the last three years. Special dedications to Dr. Valentin Besse who was my first officemate, Dr. Julien Merigeon with whom we reviewed the history of France and the social problems in our community, Dr. Ariadni Kerasidou one of my closest friends who knew how to make the days go smoother, Dr. Khmaies Guesmi, PhD student Fatma Ben Braham and Paul Mouchel who provided technical expertise and different components used in this research. Also, I thank Prof. Zhi Chao Luo for the optical tapers from China. I may not remember everyone but know that you have collaborated to the success of this thesis in your own way.

I am indebted to my family for all the sacrifices they had to do and for their continuous and unconditional support. Thank you so much.

Finally, I would like to thank my wife for having faith in me, supporting me and proving me that I am always wrong when it comes to general discussions.

Table of contents

List of Figures

Abbreviations

BP: Black Phosphorus

CGLE: Complex Ginzburg Landau Equation

CNT: Carbon nanotubes

DCF: Double Clad fiber

DSF: Dispersion shifted fiber

DSR: Dissipative soliton resonance

Er: Erbium

FWHM: Full width at half maximum

FWM: Four wave mixing

F8L: Figure of eight laser

GSA: Graphene saturable absorber

GVD: Group velocity dispersion

HML: Harmonic mode-lock

LMA: Large mode area

MF: Microfiber

NALM: Nonlinear amplified loop mirror

NLSE: Nonlinear Schrödinger equation

NOLM: Nonlinear optical loop mirror

NPE: Nonlinear polarization evolution

NPR: Nonlinear polarization rotation

PC: Polarization controllers

PCF: Photonic crystal fiber

PI-ISO: Polarization insensitive isolator

PS-ISO: Polarization sensitive isolator

SA: Saturable absorber

SBS: Stimulated Brillouin scattering

SMF: Single mode fiber

SPM: Self phase modulation

SRS: Stimulated Raman scattering

SWP: Square wave pulse

TISA: Topological insulator saturable absorber

XPM: Cross phase modulation

YB: Ytterbium

Chapter 1 Introduction

1.1 A historical background

Lasers are intense beams of electromagnetic radiation travelling in a specific direction. That said, the defining properties of lasers are that the light waves are coherent, and they are of one wavelength described as monochromatic. By harnessing these properties in a device that reflects the light back and forth through a special material, it is possible to generate an amplified light source.

The first experimental demonstration of the laser in the 1960's is one of the most significant technological developments of the modern age. It all started in 1917, when Albert Einstein established the lasing principle through his work on quantum theory. A series of developments over the next decades culminated in Theodore Maiman's demonstration of the first working laser on 16 May 1960 by shining a high-power flash lamp on a ruby rod with silver-coated surfaces [1]. Famously, Maiman's proposal was rejected by *Physical Review Letters*, whose editors judged it as the same work published earlier by Maiman concerning the excitation of ruby with light, with an examination of the relaxation times between quantum states and it is just another episode in the stream of research related to masers [2], led by Charles Townes and others. When the first laser appeared, it was dubbed "a solution looking for a problem", which Townes has said he regarded not as a joke but as a challenge [3]. But by bringing together optics and electronics, several research fields have bloomed in the field of optics and photonics, thus marking the beginning of a new technological era shaped by the control of light, and many different laser types and applications came along.

Lasers have become an enabling technology with diverse applications from medicine to manufacturing, communications to measurements and from research and analysis to domestic entertainment. On a business marketing scale, estimates suggest that the world market for lasers in 2017 alone is worth more than $11.1 billion and that the total number of laser patents issued since its invention is more than 50,000 [4]. It is no exaggeration to say that lasers have been nothing short of revolutionary in almost

60 years of their first demonstration and that without lasers, our modern technological world would be nothing like it is today. In fact, only one year after its invention, the laser was applied in a medical procedure at the Columbia-Presbyterian Hospital where a ruby laser was used to destroy an eye tumor. Today, lasers are common in most medical disciplines, e.g. dermatology, dentistry and eye surgery, because of their ability to deliver high-precision treatments, whilst remaining minimally invasive. Also, measurement and analysis have been transformed by the laser. Lasers are used to mark construction sites, determine the position of targets and to measure distances in outer space. Laser analysis of chemical and physical structures has allowed factories to manage quality control efficiently. Lasers also play a crucial role in the inspection of pharmaceuticals. Lasers can generate extreme pressures and temperatures, and so can be used to ignite nuclear fusion. Research into laser-driven fusion is currently underway and promises to address the increasing demands for energy. In addition, scientists are exploiting lasers in the development of solar cells. Long distance telecommunications and broadband internet both depend on the transmission of light pulses along optical fibers. These light pulses are both generated and relayed via lasers. This revolutionary method of communication is replacing less efficient copper wire-based networks and is the foundation of the internet and information age. Lasers are employed across the manufacturing industry as tools capable of delivering intense cutting or welding power with high precision. Their ability to manipulate and transform materials makes them ideal for the automobile, computers, etc. In fact, it is difficult to find a modern consumer product that has not been shaped by a laser during its manufacturing.

There are many types of lasers available and often described by the kind of lasing medium they use i.e. solid state, dye, excimer, gas or semiconductors. Regardless the medium, lasers are characterized by the duration of the laser emission and are divided into two main categories: continuous wave and pulsed. In the continuous wave, lasers operate with a continuous "free-running" beam power. In most high-power systems, this beam power can be adjusted while in low power lasers, its level is fixed by the design and performance usually degrades with time. While in pulsed

mode, the optical power appears in pulses of a specific duration at a specific repetition rate. There are numerous methods to achieve laser pulsing, but the end-result follows the same principle. From these methods, two are usually distinguished for operating lasers in pulsed mode: Q-switch and mode-lock.

The first proposal for Q-switched pulsed laser was reported by Hellwarth in 1961 [5] and the first demonstration of such generated pulses was achieved in 1963 by McClung and Hellwarth; they presented the emission of nano to microseconds pulses with high energy from ruby by a nitrobenzene Kerr cell modulator [6]. The first indications of mode-locking in lasers appeared in 1963 [7]–[9] and continued with the works of DiDomenico and Hargrove [10], [11] by modulating cavity losses inside the laser, which was called actively "*mode-locked*" lasers. Passive mode-locking with saturable absorber was demonstrated later with Mocker and Collins [12] and DeMaria [13]. It is in this period of mid 1960s that began the production of narrow pulses known as ultrafast pulses by mode-locking in a laser cavity. Meanwhile, optical fibers doped with rare earth ions were being tested as adequate candidates for the amplification medium in the production of lasers, and since optical fibers allow the study of linear and nonlinear effects of the light, while it is propagating inside the laser cavity. Snitzer explored the prospects for laser action from glasses doped with rare earths and demonstrated the first neodymium-glass laser in a millimeter-scale rod with the neodymium glass in a high-index core, making it essentially the first fiber laser [14]. Glass laser developers moved on to thicker rods in quest for higher power, and wouldn't return to fiber lasers for many years, but in 1964, Charles Koester and Snitzer demonstrated the first fiber amplifier, using a spring-shaped coil of fiber slipped around a linear flash lamp as a pump source [15]. This multimode laser delivered few milliwatts of output power at a wavelength of 1 μm. Several difficulties were then encountered during the design of the fiber laser, particularly related to the design of low-loss optical fiber and the pumping efficiency of these fibers. In fact, conventional glass simply couldn't be made transparent enough to carry light far since about 99 percent of its energy was lost by the time it had propagated few meters. Fortunately, Charles Kao predicted that

optical fibers could be made pure enough to carry signals for long distance as he collected and analyzed samples from glassmakers and concluded that the energy loss was mainly due to impurities such as water and minerals, not the basic glass ingredient of silica itself [16]. This led in 1970 to the creation of very long glass fibers by Corning Glass Works, that performed as Kao and Hockham had foreseen. It is with these previous advances in the development of lasers that the first single-mode neodymium doped fiber laser was produced [17] delivering a few milliwatts of output power. Highly doped fiber cores were later made with various rare earth ions such as neodymium, erbium, ytterbium, thulium [18]–[21]. Rare-earth doped fiber lasers confine the cavity light into bendable waveguides, which introduced subsequently compact laser sources. Besides reducing or eliminating complex alignment, waveguiding of the signal and pump also offers very high gain per pass and excellent thermo-optical properties.

1.2 Motivation

A common feature to all mode-locked lasers is the intensity discrimination, which is achieved by the mode-locking mechanism [22]. Such feature, also known as saturable absorption, is the underlying mechanism responsible for passive mode-locking [23]. Saturable absorption can be achieved by a variety of physical mechanisms including nonlinear polarization rotation [24]–[27], nonlinear interferometry [28]–[33], nanomaterial based saturable absorbers [34]–[36], or nonlinear mode-coupling [37], [38].

The possibility of using optical fibers in short-pulse laser devices has motivated research for nearly two decades. Fiber cavities mode-locked by saturable absorbers have become the most reliable and compact sources for robust ultrashort optical pulses. Such fiber lasers offer major practical advantages over solid state configurations. They are relatively cheap, compact, and do not require careful alignment of the optical cavity since the light is contained in a waveguide. This evolution allowed the investigation of a variety of new pulse distributions resulting from the interaction of light and optical fiber. Among several optical pulse formats, optical soliton [39] is a

very stable optical pulse formed from balancing between the anomalous dispersion and the fiber's self-phase modulation (SPM) effect, and between gain and losses. Independent of the mode-locking techniques, it was found that the soliton operation of all lasers exhibited a multiple pulse generation in the laser cavity under increasing pumping power. Different soliton distributions have been presented theoretically [40]–[42] and experimentally [32], [43]–[45] in the field of ultrashort pulse generation. The observation of this collective interaction between solitons in fiber lasers allowed to confirm the universality of solitons regardless the cavity configuration and to demonstrate the possibility of actively controlling their behavior. In fact, Komarov et al. have showed numerically that in the case of a harmonic mode-locked distribution (HML), the spectral position of an existing continuous wave (CW) in the spectrum is a factor of controlling the different nature of interactions between the pulses [46], [47]. It was also confirmed Niang et al. that by externally injecting a CW in a mode-locked fiber laser, the laser is forced to operate under a different regime from the initial state regime [48], [49].

On the other hand, the multiple solitons generation and the soliton energy quantization effect [50] limit the generation of optical pulses with larger pulse energy and narrower pulse width in the lasers. Due to this effect, when the pumping strength of the energy source is increased, the number of pulses increases inside the laser cavity so that the energy of a distinct pulse remains nearly unaffected. The shortening in pulse duration implies a spectral broadening in the Fourier domain, and when the pulse spectrum exceeds the gain of the bandwidth, the pulse becomes unstable. In this case, the single-pulse bifurcates into the next most energetically favorable state of a double-pulse configuration. The number of pulses is proportional to the pumping strength. It was conjectured that the soliton energy quantization could be an intrinsic property of the laser solitons, as solitons formed in a laser are intrinsically dissipative solitons, where the requirement of soliton internal energy balance ultimately determines the energy of a soliton [51]. Recently, new insights into pulse shaping and propagation physics [52], [53] have provided glimpses of order-of-magnitude increases in the pulse energy and peak power in femtosecond fiber lasers. However, the design

and optimization of high-performance fiber lasers is impeded by multi-pulsing instabilities (MPI), which ultimately impose a fundamental limitation on a single mode-locked pulse's energy [54]. Convenient way for circumventing the limitations and drawbacks of complicated configurations emerged with the theoretical predictions of Chang et al. [55], [56] and involved designing the passively mode-locked laser resonator with parameters enabling existence of so called Dissipative Soliton Resonances (DSR) effect. This permits the soliton energy to increase virtually indefinitely, while keeping the amplitude at a constant level and it has been demonstrated experimentally in NPR, figure-of-eight and even with graphene based saturable absorber [57].

1.3 Thesis outline

This manuscript deals with the optics of mode-locked fiber lasers using a variety of configurations and different mode-locking mechanisms at wavelengths in the near infrared range. The principal objectives are multiple: to describe the fundamental principles of mode-locking, to present experimental techniques for the generation of high energy mode-locked pulses employing various mode-locking methods thus proving its universality and finally to present experimental and technical methods in fabricating real saturable absorbers based on nanomaterials capable of generating high power ultrashort pulses in a laser configuration. Thus, this introduction chapter is followed by:

- Chapter 2 begins with a brief overview discussing key attributes of ultrashort laser pulses and some application examples. Then we continue by covering the basic principles of laser mode-locking. The intent is not only to cover one of the most interesting topics at the outset, but to use the discussion on mode-locking as a physical context in which we aim to introduce a variety of important optical effects (e.g., dispersion, filtering, and cross phase modulation).

- In Chapter 3 we discuss the influence of an injected continuous wave pulse on the behavior of the harmonic mode-locked fiber laser. These lasers possess a rich diversity of dynamical regimes that have been demonstrated through the

last decades. Recent experiments on external optical injection of continuous wave have shown the influence of such mechanism on forcing a harmonic distribution operational mode over the dominant self-starting regime. We demonstrate in this chapter that by using the injection method in certain conditions, the stability of the laser is improved.

- In Chapter 4 we focus on high average output power passively mode-locked fiber lasers. It begins with a detailed coverage of optics methods that enable pulse shaping and high average output power fiber laser generation. After defining key concepts regarding the soliton area theorem, the discussion covers the generation of square pulses exploiting the mechanism of dissipative soliton resonance in anomalous dispersion. First, the dissipative soliton resonance is investigated under the nonlinear polarization evolution mechanism of mode-locking, then under the nonlinear amplifying loops mechanism. The effect of cavity coupling ratio and length are investigated to define a set of key parameters that maintain pulse stability. After that, new effects such as multipulsing instabilities arising in dissipative soliton resonances are discussed. By taking advantage of the dissipative soliton resonance regime, we study the spectral dynamics of square pulses and we demonstrate for the first time, experimentally and numerically, the generation of staircase shape pulses generated in fiber lasers.

- In the previous chapters, we discuss the different aspects of pulse generation and pulse stability that can exist in passively mode-locked fiber lasers based on artificial absorbers. Chapter 5 focuses on the manipulation of ultrashort pulses using nanomaterial based saturable absorbers such as graphene and topological insulators. A thorough state of the art is presented as a well-defined introduction to the field of nanomaterials and their potential in mode-locked fiber lasers. Saturable absorbers are explained in detail where the mechanism of saturable absorption is highlighted and the different methods of characterizing the nanomaterials' optical properties are depicted accordingly. Also, deposition techniques of nanomaterials as fiber-based saturable absorbers are introduced and

two main methods are stressed on. Therefore, this chapter takes a two-pronged approach. First, the end-faced based saturable absorber is treated classically where experiment in fiber ring cavity is discussed for illustration. Second, after a necessarily introduction to the importance of optical tapers, experiments and results concerning graphene and topological insulators are presented.

- The final chapter concludes the experimental results presented in this thesis and highlights perspectives and possible development of the work.

Chapter 2 The physics of fiber lasers

The fundamental optical element in this work is the optical fiber, where non-linear optical effects are exploited. Optical fiber was one of the most successful inventions of the twentieth century as it has led to the development of telecommunication and advances in ultrafast technologies.

This chapter gives a general introduction to the field of ultrafast lasers, while emphasizing on mode-locked fiber lasers and the different mechanisms used to generate ultrashort pulses. It presents a well-defined context governed by the physics of propagation in optical fiber and the generation of short pulses.

2.1 Optical fibers

Conventional step-index silica fibers are the most common fiber in use today due to their widespread use in telecommunication networks. The basic concept of such fibers is to clad a core fiber with a lower index dielectric as proposed by van Heel in 1954 [58]. Two years later, the first step-index silica fibers were manufactured showing their potential in the field of telecommunications [59]. In the 1970s, several breakthrough improvements were made to reduce fiber losses. Researchers at Corning developed the predecessor to modified chemical vapor deposition to facilitate losses of less than 20 $dB.km^{-1}$ [60]. One year later, researchers at Bell labs dramatically reduced the fiber loss at 1.55 μm to as low as 0.2 $dB.km^{-1}$ [61], which is very close to the theoretical limit. This discovery led to the commercial deployment of optical fibers for long distance communications and enabled many other fiber-based photonic technologies. The importance and success of optical fibers can be attributed to several excellent properties from which we can mention:

- Extremely low attenuation (due to the use of high purity materials and careful processing) in the C-band (1550 nm).
- Good material properties (chemical stability, resistance and strength).
- Optical confinement over very long distances.
- Compactness (flexibility, ease of being coiled and packaged).

- Environmental robustness (alignment free for all fiber system, less influence of environmental perturbation compared to bulk systems).
- High power handling (low intrinsic nonlinearity of silica).

2.1.1 Basics of electromagnetic waves

From Maxwell's equations, it can be shown that the electric field $\mathbf{E}$ obeys the wave equation:

$$\nabla^2\mathbf{E}(\mathrm{r},\mathrm{t}) - \mu_0\varepsilon_0\frac{\partial^2\mathbf{E}(\mathrm{r},\mathrm{t})}{\partial \mathrm{t}^2} = \mu_0\frac{\partial^2\mathbf{P}(\mathrm{r},\mathrm{t})}{\partial \mathrm{t}^2} \qquad \text{Eq. 1}$$

where $\mathbf{E}$ is the electric field vector and $\mathbf{P}$ is the induced electric polarization. μ_0 is the permeability of free space and ε_0 is the permittivity of free space. The time varying polarization drives the electric field. For a linear propagation, the relation between $\mathbf{P}$ and $\mathbf{E}$ can be written as:

$$\mathbf{P} = \varepsilon_0\chi_\mathrm{L}\mathbf{E} \qquad \text{Eq. 2}$$

where χ_L is the linear susceptibility. In linear medium, χ_L can be expressed using the following:

$$\varepsilon_\mathrm{r} = 1+\chi_\mathrm{L} \qquad \text{Eq. 3}$$

where ε_r is defined as the relative permittivity. The refractive index of a material n is given by:

$$n = \sqrt{\varepsilon_r} = \sqrt{1+\chi_L} \qquad \text{Eq. 4}$$

The real part of n defines the magnitude of the propagation vector k, expressed as $k = n/\omega c$ while the imaginary part gives rise to the attenuation of the field.

2.1.2 Principle of waveguiding

The guidance mechanism of the light beam through an optical fiber (step-index) takes place because of the total internal reflection at the core cladding interface as shown in **Figure 2:1**.

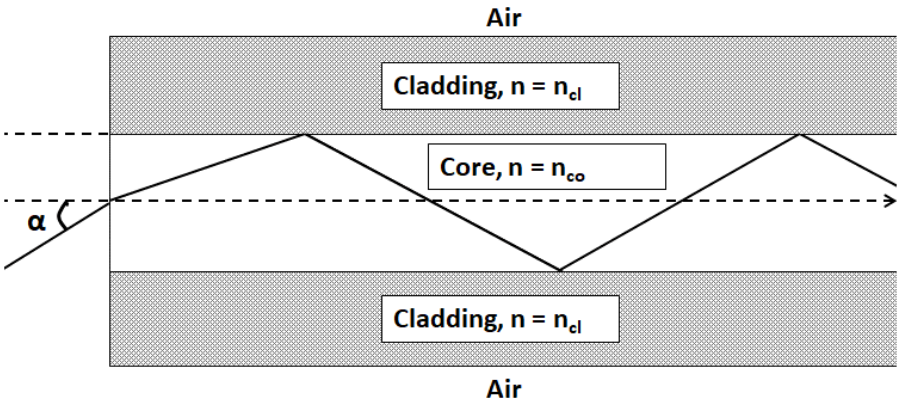

Figure 2:1. Light guidance in a step-index optical fiber under total internal reflection.

The numerical aperture NA characterizing the range of angles the fiber can accept, is determined by the refractive contrast between the core and the cladding and given by:

$$NA = \sqrt{n_{co}^2 - n_{cl}^2} = sin(\alpha) \qquad \text{Eq. 5}$$

where n_{co} and n_{cl} are the refractive indexes of the doped core and the cladding respectively, and α is the incidence angle. Due to the axial invariance of optical fiber, the electric and magnetic field for a given frequency can be written as:

$$\mathbf{E}(\mathbf{r}, z, t) = \mathbf{E}_m(\mathbf{r}) \exp\left[-\mathbf{i}(\omega t - \beta z)\right] \qquad \text{Eq. 6}$$

$$\mathbf{H}(\mathbf{r}, z, t) = \mathbf{H}_m(\mathbf{r}) \exp\left[-\mathbf{i}(\omega t - \beta z)\right] \qquad \text{Eq. 7}$$

where $\mathbf{E}_m$ is the modal electric field distribution and $\mathbf{H}_m$ is the corresponding magnetic field distribution. The axial position along the fiber is denoted by z . r is the transverse position vector over the cross-section (x, y) and ω is the angular frequency. β is the axial component of the wave vector, known as the fiber propagation constant since it is invariant regardless of transverse and axial position. The magnitude of the wave vector is also constant in any material at $k_0 n$ where n is the local refractive index and $k_0 = \frac{2\pi}{\lambda}$. Hence, the magnitude of the transverse propagation constant is constrained such that:

$$k_t = \sqrt{k_0^2 n^2 - \beta^2} \qquad \text{Eq. 8}$$

where k_t is the perpendicular wave number and n is equal to n_{co} or n_{cl}. It is important to note that the refractive index profile of the fiber at any point must satisfy $n_{cl} \le n(x,y) \le n_{co}$ where n_{co} and n_{cl} are the borders indices. Therefore, β satisfies the condition given by:

$$n_{cl}k_0 \le \beta \le n_{co}k_0 \qquad \text{Eq. 9}$$

In this case, only certain values of the propagation constant are possible, illustrating that the light is guided in the core and the field in the cladding will decay gradually with distance from the core-cladding interface. In addition, the above equation implies that the optical fiber may support multiple solutions, which are known as modes. For a conventional step-index fiber, this can be illustrated using the V parameter. With a given core radius a, the V parameter can be expressed as:

$$V = ak_0\sqrt{(n_{co}^2 - n_{cl}^2)} \qquad \text{Eq. 10}$$

The number of modes increases with the V parameter. For a single mode fiber where only the fundamental mode propagates, it needs to satisfy the condition $V < 2.405$. From this, the cut-off wavelength of a single mode fiber can be calculated. Typically, single mode fibers have a small core size to wavelength ratio and small refractive index difference between the core and the cladding.

2.1.3 Rare-earth doped fibers

The success of the significant reduction in the loss of standard telecom fiber motivated the development of rare-earth doped gain fibers. By combining the gain of rare-earth ions with tight optical confinement available in the optical fiber, these materials offer an excellent medium to produce compact and efficient devices.

By incorporating a laser ion into the core of an optical fiber, one obtains a unique medium that exhibits both a low propagation loss and a high gain. The greater the optical densities, the higher the probability of encounter between an inverted ion and a single photon, the higher the optical gain [62]. Rare-earth doped fiber lasers have several advantages, which makes them comparable or superior to the bulk lasers,

namely, high pump absorption, thermal advantages and mechanical superiority. Fiber lasers on the other hand, have major limitations when high pulse energies are required due to the long interaction length of fiber, which leads to undesirable nonlinear effects.

2.2 Pulse propagation in optical fibers

When pulses propagate along a fiber, their temporal shapes, spectra and power are influenced by the combination of different phenomena's. To describe the propagation of the electric field envelope, the dominant physical effects must be taken into consideration. It includes dispersion, absorption and nonlinearities. The simplest standard equation used to describe the propagation inside optical fiber is the Nonlinear Schrödinger equation NLSE [63]:

$$i\frac{\partial A}{\partial z}+i\frac{\alpha}{2}A-\frac{\beta_2}{2}\frac{\partial^2 A}{\partial t^2}+\gamma|A|^2A=0 \qquad \text{Eq. 11}$$

A represents the envelope of the field, β_2 is the second order group velocity dispersion parameter, γ is the nonlinear parameter and α is the absorption coefficient. The NLSE equation is derived from Maxwell's equations and adapted to single-mode propagation.

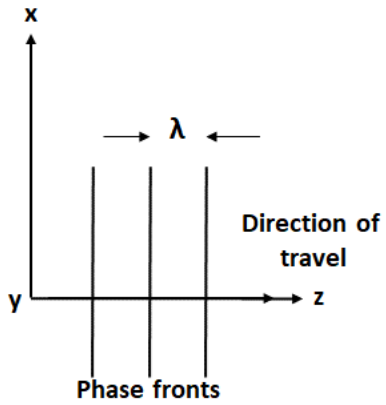

Figure 2:2. Plane wave propagation

The simplest form of solution is a plane wave, whose surfaces of constant phase are infinite planes, perpendicular to the direction of propagation as in Figure 2:2. Clearly, in this case no field quantities can vary with the transverse coordinates x and y; the only spatial variation is caused by changes in the propagation direction z in time. The

envelope of the field A, contains the phase information, which plays a significant role in determining the way a pulse propagates. The second term refers to the fiber loss that will be explained in the section below. The term containing the second derivative with respect to time illustrates the effect of chromatic dispersion, which will cause pulse broadening and the fourth term describes the nonlinear effect which acts to broaden the pulse spectrally.

2.2.1 Absorption

Absorption is an important fiber parameter, which measures power loss between input and output. Given the initial power P_0 launched at the input of a fiber of length L, the transmitted power can be written as:

$$P(\mathrm{L}) = P_0 \exp(-\alpha \mathrm{L}) \qquad \text{Eq. 12}$$

where α denotes the attenuation constant, corresponding to a measured coefficient of total fiber loss. Alternatively, the absorption coefficient can be expressed in a decibel unit (dB.km^{-1}) using the relation:

$$\alpha_{dB} = -\frac{10}{L} log \frac{P(L)}{P_0} = 4.323\alpha \qquad \text{Eq. 13}$$

Fused silica fiber has a transmission over a broadband wavelength range, covering from the ultraviolet absorption edge at 200 nm to an infrared edge at 2500 nm (low attenuation in the range of 500 nm to 2000 nm). For much of the transmission window, losses are dominated by Rayleigh scattering ($\propto \frac{1}{\lambda^4}$), intrinsic material absorption and impurities.

2.2.2 Dispersion

The interaction between an electromagnetic wave and the bound electrons of a dielectric during the propagation in an optical fiber depends on the frequency of the wave. This gives rise to chromatic dispersion, a phenomenon for which the phase velocity of a wave is dependent on its frequency components. Dispersion causes pulse

broadening due to the different phase velocities of the frequency components and if given by:

$$\upsilon_p = \frac{\omega}{k} = \frac{c}{n(\omega)} \qquad \text{Eq. 14}$$

The phase velocity of the propagation wave is υ_p and n is the refractive index of the fiber. For a single mode fiber, the dispersion of a dielectric waveguide mode consists of the material and waveguide dispersion. Material dispersion originates from the frequency-dependent response of a material to incident electromagnetic waves. This can lead to undesired chromatic aberration in an optical component and the separation of different wavelength in a dispersive device. Meanwhile, the waveguide dispersion is related to the geometry of the fiber and occurs due to the propagation of the fundamental mode in both the core and cladding region of a single mode fiber. Given that the mode field distribution is strongly frequency-dependent, the effective mode index varies as a function of the wavelength (frequency).

These effects can be treated separately, when the refractive index difference between the core and the cladding is small [64]. Although it has been shown that the expression is given by:

$$D = D_m + D_\omega \qquad \text{Eq. 15}$$

where D_m and D_ω denote the material and waveguide dispersion respectively. This expression is not quite correct [65] and it is an approximation that is valid in conventional fibers due to the small contribution from waveguide dispersion to the total dispersion of the fundamental mode (LP_{01}). Even a significant percentage error in the waveguide dispersion has little influence.

Mathematically, the effect of dispersion on pulses can be expressed by a Taylor series expansion of the mode propagation constant β about a central frequency ω_0 :

$$\beta(\omega) = k_0 n(\omega) = \sum_{m=0}^{n} \frac{(\omega - \omega_0)^m \beta_m}{m!} \qquad \text{Eq. 16}$$

where

$$\beta(m)=\left(\frac{d^m\beta(\omega)}{d\omega^m}\right)_{\omega=\omega_0} \quad \text{and} \quad m=0,1,2,... \qquad \text{Eq. 17}$$

The first order parameter β_1 is related to the group delay υ_g given by:

$$\beta_1=\frac{1}{\upsilon_g} \qquad \text{Eq. 18}$$

where υ_g describes the overall velocity of the pulse envelope and is inversely proportional to the group index, $\upsilon_g=\frac{c}{n_g}$. Higher order dispersion parameters (e.g. β_3) become particularly significant around the zero-dispersion wavelength ZDW, where the group velocity dispersion GVD is very small. In this case; the dispersion effect is dominated by β_3 , which leads to asymmetric broadening and distortion of ultrashort pulses.

2.2.3 Nonlinear effects

As light beam propagates inside the core of the optical fiber, the intense peak power modifies the refractive index of the fiber material and leads to nonlinear effects. This material response can be represented by an expansion of the induced polarization, which depends on the intensity of the electric field and the dielectric susceptibility χ:

$$P=\chi^{(1)}E+\chi^{(2)}EE+\chi^{(3)}EEE \qquad \text{Eq. 19}$$

where $\chi^{(n)}$ is the nth order of susceptibility at optical frequencies. When the applied electric field is significantly weaker than the internal electric field of the dielectric material, the induced electric polarization consists predominantly of the linear susceptibility $\chi^{(1)}$ and as such, results in a linear response within the material. The effects of $\chi^{(1)}$ give rise to the refractive index $n\left(Re\left[\chi^{(1)}\right]\right)$ and the attenuation coefficient $\alpha\left(Im\left[\chi^{(1)}\right]\right)$. When the intensity of the applied electric field is comparable to the internal one, the higher order nonlinear terms become significant and need to be taken

into consideration. The higher order susceptibilities ($n \geq 2$) are tensors of n+1 rank and are responsible for a variety of nonlinear effects, namely, second harmonic generation and sum frequency generation. It is noted that in isotropic materials $\chi^{(2)}$ is zero under the dipole approximation, therefore in materials like silica fiber, graphene, carbon nanotubes, it is neglected. Consequently, the dominant nonlinear effects in such materials are related to $\chi^{(3)}$. Typically, $\chi^{(3)}$ is responsible for phenomena including third harmonic generation THG, nonlinear refraction and four-wave mixing FWM. Its contributions originated from the electric response of the atoms, the vibrational response of the molecules, thermal effects and electrostriction effects [66]. For optical fibers, the nonlinear processes involving THG and FWM are not efficient unless steps are taken to ensure phase matching. Therefore, most nonlinear effects in fibers originate from nonlinear refraction, referring to the intensity dependence of the refractive index. The total index n is intensity dependent and can be expressed using nonlinear refractive index n_2 and intensity I , given by:

$$n(\omega, I) = n_0(\omega) + n_2 I \qquad \text{Eq. 20}$$

$$n_2 = \frac{3}{8n}\mathrm{Re}\left[\chi^{(3)}\right] \qquad \text{Eq. 21}$$

where $n_0(\omega)$ is the linear refractive index of the material. The nonlinear refractive index gives rise to self-phase modulation SPM and cross-phase modulation XPM. The imaginary part $\mathrm{Im}\left[\chi^{(3)}\right]$ gives rise to two-photon absorption.

Self-phase modulation SPM

Self-phase modulation leads to the spectral broadening of optical pulses during propagation. For fibers, this process is related to two length scales, nonlinear length L_{NL} providing the length scale over which nonlinear effects become significant, and

effective length L_{eff} which is shorter than the fiber length as it takes fiber loss into account. These quantities are defined as:

$$L_{NL} = \frac{1}{\gamma P_0} \quad \text{Eq. 22}$$

$$L_{eff} = \frac{1-\exp(-\alpha L)}{\alpha} \quad \text{Eq. 23}$$

where P_0 is the incident peak power and α is the fiber absorption coefficient. γ is the nonlinear parameter defined as:

$$\gamma = \frac{n_2 \omega_0}{c\, A_{eff}} \quad \text{Eq. 24}$$

where n_2 is the nonlinear refractive index, ω_0 is the frequency, c is the speed of light in vacuum and A_{eff} is the effective mode area of the fiber.

For a time-scale normalized to the input width T_0 expressed by:

$$\tau = \frac{T}{T_0} \quad \text{Eq. 25}$$

we have a normalized U such as $A(z,\tau) = \sqrt{P_0}\exp\left(\frac{-\alpha z}{2}\, U(z,\tau)\right)$. If we ignore the dispersive effects in the master equation Eq.12, we can describe $A(z,t) = A(0,t)\exp(i\phi_{NL})$ where ϕ_{NL} is expressed by:

$$\phi_{NL}(L,T) = |U(0,T)|^2 \frac{L_{eff}}{L_{NL}} \quad \text{Eq. 26}$$

where $U(0,T)$ refers to the field amplitude before being launched into the fiber and T is the normalized time expressed by $T = t - \frac{z}{\upsilon_g}$ where z is the distance along the propagation direction in time. Consequently, the maximum phase shift ϕ_{max} occurs when T is equal to zero. If U is normalized and centered to zero such that $|U(0,0)| = 1$ then:

$$\phi_{max} = \frac{L_{eff}}{L_{NL}} = \gamma P_0 L_{eff} \qquad \text{Eq. 27}$$

which can be reduced to $\phi_{max} = \gamma P_0 L$ if $\alpha L \ll 1$. This results in a temporally varying phase, which in turn causes the variation of optical frequency with time. The time-dependent phase change caused by SPM is associated with a modification of the optical spectrum. This modification is related to the initial pulse shape and chirp [67]. If the pulse is initially up chirped, SPM leads to spectral broadening whereas spectral compression will occur if the initial pulse is down chirped. In a special case of optical pulses propagating in anomalous dispersion, the chirp from SPM can be balanced by dispersion and this leads to the formation of solitons.

Stimulated Raman scattering

Stimulated Raman scattering SRS is an inelastic scattering process of photons from vibrations and density variations of silica. This process occurs when a photon of frequency ω_p is downshifted or upshifted to a frequency ω_s following by the creation of a phonon at the appropriate energy and momentum to conserve the energy when propagating through a medium. Such frequency shifted radiation is known as Stokes and anti-Stokes wave respectively [63]. SRS is an important nonlinear process in optical fibers due to the waveguide nature of optical fibers that ensures a high-power density maintained over hundreds of meters. Also, given that silica is amorphous, there are many available vibrational states, which lead to a very broad Raman gain.

Stimulated Brillouin scattering

Stimulated Brillouin scattering SBS is comparable to SRS. It can be explained by considering the formation of an acoustic wave in the fiber, generated by the electric field of the pump and forming a pressure wave in the material through electrostriction [68]. The acoustic wave modulates the refractive index of the fiber, setting up the conditions for Bragg reflection, which scatters and reflects the light. This corresponds to a

downshifted frequency due to the Doppler shift associated with the travelling acoustic wave. In the case of SBS, the Stokes waves propagates in the backward direction.

Cross-phase modulation

Cross-phase modulation XPM describes the interaction between two co-propagating optical fields through a nonlinear medium without involving any energy transfer. This process relies on the intensity of not only one beam but also on the intensity of any co-propagating beams. It is always accompanied by SPM.

A parameter known as the walk-off length is commonly used in the discussion of XPM process:

$$L_{walk-off} = \frac{\tau}{d} \qquad \text{Eq. 28}$$

where τ is the initial pulse width and d is given by:

$$d = \frac{\upsilon_a - \upsilon_b}{\upsilon_a \upsilon_b} \qquad \text{Eq. 29}$$

The terms υ_a and υ_b correspond to the group velocity at λ_a and λ_b respectively. XPM promotes a variety of spectral and temporal effects depending on the group velocity mismatch between the two pulses and the dispersion length given by:

$$L_D = \frac{\tau^2}{|\beta_2|} \qquad \text{Eq. 30}$$

where β_2 is the group velocity parameter. Considering an optical fiber of length L, the co-propagating process, involving nonlinearity and dispersion, can be discussed in different conditions:

- If $L \ll L_{walk-off}$, $L \ll L_D$ then XPM is insignificant.
- If $L_{walk-off} < L$, $L \ll L_D$ then the spectrum is broadened asymmetrically while the pulse shape is maintained.
- If $L_{walk-off} \ll L$, $L_D \ll L$ then both the spectrum and pulse shape are altered.

Modulation instability

Modulation instability MI is a feature of optical signal propagation in a non-linear anomalous dispersive medium. The process can be understood with the formalism of FWM [69]. It originates from a non-stable solution to the NLSE under perturbation in the anomalous dispersion region and manifests itself as amplification of noise fluctuations of a continuous wave CW or quasi-CW field, with frequencies in the parametric gain sidebands and thus these fluctuations experience gain [70]. Solitons form because of being trapped in this process, therefore ultrashort pulses with peak power orders of magnitude higher than the initial pump source are generated.

2.3 The fundamentals of mode-locking

The development of rare-earth fibers led to the tremendous growth and advent of fiber amplifiers, which have revolutionized the design of optical fiber communication systems. In addition, these amplifiers can be converted into fiber lasers by placing them inside a fiber cavity designed to provide optical feedback. Such lasers can be made to produce optical pulses of extreme ultrashort duration and are called mode-locked fiber lasers.

Mode-locked lasers are an extremely useful type of laser. The usefulness of such systems, while perhaps not obvious at first, is immense. Application of these lasers range from industrial micro-machining all the way to facilitating the most precise frequency measurements ever made. Based on the many proposals for innovative technologies that utilize mode-locked lasers, they will be an invaluable tool for future technologies.

2.3.1 Introduction to mode-locked fiber lasers

Passively mode-locked fiber laser sources have been extensively developed in recent years across a broad range of applications requiring ultrashort pulses, such as micromachining, telecommunications, and medicine, because of their compactness, simplicity, and low-cost. The history of the fiber laser can be traced back to 1961 when

Snitzer used a 300 µm-core-diameter Nd-doped fiber in a laser cavity to initiate laser action [14]. A few years later, with the aim of power-scaling, the fiber amplifier was proposed and reported by Koester et al., where 47 dB gain was achieved through a 1-m long angle cleaved Nd-doped glass fiber [15]. The major problems, which limited the development of fiber based sources in that period were high fiber loss and the limited availability of pump diodes. Several years later, researchers at Corning reported the low-loss single-mode fiber waveguide, which was very close to the intrinsic material scattering loss limit [71]. The improvement of fiber loss benefited the fabrication of gain fiber. In 1973, Stone et al. utilized a low-loss silica fiber doped with a compound of Nd_2O_3 and Al_2O_3 and the core was end-pumped by a diode [72]. This experiment supported the potential development of low-loss, high-efficiency fiber lasers. Substantial improvements were made to overcome the loss issue due to the growing interest of using fibers for telecommunications. Researchers at Bell labs successfully reduced the fiber loss to as low as 0.2 $dB.km^{-1}$ in 1974 [61]. Later, Er-doped fiber amplifiers were developed with the advantage that their operation wavelength at 1.55 µm minimizes the losses, which is necessary for communications [73].

Mode-locking is an effective technique to produce ultrashort pulses and has been extensively used in lasers systems, with the first demonstration [11] just four years after the development of the laser. Figure 2:3 shows the formation of a pulse train, which is due to the constructive interference between oscillating modes.

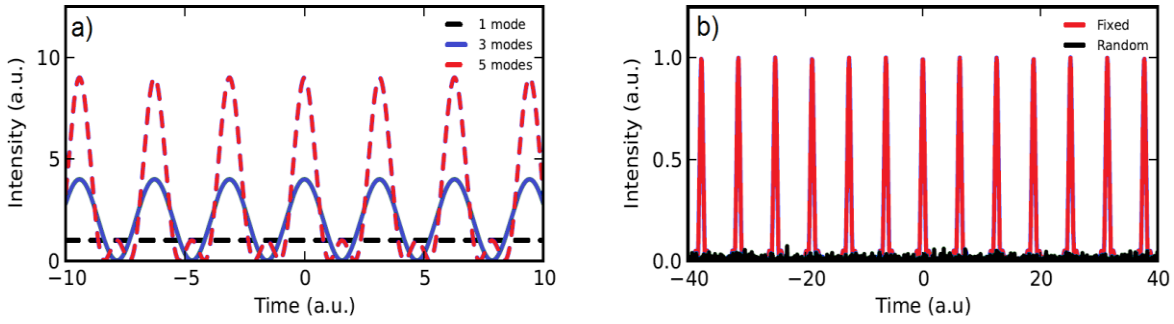

Figure 2:3. The formation of a pulse train resulting from constructive interference between oscillating waves: a) Arbitrary temporal intensities for 1, 3 and 5 modes, b) fixed phase relationship for a pulse train and random phase for a CW signal.

The simultaneous oscillation of a series of highly coherent, phase-locked longitudinal modes of a resonator which periodically emits ultrashort pulses with the entire energy of the light field. Pulse durations of less than 10 fs can be generated directly from a Ti: Sapphire laser. A 2.6 fs pulse was reported by Yamashita et al. [74], through the compression of an ultrabroadband white-light continuum using both induced-phase modulation and self-phase modulation in an Ar-gas-filled hollow fiber.

2.3.2 Pulsed regimes

While the shortest pulses have been generated by a continuous-wave CW mode-locked laser, there are other pulsating regimes: gain switched, Q-switched, and mode-locked pulses. We will start by briefly discussing the definition of the different regimes.

Gain switching

Gain switching is a direct method to generate pulses by modulating the laser gain via the pump power. In this approach, a high pump power is applied to a laser. If the gain coefficient exceeds the loss coefficient, optical pulses are produced. The pulse duration obtained can be shorter than the pump pulse and the higher the pump pulse energy, the shorter the pulse build-up time or the required pump pulse duration. This technique has been widely exploited in pulsed semiconductor lasers as it is easy to modulate the electric current used for pumping.

Q-switching

Q-switching is a technique used extensively with optically pumped solid-state lasers. In this scheme, the emission of pulses is achieved by decreasing the resonator loss periodically with the use of an intra-cavity modulator. Therefore, the Q-switching scheme can be explained as a loss switching. This technique is based on storing energy in the atoms in the form of an accumulated population inversion during the off-times. Subsequently, during the on-times, the stored energy is released, and intense pulses

are generated. A Q-switched laser normally produces high average output power at tens or hundreds of kilohertz repetition rate and the pulse duration is usually in the microsecond scale.

Mode-locking

Ultrashort pulses are in most cases produced by mode-locked lasers. A mode-locked cavity contains either an active device or a non- linear passive element, producing a loss or phase modulation to help the formation of the pulse circulating within the cavity. Differing from the previous two regimes, this method is obtained by coupling the longitudinal modes of a laser and locking their phases to each other. In the time domain, the output of a mode-locked laser is a train consisting of short pulses with a fixed separation $\Delta T = \frac{c}{L}$ for a ring configuration, and $\Delta T = \frac{c}{2L}$ for a linear configuration where L is the optical length of the resonator. The repetition rate of mode-locked pulses is the reciprocal of the round-trip time. The pulse duration is much shorter than the cavity round-trip time and depends on the factors including the gain bandwidth, modulation depth of the modulator, and the bandwidth limited element, such as a bandpass filter.

The incorporation of a saturable absorber into a laser can achieve mode-locking. Typically, in a solid-state cavity, this introduces a Q-switching tendency that can drive the laser into the regime of Q-switched mode-locking as shown in Figure 2:4(a).

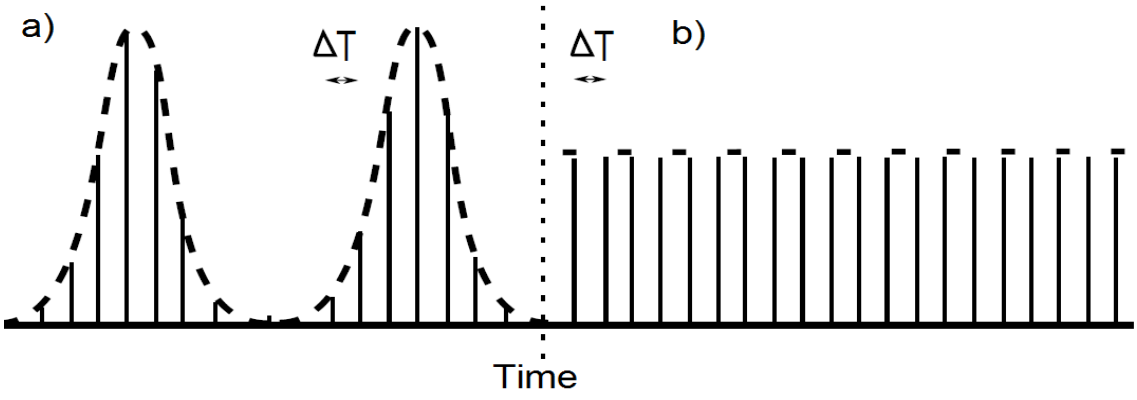

Figure 2:4. Mode-locked pulse trace in the time domain, (a) Q-switched mode-locking and (b) CW mode-locking.

The output pulses are generated underneath a Q-switched envelope, leading to a large oscillation of pulse energy. These instabilities are unwanted for many applications, implying the strong fluctuation of parameters and showing that pulse parameters do not reach a steady state. These drawbacks can be overcome through several methods: using a small mode area fiber; incorporate an electronic feedback to build up the stability of the resonator; reducing the loss or increase the intra-cavity power; optimizing the modulator e.g. saturable absorbers.

The theory of stability limits for ultrashort pulses in a solid-state laser was developed by Kärtner [75] and subsequently extended by Hönninger [76], deriving a criterion for the minimum intra-cavity pulse energy, which is required for obtaining stable CW mode-locking shown in Figure 2:4.(b), a regime preferable for many applications where a constant pulse energy and high repetition rate is required:

$$E_p^2 > E_{sat,g} E_{sat,a} \Delta R \qquad \text{Eq. 31}$$

where E_p is the intra-cavity pulse energy, $E_{sat,g}$ is the saturation energy of the gain medium, $E_{sat,a}$ is the saturation energy of the absorber and ΔR is the modulation depth. Although it is necessary to include the interplay of dispersion and nonlinearity, gain filtering, and effects caused by the saturable absorber, this expression describes a qualitative understanding of the dynamics. The threshold of CW mode-locking can be reduced by decreasing the saturation energy and modulation depth of the saturable absorber, which can be achieved by careful design. However, this optimization is a tradeoff: a small modulation depth will lead to the reduction of self-starting performance, particularly in fiber lasers, where a relatively large modulation depth is required due to the strong gain efficiency, significant nonlinearity and dispersion. The discussion of mode-locked fiber lasers with saturable absorber SA is outlined in the following section.

2.3.3 Techniques of mode-locking

The methods of mode-locking can be divided into two categories: active mode-locking, where the mode-locking element is driven by an external modulator; and passive mode-locking, where the element which induces mode-locking exploits a nonlinear optical effect.

Active mode-locking

Active mode-locking will not be discussed in this thesis beyond a brief description of the basic mechanism. This technique was first investigated by Kuizenga and Siegman [77] using a Gaussian pulse analysis. Active mode-locking can be implemented using: an amplitude modulator AM, a phase modulator PM, or synchronous pumping - a periodic modulation of the laser gain at a repetition rate equal to the round-trip frequency. AM and PM are typically used for short pulse generation (< 1ps) rather than mode-locking by synchronous pumping, which generally is applied to active media with nanosecond relaxation time. The principle of active mode-locking is presented in Figure 2:5.

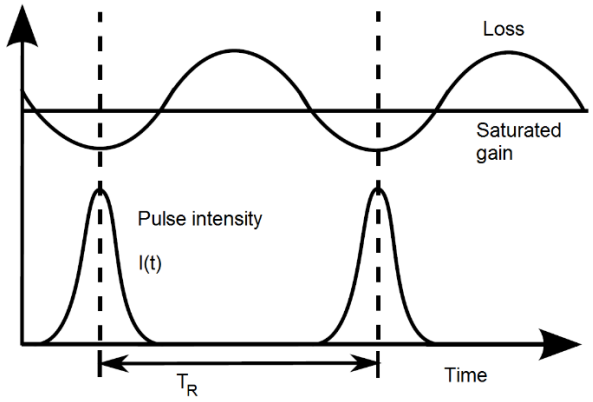

Figure 2:5. Diagram of active mode-locking process.

This technique involves the periodic modulation of the resonator loss or of the round-trip phase change. The pulse is selected through a periodic loss modulation process, as it can pass through only at the loss minima. Therefore, the intra-cavity field is modulated at the same frequency of the repetition rate of the modulator. The pulse width in the order of picoseconds. In fact, the attenuation of the wings effectively leads

to pulse shortening at each round trip, while due to other processes such as gain narrowing, it tends to broaden.

An analytical solution can be approached based on the master equation [78] . The modulation strength M_s corresponding to the curvature of the loss modulation in the time domain at the minimum loss point can be written as [22]:

$$M_s = \frac{M\omega_M^2}{2} \qquad \text{Eq. 32}$$

where M is the maximum amplitude of the loss profile and ω_M is the modulation frequency that must be tuned to the resonator round-trip time such as $\omega_M = \frac{2\pi}{T_R}$. The pulse width based on the Kuizenga-Siegman theory, is the fourth root of the ratio between gain dispersion D_g and modulator strength M_s , given by:

$$\tau^4 = \frac{2g}{\Omega_g^2 M \omega_M^2} \qquad \text{Eq. 33}$$

where g and Ω_g represent the saturated single-pass gain and gain bandwidth respectively. The achievable pulse width is inversely proportional to the fourth root of the curvature in the loss modulation and is limited by the speed of the external signal generators.

Passive mode-locking

The shortest pulses reported to date have been generated using passive mode-locking techniques based on saturable absorbers. There are several types of saturable absorbers currently used in laser technology. They can be generally classified into two categories: artificial and real SAs as shown in Figure 2:6.

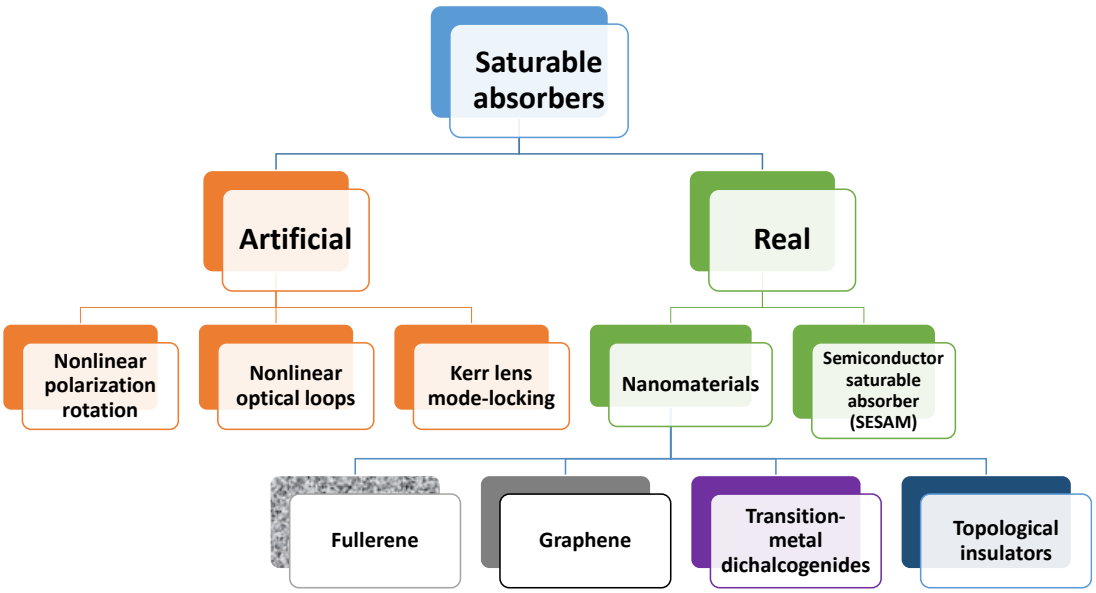

Figure 2:6. Types of saturable absorbers for ultrafast lasers.

The term "artificial SA" refers to a mode-locking technique, where a power dependent nonlinear optical effect acts as a saturable absorber. Among those techniques, the most important include nonlinear polarization rotation NPR, nonlinear loop mirrors NOLM or nonlinear amplifying loop mirror NALM, and Kerr-lens mode locking KLM. Among real saturable absorbers we can distinguish two groups: semiconductor saturable absorber mirrors SESAMs and nanomaterials. The SESAMs are currently one of the most widely used saturable absorbers in solid-state and fiber lasers, also in commercially available industrial systems. They are based on a well-established technology developed for more than 20 years [79]. However, SESAMs have some limitations. The technology is based on semiconductors (e.g., InGaAs/GaAs quantum wells), which are characterized by an energy band gap. Consequently, this results in a limited wavelength operation range. Thus, each SESAM needs to be designed strictly for a specific laser operating at a certain wavelength. Fabrication of the SESAM also involves expensive and complicated molecular beam epitaxy MBE technology [80] . All those limitations have driven the laser community to seek for alternative, new saturable absorber materials. The field of nanomaterial-based SAs emerged in recent years to one of the most important branches of ultrafast laser technology. This new era started in 2003 as Set et al. [81] demonstrated the first carbon nanotube CNT mode-locked fiber laser.

Few years later, in 2009, the first lasers utilizing graphene were reported [82], [83]. Starting from this date, the number of papers and reports on fiber lasers mode-locked with graphene and other 2D materials: topological insulators, transition metal dichalcogenides, and recently black phosphorus, grew rapidly.

Saturable absorption is a nonparametric nonlinear optical process, which occurs in many materials under excitation with high-power light beam. In general, the optical transmittance of a saturable absorber is power dependent in a way that it introduces larger losses for low-intensity light. After illumination with high-intensity light, the absorption saturates, and the SA becomes more transparent. The mechanism can be described as a self-amplitude modulation introduced by saturable absorber device to the laser radiation. Low-intensity wings experience more loss than the high intensity peaks. Mode-locking starts from noise fluctuations. After circulating in the laser cavity, preferentially amplified noise spikes become strong enough to saturate the gain level and reduce the loss in the saturable absorber, reaching a steady state and as such a stable pulse train is formed. This saturation process in absorbers can also be explained from an energy perspective, based on carrier dynamics. When absorbing sufficient light, carriers from the valence band are excited to the conduction band. In the strong excitation, the absorption is saturated as the initial states of the pump are depleted and the final states are partially occupied. Figure 2:7 shows the two time-scales in this regime: a short time-scale, intra-band thermalization (on the order of hundreds of femtoseconds to a few picoseconds) and a long-time scale, inter-band recombination (on the order of a few picoseconds to nanoseconds).

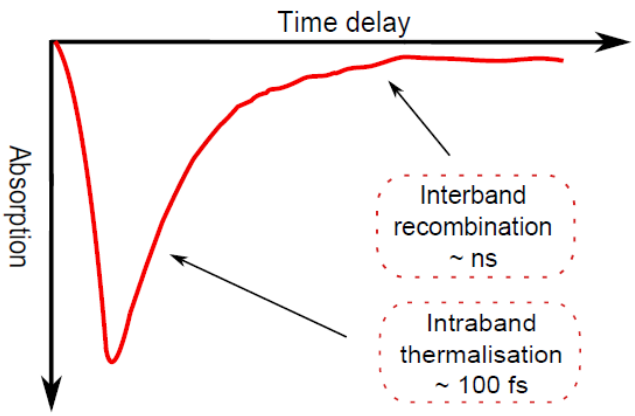

Figure 2:7. Parameters in the absorption process to achieve mode-locking.

The contributions of the short time-scale include: a coherent regime with a duration of 10-50 fs, depending on conditions and materials, a 60-100 fs time-scale of carrier-carrier scattering setting in and leading to the destruction of coherence and thermalization of the electron and hole gas, and a 300 fs-1 ps interaction between carrier gas and the lattice, all of which results in the partial recovery of the absorption. The time-scale, also known as the lifetime, is dependent on the nature of material.

2.4 Chapter summary

In this chapter, the basic principles of optical fiber have been reviewed. It was followed by a brief discussion of linear and nonlinear effects experienced by light while propagating in optical fiber including fiber losses, dispersion and nonlinearities. Furthermore, the mechanism of mode-locking has been examined, including a presentation of different pulsating regimes, mode-locking methods and operational regimes.

The management of the interplay of cavity dispersion, nonlinearity and bandwidth-filtering effect has permitted the development of lasers with distinct types of ultrashort pulse shape. To better understand the dynamics of high power mode-locked lasers, different regimes will be discussed in the following chapters.

Chapter 3 External injection effects in mode-locked lasers: a study of stability

In the last decades, optical injection was first investigated in gas and solid state lasers [84]–[87]. The early studies were devoted to injection locking [88]–[90] for its various applications such as frequency stabilization [90], [91], linewidth narrowing and chirp reduction [92], [93], polarization control [94], coherence enhancement of broad area lasers [95] and laser arrays [96]. Later, the interest was directed towards fiber lasers [47]–[49].

In this chapter, we investigate experimentally the influence of an injected continuous external optical laser on the stability of a passive harmonic mode-locked fiber laser operating in the anomalous dispersion regime. Under specific conditions, the continuous-wave significantly increases the stability of the harmonic mode-locked regime. This occurs for a discrete set of wavelengths and below a critical injected power.

3.1 Brief introduction to external injection

Passive mode locking in fiber lasers has been studied for its various interests at both fundamental and applied levels in the generation of ultrashort pulses. This process can be obtained by either the addition in the cavity of a real saturable absorber such as graphene, topological insulator [34], [36] or by means of artificial techniques like nonlinear amplified loop mirror, nonlinear polarization evolution mechanism [32]. Under certain conditions, due to the energy quantization [97], the configurations using these saturable absorbers tend to exhibit multiple pulse formation in the anomalous dispersion regime [98]. The resulting temporal pulse distribution is the consequence of soliton interaction dynamics inside the cavity that can exhibit various solitons patterns such as bound states, soliton bunches in the case of soliton attraction or harmonic mode locking when a long range repulsive interaction occurs [32].

Passive harmonic mode-locking (HML) can have a wide range of repetition rate starting from a few MHz to some GHz depending on the technique used. It has

been reported a Yb-doped fiber laser with a 2 GHz repetition rate and a supermode suppression level (SSL) of about 45 dB [99]. While using an erbium doped double clad fiber laser, passive harmonic mode locking operating at the 322nd harmonic with a repetition rate up to 3 GHz and a supermode suppression better than 25 dB has been demonstrated [43]. Sobon et al. [100] reported a 10 GHz repetition rate passive harmonic mode locked fiber laser using co-doped Er:Yb fibers, with a supermode suppression level of 16 dB. It has also been shown that in harmonic mode locking, harmonics can be tuned with a span ranging from the 6th to 928th and a repetition rate from 153 MHz to 22.2 GHz [101] with an interesting SSL of 41 dB. Different factors that might lead to this specific soliton distribution in the cavity remain uncertain. It was theoretically demonstrated that a continuous-wave component in the optical spectrum acts as an efficient agent to manage the interaction between neighboring pulses [41]. More recently it has been shown both theoretically [47], [49], [102] and experimentally [103] that a small external continuous-wave component can control the nature of the interaction between the soliton in the cavity. Even though the problem of optical injection in CW regime is quite old [104], many properties concerning its dynamical behaviors are still far from being well understood. Optical injection has been widely studied in the framework of semiconductor lasers, mainly for the important mechanism of injection locking in which ideally the spectral purity of a low power master laser is transferred to a high-power slave laser [105]. Although most of the studies were dedicated to continuous-wave injection, the case of a passively mode-locked laser has been also investigated with the objective of locking the injected laser on the external one [106]. There are very few papers concerning the injection of a continuous-wave laser on a passively mode-locked laser. In [107], [108] it was reported that a quantum dot passively mode-locked laser submitted to a continuous-wave injection could be efficiently stabilized. It has been reported independently that a low power external continuous-wave does not have a major impact on the stability of the harmonic mode locking distribution, thus highlighting the robustness of an initial state HML against the external injection [101]. To give additional physical insight to this problem, we have decided to conduct several series of experiments of a passively mode-locked fiber laser operating

in HML regime and subjected to external injection of a continuous-wave laser with variable wavelength and power.

3.2 Fiber ring cavity schematic with an auxiliary laser setup

The experimental setup is shown in Figure 3:1. It is based on an all-fiber unidirectional ring cavity exploiting the nonlinear polarization evolution technique to achieve mode-locking.

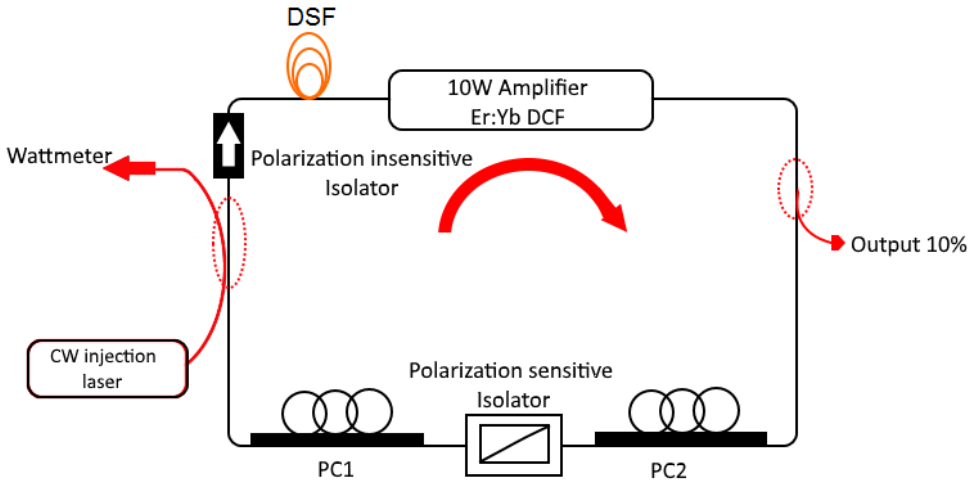

Figure 3:1 Experimental setup of the fiber ring laser using the nonlinear polarization rotation

We use a C-band double clad V-groove Er:Yb 10W fiber amplifier from Keopsys. It consists of 5 m long double-clad fiber DCF that has second order dispersion of $\beta_2^{DCF} = -0.021\ ps^2.m^{-1}$. The geometry of the inner clad has an octagonal shape. The diameter of the inner clad is 130 μm which allows a high coupling efficiency of the multimode pump waves into the fiber and the fiber core diameter is 12 μm. It is pumped at 980 nm with several laser diodes injected with the v-groove technique. The maximum achievable output power in continuous lasing operation is 10 W, ensured by the 40 W pumping power. A piece of dispersion-shifted fiber $\beta_2^{DSF} = 0.14\ ps^2.m^{-1}$ is added to control the total cavity dispersion. To ensure soliton regime together with multiple-pulse mode locking, the cavity is designed so that the total dispersion is in the anomalous regime with $\beta_2^{Total} = -0.288\ ps^2.m^{-1}$ .The total cavity length is approximately 38 m, including 30 m of standard single mode fiber SMF with a

$\beta_2^{SMF} = -0.022\ ps^2.m^{-1}$, corresponding to a round-trip time of 190 ns and a free spectral range of 5.26 MHz Polarization controllers PC are used with a polarization sensitive isolator to control the nonlinear losses of the cavity thus the operating regime of the laser. A polarization-insensitive isolator PI-ISO is employed to force unidirectional operation of the cavity. A 10 % output coupler is used to extract the power from the cavity. The 10 W amplifier requires a threshold signal on the input to turn it on which is a security requirement for protecting the internal electronic circuitry. The external optical signal used for this purpose is delivered by a homemade continuous-wave tunable fiber laser with a linewidth of 1 nm and 1.2 W maximum output power [109]. It is directly injected in the cavity through a 3-dB fiber coupler. When the principal laser is launched, we turn off the auxiliary CW laser to avoid any coupling between both lasers.

The output intensity is measured using a high-speed photodetector (TIA-1200) and visualized with a fast oscilloscope (Tektronix TDS 6124C, 12 GHz, 40 GS. s^{-1}). The spectral properties are analyzed with an optical spectrum analyzer (Anritsu MS 9710C) and the pulse duration is measured with an optical autocorrelator with a scanning range of ±100 ps (Femtochrome FR-103 XL). An electronic spectrum analyzer (Rohde & Schwarz FSP Spectrum Analyzer 9 kHz to 13.6 GHz) is used to characterize the radio frequency spectrum of the laser.

To turn on the main 10 W amplifier, it is required to have 17 dBm on the input, therefore we switch on the external laser and set it using these requirements. The main concept of this experiment is to analyze the influence of the externally injected signal delivered by the auxiliary CW laser on the behavior of the mode-locked cavity. Thus, we fix the pumping power of the auxiliary laser to provide 200 mW of output power, and we turn it off when the 17 dBm are achieved.

As the pump power is increased and while the polarization controllers within the cavity are finely adjusted, temporal splitting of optical pulses is observed due to

the soliton energy quantization effect [50]. Then a stable harmonic mode-locked distribution of solitons is achieved. Figure 3:2 shows the measured oscilloscope trace of the output pulses.

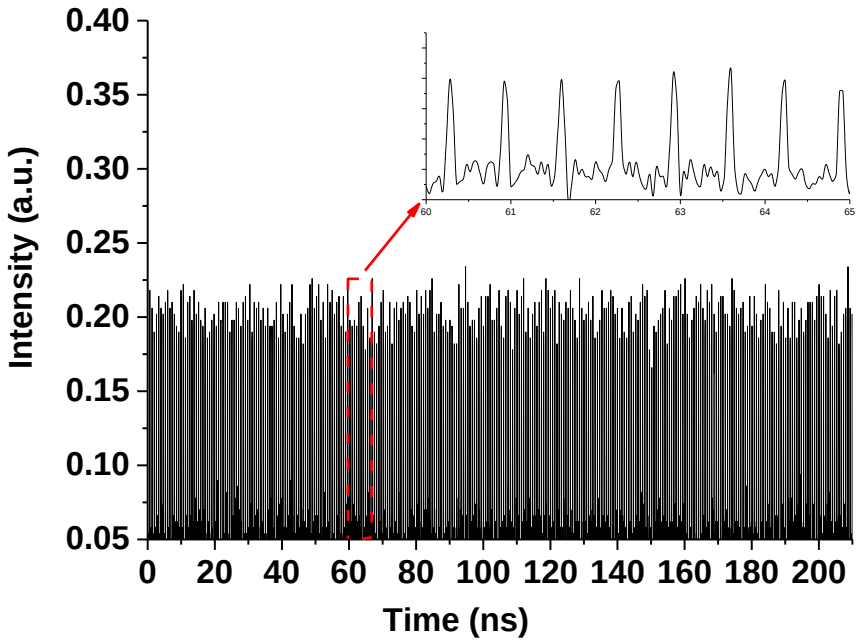

Figure 3:2. Temporal trace of the harmonic mode lock distribution. The inset shows the equally-spaced solitons.

The measured optical spectrum is depicted in Figure 3:3. It exhibits a spontaneous continuous-wave component at about 1562 nm with a magnitude of -9.6 dBm which has been identified as a main characteristic in harmonic mode lock regime [41]. The central wavelength is measured to be 1565 nm with a Full Width at Half maximum FWHM (-3dB) of 4.47 nm.

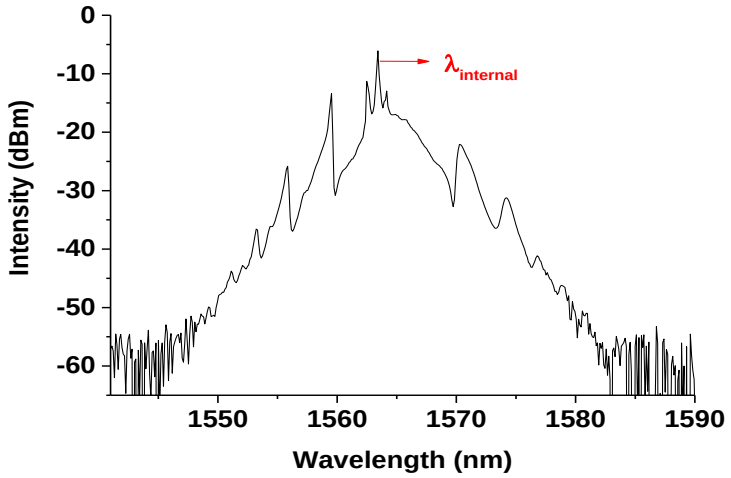

Figure 3:3. Optical spectrum trace of the free running harmonic mode lock laser

The spectrum contains several Kelly's sidebands which is a characteristic of the mode-locked distributions in the anomalous dispersion regime [110]. Figure 3:4 exhibits the measured autocorrelation trace of the optical pulses where their temporal width is estimated to be ~1.4 ps after deconvolution using a hyperbolic secant fitting curve. Considering the 3-dB bandwidth of 4.47 nm, the estimated time-bandwidth product is ~0.77 which is larger than that of transform-limited $sech^2$ pulses. This indicates that the output pulses are chirped.

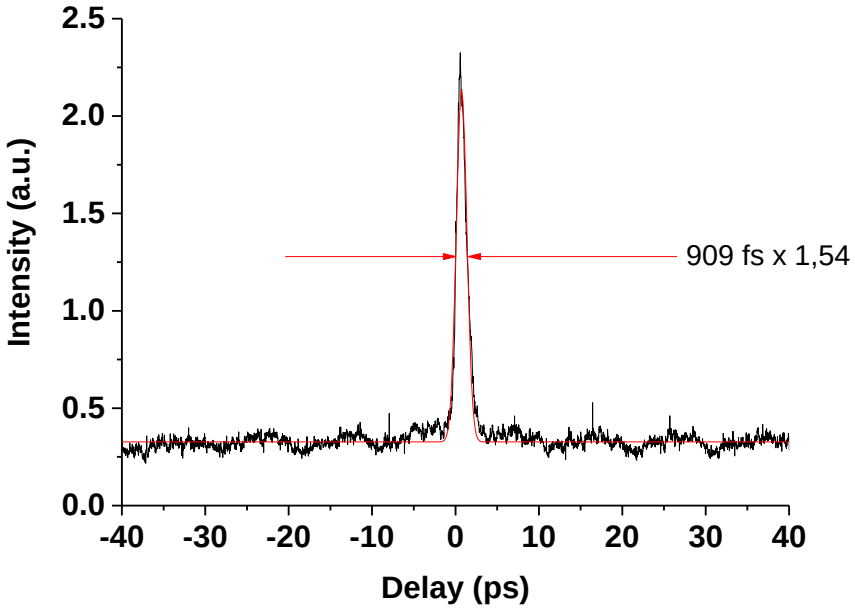

Figure 3:4. Autocorrelation trace of the generated harmonic mode lock distribution.

The measured RF spectrum of the output pulses is shown in Figure 3:5. A strong signal peak at 1.76 GHz is clearly observed and the signal to noise ratio SNR is measured to be around 20 dB over an 8 GHz frequency span. Compared to the fundamental cavity frequency, this results in the generation of the 334th harmonic.

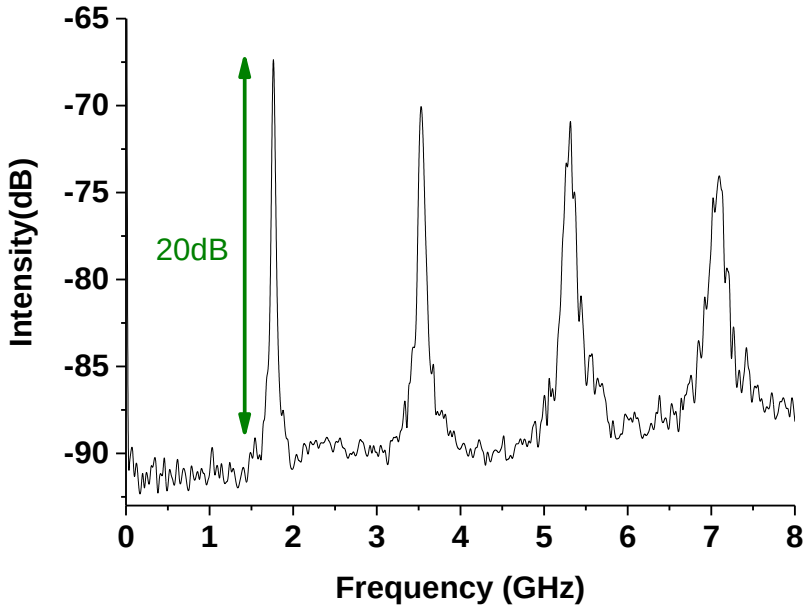

Figure 3:5. RF spectrum of the harmonic mode lock distribution with a resolution of 100 kHz.

3.3 Influence of an external laser injection on mode-locked stability

To investigate the influence of the external optical signal on the mode-locked harmonic distribution, we turn on the auxiliary laser and with the spectral filter we can shift the wavelength from 1530 nm to 1580nm. Under the influence of the external CW, the interaction between the solitons inside the cavity is affected, which can force the laser to operate in different regimes as it has been experimentally demonstrated before [103]. In our quest to find new optical distributions by starting from a well-defined initial regime, we observed that under precise circumstances, the injected laser influenced the stability of the harmonic mode lock distribution. In fact, the more the external signal shifted towards long wavelengths the higher the supermode suppression ratio became. To present the results, we will show the temporal trace, optical spectrum, RF spectrum and autocorrelation trace under each case of injection, keeping in mind that, except when clearly mentioned, neither the injected input power nor the mechanism of harmonic mode locking are modified.

3.3.1 External injection with λ = 1545 nm

Based on the obtained harmonic distribution, we inject the external CW signal into the optical spectrum of the main cavity starting from the short wavelengths. We set the external CW signal at λ = 1530 nm with an average output power of 75 mW, then we tune slowly towards the longer wavelengths. Between λ = 1530 nm and λ = 1545 nm, there is no significant effect on the output distribution. When the external signal reaches 1545 nm, we do not notice a modification of the oscillator distribution's nature as naturally expected [47], [111], [112], instead the external CW improves the SNR of the output pulses. The optical spectrum depicted in Figure 3:6 validates the presence of the injected signal around 1545 nm. The internal continuous-wave component and the sidebands are still present in the spectrum, the center is at 1565 nm and the spectral width at FWHM is Δλ = 3.71 nm, which is narrower than without the injection. We can note that the amplitude of the external continuous-wave (-12.8 dBm) remains below the one of the internal continuous-wave component (-9.6 dBm).

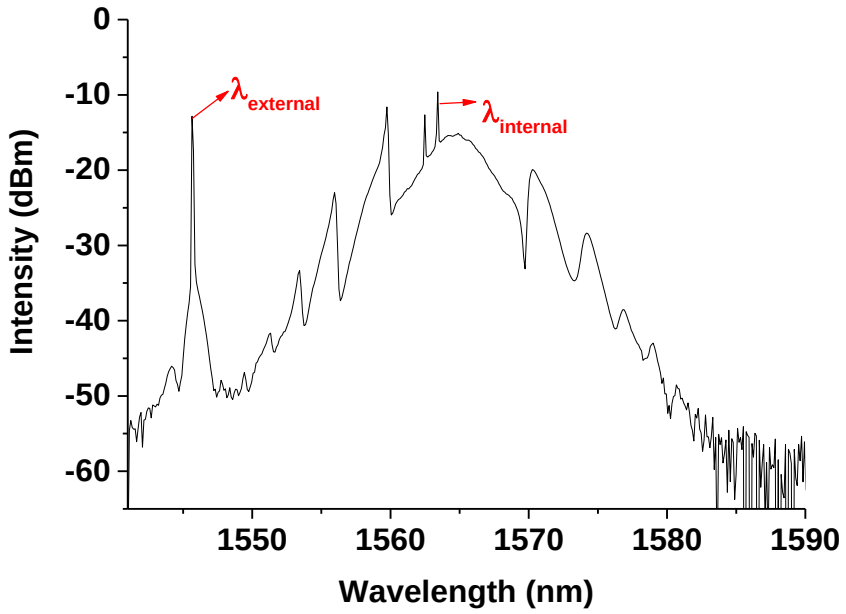

Figure 3:6. Optical spectrum of the HML laser with an injected λ =1545 nm.

As mentioned earlier, we can see the impact of the injected external continuous-wave clearly visible in the RF spectrum of Figure 3:7 which confirms the improvement of the SNR level. We have a fundamental harmonic frequency around 1.76 GHz

with a SSL of 25 dB. The pulse duration remains almost the same about ~1.4 ps. We also notice an increase in the intensity of the autocorrelation trace.

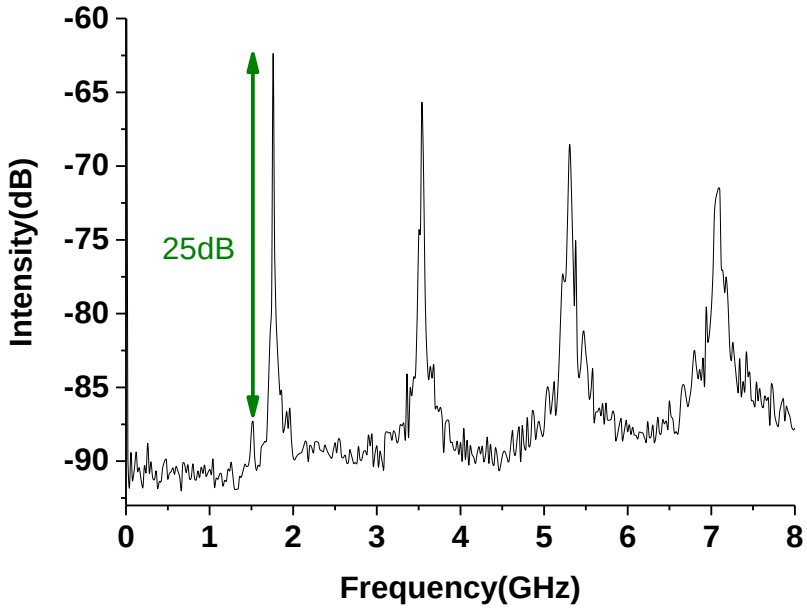

Figure 3:7. RF spectrum trace of the HML with an injected λ =1545 nm.

3.3.2 External injection with λ = 1548 nm

We continue shifting the wavelength of the external signal till we reach 1548 nm. We notice that between λ = 1545 nm and λ = 1548 nm we lose the harmonic mode locking distribution which gives place to a random distribution of solitons. This is in total agreement with previous studies [47], [111], [112] where it has been demonstrated that the external CW signal modifies significantly the nature of interaction and breaks the bonds between the solitons.

Based on the optical spectrum in Figure 3:8, the central wavelength is still at 1565 nm and spectral width at FWHM remains unmodified with Δλ = 3.71 nm.

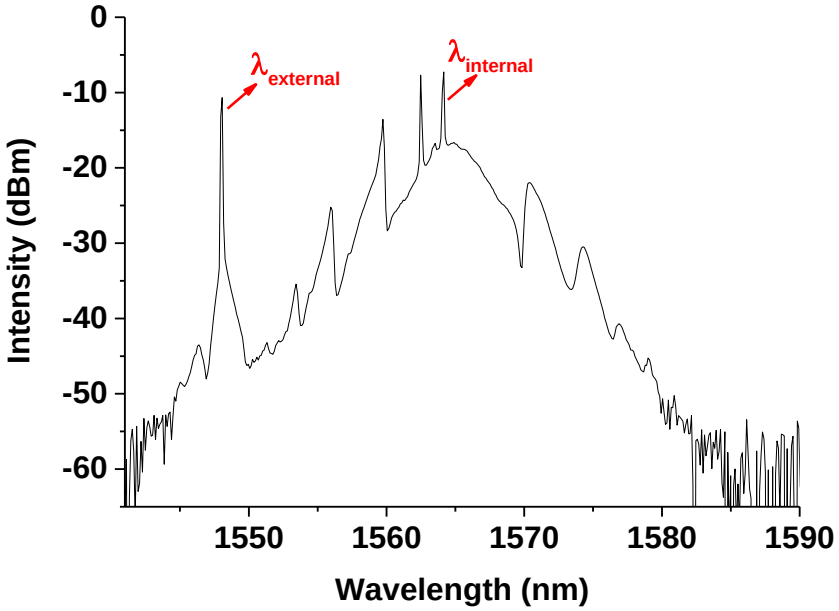

Figure 3:8. Optical spectrum trace of the HML laser with an injected λ=1548 nm.

As it has been measured before, the pulse duration is almost the same about ~1.4 ps and we still have the same number of solitons in the cavity. Moreover, the optical spectrum shows that there is no significant change on the amplitudes of the internal and injected continuous-wave components. Meanwhile, the RF spectrum in Figure 3:9 exhibits a drastic improvement of the SNR level. We have a fundamental harmonic around 1.76 GHz with SNR of 32 dB, significantly higher than that without injection.

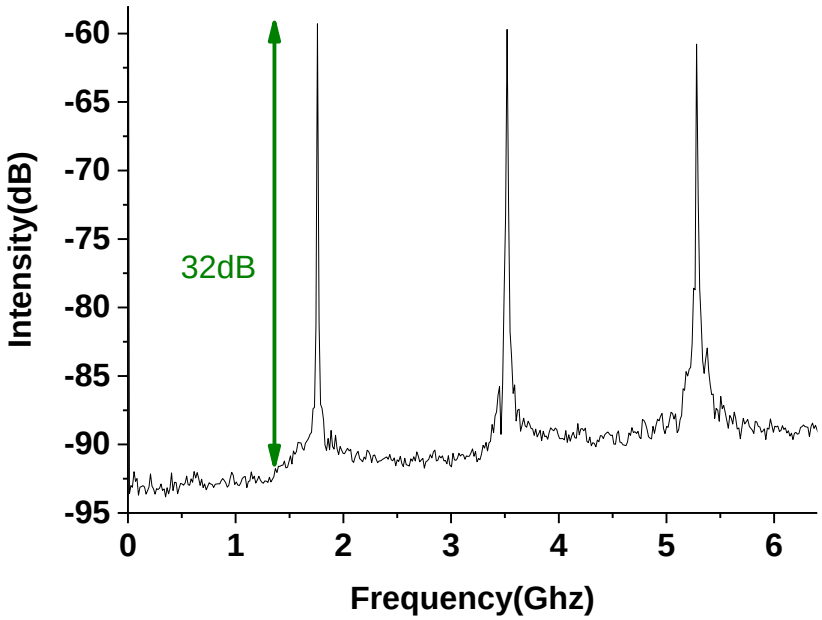

Figure 3:9. RF spectrum trace of the HML with an injected λ =1548 nm

3.3.3 External injection with λ = 1549 nm

When we move closer to the first side band, the optical spectrum shown in Figure 3:10 shrinks in width and amplitude. We note the central wavelength at 1565 nm and the spectral width at FWHM is Δλ = 3.29 nm.

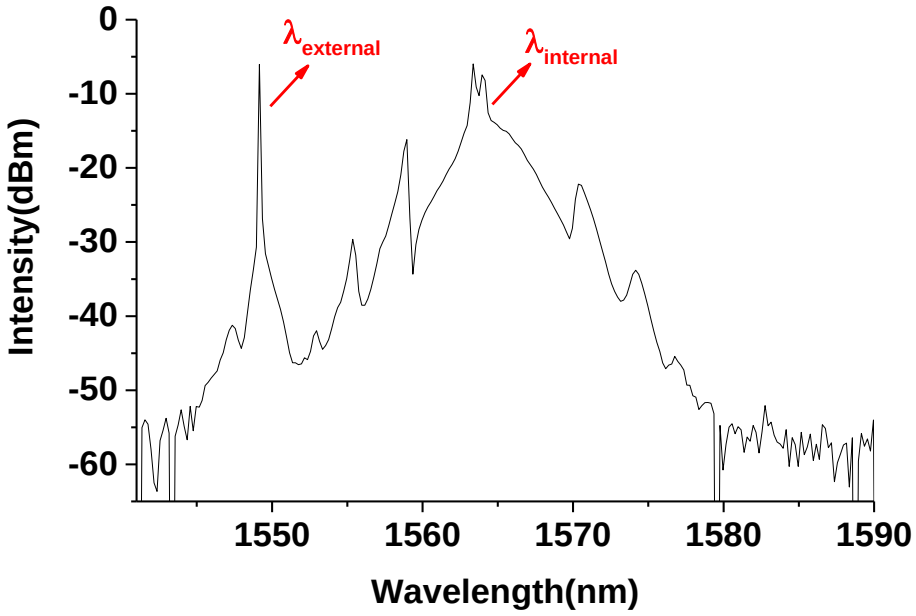

Figure 3:10. Optical spectrum trace of the HML laser with an injected λ=1549 nm.

This behavior occurs typically because the amplification of the external CW signal becomes more important when we are close to the center of the optical spectrum. Such amplification leads to a comparable magnitude of the internal continuous-wave component and the injected signal, of about -6 dBm. The pulse duration is almost stable about 1.4 ps which means we are still in the same soliton distribution as before and we notice a decrease in the intensity of the autocorrelation trace.

The RF spectrum in Figure 3:11 shows a big loss of stability compared to the previous cases. We have a fundamental harmonic around 1.76 GHz with an SNR level of 18 dB. Hypothetically, this behavior is rather expected since the amplitude of the external continuous-wave component is nearly equal or superior to the internal continuous-wave component, which leads to a strong laser perturbation and the HML regime is lost.

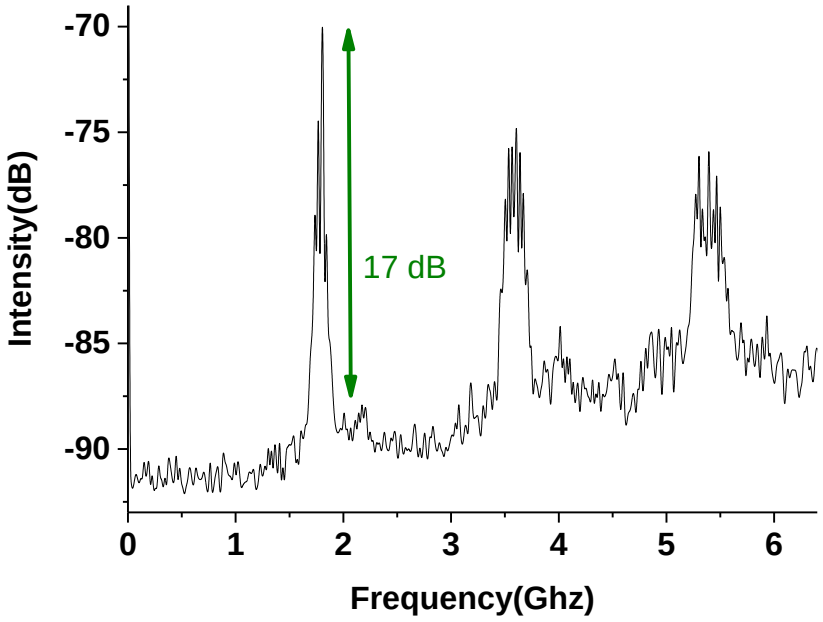

Figure 3:11. RF spectrum trace of the HML with an injected λ =1549 nm

To confirm this hypothesis, we have done several series of experiments. First, starting from a stable HML regime, we have switched on the external laser with an initial wavelength out of the spectrum of the principal laser and with a power comparable to the internal continuous-wave component. Once the wavelength approaches the spectrum of the 10 W laser, there occurs a sudden injection locking phenomenon characterized by a spectral locking of the 10 W laser on the injected signal. In this case the laser changes to the continuous-wave operating regime. Such situation corresponds to classical results on injection locking experiments in which a slave oscillator locks its frequency on a master oscillator [105]. We have noticed that if the power of the injected signal is then reduced or the wavelength tuned out of the 10 W laser spectrum, the initial HML regime is not restored. Starting from the situation of Figure 3:10, if the wavelength of the external signal is further increased, the HML regime is lost and the laser operates in another multiple pulsing regime. Then, if the external power is reduced, the HML regime is not restored unless the wavelength is tuned significantly below its initial value and then increased to its initial value. Such behavior is characteristic of an optical memory since the operating regime depends on the path. Finally, we have verified that for the initial situation of Figure 3:10, if the injected power is reduced the SNR increases up to about 23 dB. Hence our experimental results strongly suggest that the relative magnitudes of the internal and external continuous-

wave are a key parameter for improving the stability of the HML regime. Therefore, we can conveniently represent the previous results in a diagram which depicts the evolution of the SNR as a function of injected wavelength for a fixed injected power. The results are presented in Figure 3:12 and it demonstrates that the SNR is increased for a discrete set of external wavelengths and, out of these narrow ranges, the SNR is significantly reduced till the HML is lost.

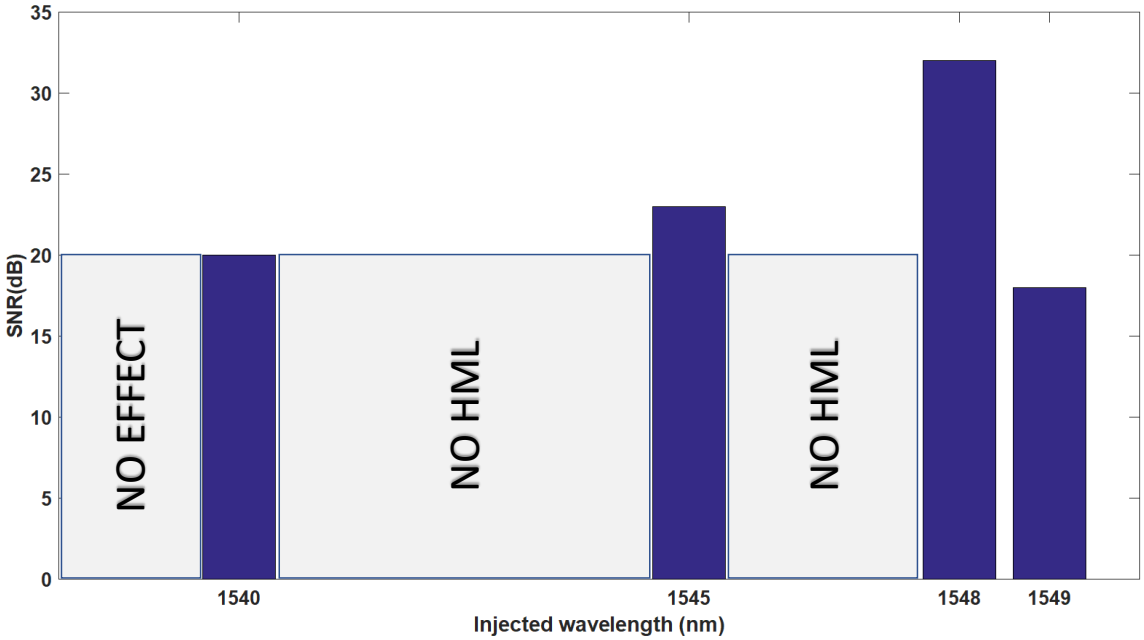

Figure 3:12. Influence of the external injection on the SNR on the HML distribution.

In addition, the SNR level increases when we shift to longer injected wavelengths until the amplitude of the external signal becomes nearly equal to the amplitude of the internal continuous-wave component. At this point, there is a sudden decrease of the SNR. Consequently, we have two conditions for which the stability is increased: the level of the injected pulse should be lower than the level of the self-generated continuous-wave and the wavelength of the injected pulse must belong to a discrete set of well-defined values.

3.4 Chapter summary

We have demonstrated in this chapter, an experimental study and analysis concerning the influence of an externally injected CW signal on an established har-

monically mode-locked distribution under the mechanism of the nonlinear polarization rotation. The presented results provide experimental proofs that the stability of such regime can be significantly improved by implementing an external injection.

From a theoretical point of view, Komarov et al. demonstrated that HML regime can be forced by external continuous optical injection [47]. They reported that the HML regime could be obtained when the external wavelength was resonant with Kelly's sidebands. Our experimental results do not address the same problem because we start directly from a HML regime. However, these results show that some resonance phenomenon occurs for the improvement of the stability of the HML regime. From this perspective, the experimental results confirm that a resonant effect occurs although we have not demonstrated that there is a resonance with Kelly's sidebands. Such point requires specific studies and additional numerical simulations.

Chapter 4 Pulse duration and energy scaling in mode-locked fiber lasers

The previous chapter was a continuation of the earlier works concerning the influence of injection of mode-locked lasers in our lab. The recent theoretical works of our colleagues motivated us to start experimental trial on high energy pulse generation. Mode-locked double-clad co-doped fiber lasers capable of producing nanosecond level pulses with high energy have many advantages for various applications. An increase in the mode-locked pulse's energy can be achieved by carefully choosing the cavity parameters.

Dissipative soliton resonance DSR mechanism leading to high energy mode-locking has been reported in different fiber laser configurations. In this chapter, we will investigate this phenomenon with double-clad amplifiers in all-fiber laser setups. Different pulse width and energies can be realized with different parameters of the laser cavity by exploiting the dissipative soliton resonance mode. Even in the DSR operation, a multi-pulsing can be observed in the form of harmonic generation of square pulses. Finally, a new type of staircase shaped pulses has been identified based on the spectral doublet that exists in the DSR region.

4.1 Introduction to dissipative soliton resonance

The pulses forming in the mode-locked fiber lasers frequently take the shape of a soliton. The shape and energy of a soliton are preserved during the propagation. The laser is characterized by continuous energy flow, which leads to a strong requirement of an additional balance between gain and loss for the soliton formation to occur. Dispersion spreads the pulse in the time domain, while nonlinearity broadens it in frequency domain. Thus, to produce stationary state in fiber laser, the balance between gain and loss, dispersion and nonlinearity is needed. This fact exposes the dissipative nature of solitons formed in a fiber laser [113]. As a consequence, the energy dissipa-

tion in the cavity leads to an interaction of solitons and formation of multi-soliton complexes such as bound solitons, bunch of solitons and soliton rains [32], [42], [44], [47], [114], [115].

Conventionally, the propagation of light in a laser cavity is well explained by Maxwell's equations for electromagnetic waves. Since lasers contain various elements in the cavity, all important physical effects must be considered. Therefore, the theoretical model must introduce different propagation equations explaining the complexity of the system and including the response of the saturable absorber and gain medium. Thus, it is beneficial to start with a master equation that incorporates all the physical elements that play a role in the mode-locking mechanism [24], [116], [117]. It turns out that the main master equation is a variation of the more general physical approach, the cubic complex Ginzburg–Landau equation [118], a universal equation used to describe systems near bifurcations. However, the inclusion of a quintic saturating term in the Ginzburg–Landau equation was shown to be essential for the stability of pulsed solutions [119]. From another point of view, the complex cubic–quintic Ginzburg–Landau equation (CGLE) is the extension of the nonlinear Schrödinger equation to higher-order and dissipative terms. The CGLE has been used to describe a wide range of nonlinear optical systems, such as passively mode-locked lasers with fast saturable absorbers, parametric oscillators, wide aperture lasers and nonlinear optical transmission lines [113]. The normalized form of the CGLE is:

$$\mathrm{i}\frac{\partial \mathrm{A}}{\partial \mathrm{z}}+\frac{\mathrm{D}}{2}\frac{\partial^2 \mathrm{A}}{\partial \mathrm{t}^2}+|\mathrm{A}|^2\,\mathrm{A}=\mathrm{i}\delta\mathrm{A}+\mathrm{i}\beta\frac{\partial^2 \mathrm{A}}{\partial \mathrm{t}^2}+\mathrm{i}\varepsilon|\mathrm{A}|^2\,\mathrm{A}-\upsilon|\mathrm{A}|^4\,\mathrm{A}+\mathrm{i}\mu|\mathrm{A}|^4\,\mathrm{A} \qquad \text{Eq. 34}$$

where the optical field envelope A , t is the retarded time in the frame moving with the pulse, and z the propagation distance, D is dispersion propagation term (it can be positive or negative depending on the regime), υ applies to a quintic Kerr effect, δ , ε , β and μ are the coefficients for linear loss (if negative), nonlinear gain (if positive), spectral filtering and saturation of the nonlinear gain (if negative), respectively. These are the basic physical effects required to build a mode-locked laser, with the expected signs of their contributions as suggested above.

The CGLE is non-integrable equation in multi-dimensions, which means that general analytical solutions are not available. Selected analytical solutions can only be found for specific relations between the equation parameters. The large and multiple regions of parameter domains of the CGLE in which stable dissipative solitons can be found is very important as it allows to explore innovative cavity designs. In fact, by managing the dispersion parameters, researchers were more interested in the net normal dispersion regime. This was stimulated by the dispersion-managed fiber laser configurations tested by Haus and co-workers in the mid-1990s [120]. The mode-locked fiber laser configurations tested in the early 1990s favored conventional soliton pulse shaping by using predominant anomalous fiber segments, whereas the stretched-pulse mode-locked fiber laser combined fibers of opposite dispersion signs, thereby introducing huge intracavity temporal breathing dynamics as soon as there is approximate compensation between anomalous and normal dispersions. Such circulation of highly stretched pulses with reduced amplitude allowed researchers to reach pulse energies approaching the nanojoule range, which is much higher than in all-anomalous-dispersion lasers.

To understand the challenge of producing high-energy pulses from a laser oscillator, it is important to know that the Kerr nonlinearity combined with the dispersion generally leads to pulse break-up after the accumulated nonlinear phase has exceeded a certain level. These effects can be circumvented by employing significant temporal stretching of the pulse inside the cavity, thus reducing the peak power while maintaining a large spectral content. This strategy essentially incorporates chirped-pulse amplification inside the laser oscillator [121]–[123].

In the last decade, alternative cavity designs for achieving stable stretched-pulse operation with higher pulse energies has been explored. In 2004, the group led by F. Wise successfully implemented the self-similar propagation of chirped parabolic pulses in the passive part of the laser cavity. This achievement led to an increased pulse-energy performance of nearly 10 nJ per pulse [124]. The implementation of self-similarity inside a cavity relies on a subtle balance between normal dispersion and nonlinearity. These parameters, which act together in a passive fiber, must be balanced

by spectral filtering, nonlinear gain and anomalous dispersion in the laser cavity, thus performing a precise self-consistent pulse reshaping process. Indeed, the acceptance of unusually large intracavity gain and losses, through spectral filtering seems to be the key for entering specific pulse regimes such as self-similarity. Self-similar pulses, also known as similaritons, are forever-expanding pulses that are completely different from the solitons. Interestingly, the transition from similariton to soliton dynamics is performed by a spectral filter, which truncates the pulse in both the spectral and temporal domains. Spectral filtering of a highly chirped pulse has a significant clipping effect on the temporal pulse wings.

When the cavity dynamics become dominated by the composite balance between spectral filtering on one side, and nonlinearity, dispersion and gain on the other side, the tendency of emitting pulses with double-lobe optical spectra is confirmed. Ytterbium-doped mode-locked fiber lasers employing such designs can produce pulses with energies above 20 nJ using standard fiber technology [52], [125], [126]. In these oscillators, the strong dissipative effects per roundtrip are at the heart of pulse formation and stability. Dissipative solitons are found in all-normal dispersion lasers and in lasers with anomalous dispersion, revealing dynamics that are unusual to Schrodinger solitons.

There are currently several trends in the development of high pulse energy mode-locked fiber laser oscillators. Perhaps the most efficient of these relies on the use of advanced technology, in which microjoule-level pulse energies have been achieved by developing large-mode-area gain fibers through microstructuring [127]. Another trend is to shift mode-locking operation further into the normal dispersion regime, thereby increasing the pulse chirping effect [121], [128]. To remain compatible with today's available pumping powers, such strategies are usually supplemented with an increased cavity length to reduce the pulse repetition rate.

Recently, an alternative conceptual approach known as dissipative soliton resonance (DSR) was proposed for increasing the pulse energy [129]–[131]. Found

initially in the frame of the CGLE master equation, DSR describes dissipative solitons that acquire theoretically infinite energy when the equation parameters approach a specific hyper-surface in the parameter space. In practice, this implies that mode-locked laser setups could be designed in which the pulse energy would increase linearly with the pumping power without suffering pulse break-up, within a narrow range of laser parameters. Pulses close to DSR share common features, such as a clamped peak power and a finite bandwidth. Thus, the boost in energy causes the duration of the chirped pulse to increase. A similar approach utilizes a trial function to reduce the CGLE dynamics to a master diagram, which allows a scalable pulse energy to be found [132], [133]. A numerical analysis of the DSR phenomenon in a realistic fiber laser set-up, taking into account gain saturation, provides guidelines for testing the concept experimentally [131], although in such cases high-order physical effects might flatten the resonance effect.

The experimental verification of the feasibility of generating high energy mode-locked pulses directly from the laser cavity has been widely investigated. A common denominator of all the works is the extended length cavities with low repetition rates and the relatively large value of net cavity dispersion. It has also been shown that the high nonlinearity plays an important role in widening the pulse [134]. In the DSR region, the generation of high energy square pulses has been demonstrated regardless the sign of the dispersion or the mode-locking mechanism. Thus, DSR square pulses have been documented in long cavities employing standard monomode amplifiers [134]–[141]. However, due to the limited gain of purely single-mode active fibers in these configurations, the output pulse energy tends to be relatively low in the order of few to hundreds of nanojoules. Therefore, the obvious solution to increase energies of pulses generated in all-fiber lasers would be to use double-clad doped fibers, offering high gain and efficiency. The first demonstration of double-clad Er:Yb laser operating in DSR regime was presented in a F8L all-fiber configuration yielding 2.12 μJ [142]. It was followed by our contributions us-

ing a NPR configuration achieving 2.27 μJ [143] and a F8L double amplifier configuration in the DSR region achieving a record 10 μJ energy per pulse [144]. Recently, a novel Figure-9 fiber laser setup was proposed [145].

4.2 Square-wave pulse (SWP) generation in fiber ring laser setup

The intrinsic feature of DSR mode-locked lasers is the square shape of generated pulses. Duration of the pulses is linearly tunable with pump power delivered to the active fiber, while the peak power remains nearly unchanged. Both theoretical and experimental investigations suggest that parameters of generated pulses should strongly rely on dispersion of the resonator and typically require large values.

In this section, we will investigate the generation of SWP from a double-clad Er:Yb fiber laser mode-locked by the NPR mechanism in the DSR region.

4.2.1 Experimental schematic of a fiber ring oscillator setup

The oscillator setup exhibited in Figure 4:1 is based on a simple all fiber ring cavity configuration operating using the mechanism of nonlinear polarization evolution.

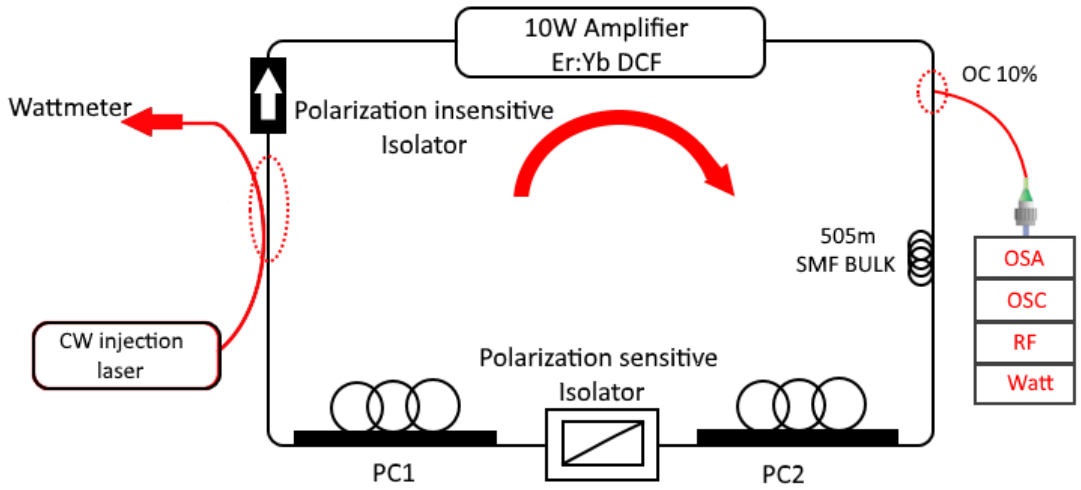

Figure 4:1. Experimental setup of the ring cavity. OC: 10/90 output coupler. PC: polarization controller. OSA: optical spectrum analyzer. OSC: oscilloscope. RF: radio-frequency analyzer. Watt: wattmeter.

To achieve high gain and record output power, we use a C-band double clad V-groove Er:Yb 10 W fiber amplifier from Keopsys. The maximum achievable output power in continuous lasing operation is 10 W, ensured by the 40 W pumping power. Several laser diodes operating at 980 nm pump a 5m-long double-clad fiber that has a second order dispersion of -0.021 $ps^2.m^{-1}$. To ensure large anomalous dispersion together with large pulses duration, we add a piece of 505 m single mode fiber (SMF) so that the net cavity dispersion in the anomalous regime is about -11.872 ps^2. The total cavity length is about 536 m, including 528 m of SMF with a second order dispersion of -0.022 $ps^2.m^{-1}$. The round-trip time of the cavity is 2.681 µs corresponding to a free spectral range of 373 kHz. Two polarization controller (PC) were used with a polarization sensitive isolator to control the nonlinear losses. A polarization-insensitive isolator (PI-ISO) was employed to force unidirectional operation of the cavity. A 10/90 output coupler is used to extract 10% of the power from the cavity. The 10 W amplifier requires a threshold input signal to start. This is a security requirement for protecting the internal optic and electronic circuitry. The external optical signal is delivered by a homemade continuous wave tunable fiber laser with 800 mW maximum output power [109], and is directly injected in the cavity through a 50/50 fiber coupler. Let us mention that once the 10 W laser is operating, the external laser is switched off. In addition, the 10 W amplifier has 2 distinct operating regimes per the datasheet: the low power regime, which requires a minimum input of 17 dBm and a high-power regime for which the gain of the amplifier must be below 13 dB. The output intensity is measured using a high-speed photodetector (TIA-1200), and visualized with a fast oscilloscope (Tektronix TDS 6124C, 12 GHz, 40 GSa). Also, the output power is measured using a high-power wattmeter detector (Coherent Molectron PM500AD). The spectral properties are analyzed with an optical spectrum analyzer (Anritsu MS 9710C) and the pulse duration is measured with an optical autocorrelator with a scanning range of ±100 ps (Femtochrome FR-103 XL). An electronic spectrum analyzer (Rohde & Schwarz FSP Spectrum Analyzer 9 kHz to 13.6 GHz) is used to characterize the radio frequency spectrum of the laser.

4.2.2 High energy 2.27 μJ SWP emission under DSR operational mode

While we visualize the optical spectrum, temporal trace and the RF spectrum, we monitor the output power using the wattmeter. By carefully adjusting the polarization controllers we retrieve mode-locked pulses at a pumping power of P_{pump} = 4W showing a conventional mode locking with sech pulse profile. After having the laser stabilized in mode locked regime, we then slightly adjust the paddles of the polarization controller and by increasing the pump power to 4.8 W, we obtain DSR regime as presented in Figure 4:2. If the polarization controllers are altered during the experiment, we observe other regimes such as multiple solitons [32] or multiple square pulses.

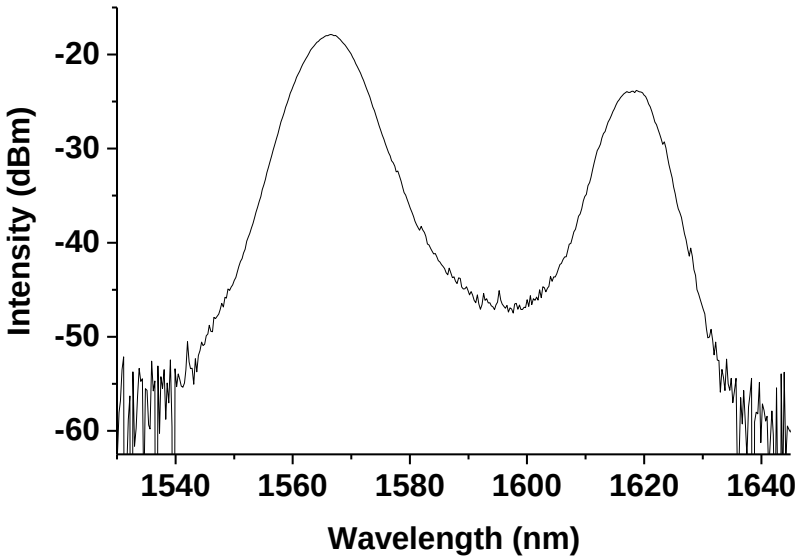

Figure 4:2. Optical spectrum trace of the mode-locked emission at 5.4 W of pumping power.

Figure 4:2 shows the optical spectrum trace of the generated square-wave pulses (SWP) under 5.4 W of pumping power. Such two peaks spectrum has been previously observed in DSR regime but no physical explanation was given [57]. The first band is centered on 1566 nm with 8.5 nm of spectral bandwidth at -3 dB while the second band is centered on 1618 nm with 7 nm of spectral bandwidth at -3 dB. The spectral distance between the central wavelengths is 45 nm. The noise appearing in the wings of the spectrum is linked to the analyzer optical sensitivity characteristics. The autocorrelation trace of the square pulse exhibited in Figure 4:3, points out a constant level because of the low scanning range compared to the pulse duration.

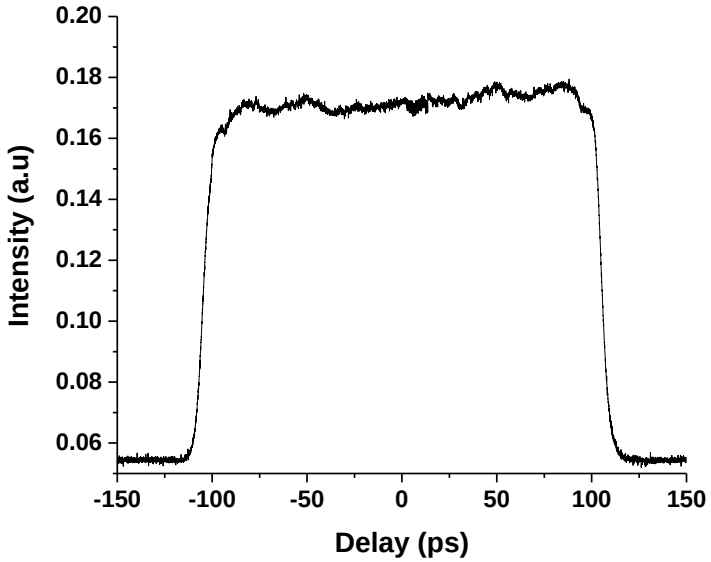

Figure 4:3. Autocorrelation trace of the generated square-wave pulses.

Figure 4:4 depicts the temporal trace of the generated pulses. We notice a peak in the leading edge of the pulse. This behavior has been noticed before but no further investigation has been made in order to understand its nature [146].

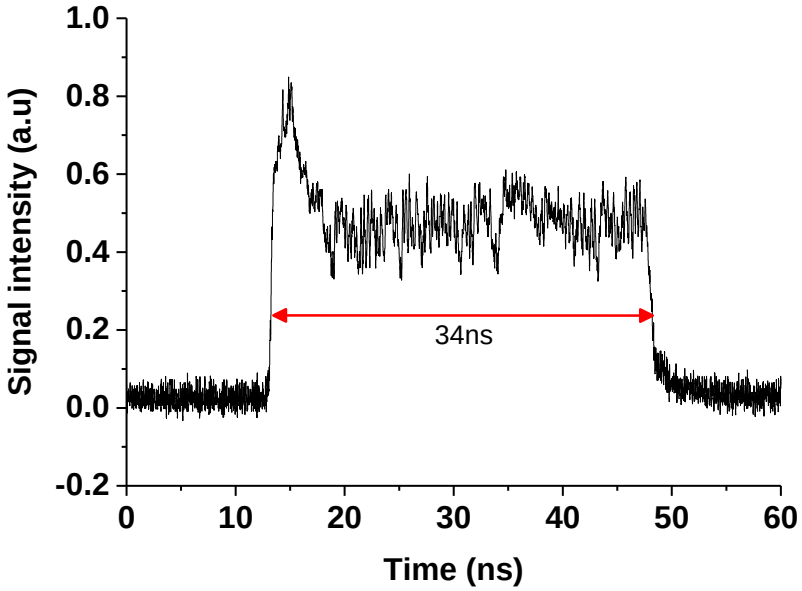

Figure 4:4. Temporal pulse trace of the mode locked emission at 5.4 W of pumping power.

As expected the pulse has a square-shape with a duration of 34 ns. According to Figure 4:5, the RF spectrum shows a signal to noise ratio above 50 dB. The inset exhibits a characteristic modulation with a period of 28 MHz corresponding to the duration of the generated pulses for 5.4 W of pumping power.

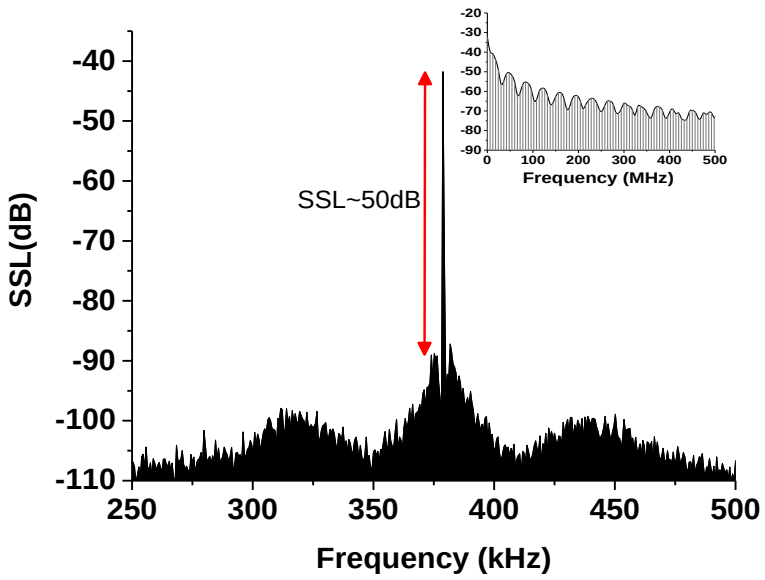

Figure 4:5. At 5.4 W of pumping power: RF spectrum trace with 1 Hz bandwidth, the inset shows the RF spectrum trace with 500 MHz span.

To confirm the existence of only one square pulse and that we did not record the envelop of a bunch of short pulses, we have verified that there isn't a coherent peak with a large pedestal and no fine structure in the autocorrelation spectrum. In addition, our detection apparatus allows us to resolve about 75 ps which is sufficient to visualize any bunch of solitons.

By fixing the polarization controllers, the square-wave pulse is stretched with the increase of the pump power while the peak power remains nearly constant. The evolution of the pulse duration and pulse output energy for fixed polarization controllers is presented in Figure 4:6. We notice that the pulse duration and the pulse energy can be quasi-linearly increased with the pumping power without significantly affecting the peak power.

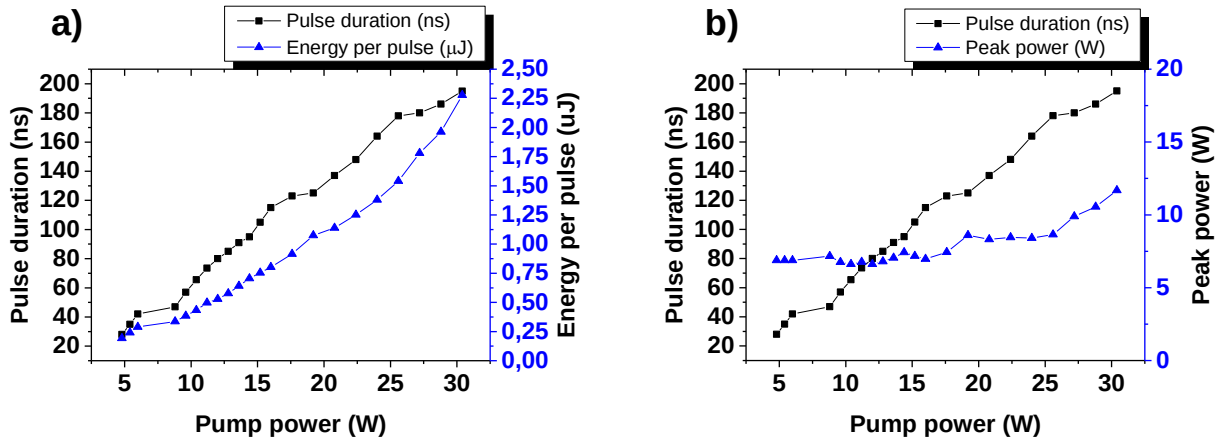

Figure 4:6. (a) Evolution of the pulse duration and energy versus pump power. (b) Evolution of the peak power and pulse duration against pump power.

In fact, the graphs in Figure 4:6 (a) and Figure 4:6 (b) can be divided into 3 regions. For $P_{pump} \leq 7W$ the amplifier operates in the low power regime and the evolution of both the pulse duration and energy is nearly linear. For $7 \leq P_{pump} \leq 26W$ the amplifier operates in high power regime for which the evolution is still linear but with a different slope. Finally, for $P_{pump} \geq 26W$ although there is no modification of the operating regime of the amplifier, there is the emergence of a CW component which requires an adjustment of the polarization controllers to remove it. Such readjustment leads to a variation of the nonlinear losses and then to a modification of the pulse characteristics specially the peak power.

The highest achieved pulse energy is 2.27 μJ and is connected to the fiber coupler used as the output port of the laser. This study is done with a 10/90 output coupler that has significant insertion losses. Considering all these additional losses occurring after the laser output, our pulse output energy would increase if the oscillator's components are carefully optimized. The achieved generated square-wave pulses are tuned in a range from 28 ns to 190 ns as shown in Figure 4:7. We notice that the peak present in the square-wave pulse as mentioned before under low pumping power, disappears while we increase the latter.

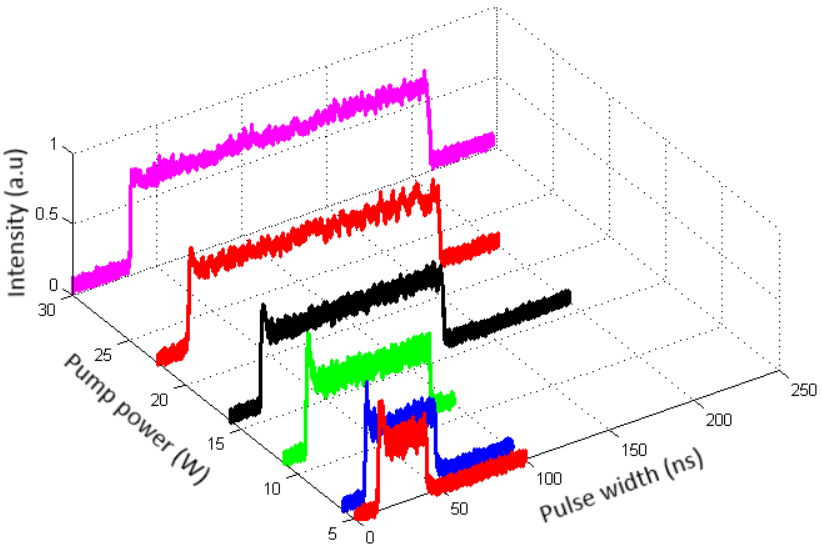

Figure 4:7. Tuning range of the generated DSR square-wave pulse

At a maximum pump power of 30 W, the laser generated a 190-ns square pulse with an output power of 850 mW. At a repetition of 373 kHz, the output pulse energy is 2.27 µJ with 11.5 W of peak power. This is by far the highest output pulse energy ever reported in a fiber oscillator passively mode-locked through nonlinear polarization evolution. It is worth to mention that during our experiment there was no pulse breaking, nor pulse bunching or higher harmonic operation till we passed the 26 W threshold of pump power. In fact, a further increase in the pumping power above 30-W destabilizes the system and we observe wave breaking even by carefully readjusting the polarization controllers. This is not in agreement with theoretical predictions [147].

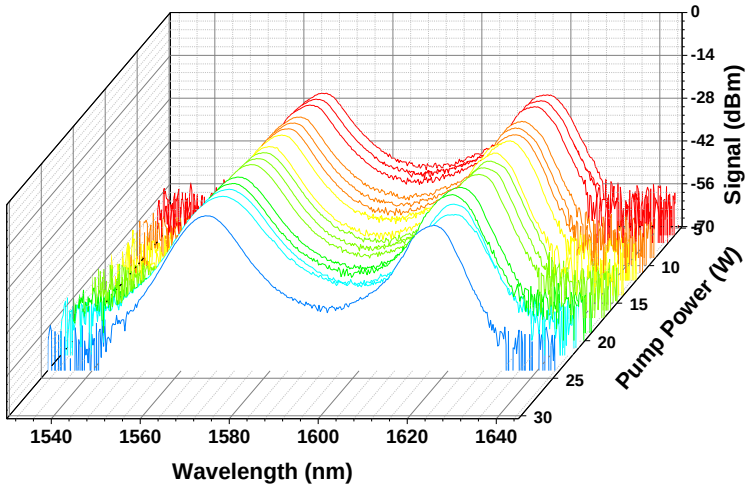

Figure 4:8. Variation of the optical spectrum trace with the change of pumping power

The evolution of the optical spectrum at various pumping power is shown in Figure 4:8. The spectral intensity increases slightly with the pump power while the 3-dB bandwidths of the spectra remain nearly invariable. By increasing the pump power while fixing the polarization controllers under the stable mode-locking operating regime, no significant change in the optical spectrum is observed.

4.3 SWP generation in dual amplifier figure-of-eight fiber laser scheme

Since the DSR effect occurs irrespectively of the employed mode-locking mechanism, experimental verification of this distinctive pulsed mode has been provided for several configurations. In the nonlinear loop mirrors mechanism, Mei et al. demonstrated that the peak power clamping in the dissipative soliton regime can be explained by investigating the NALM transmission as a function of peak pulse power [138]. Conventionally in the DSR region, pulse width and energy can be tuned in certain range whereas the peak power remains at a stable level. By adjusting the gain in both loops, Mei reported that the DSR pulse's characteristics can be controlled independently: the gain in the UR affects only the peak power by keeping the pulse width unchanged, whereas the gain in the NALM allows the tuning of the pulse width without altering the level of the peak power. In this section, we have reexamined the experiment in [138] by introducing double-clad amplifiers instead of the standard amplifiers in both loops, and we compared the obtained results to [138].

4.3.1 Schematic of the F8L using dual amplifiers

The experimental setup shown in Figure 4:9 is based on an all-fiber figure-of-eight laser cavity. It consists of a main unidirectional ring cavity (UR) connected to a nonlinear amplifying loop mirror NALM by a 70/30 fused fiber coupler to have an asymmetric light distribution in both paths of the NALM. The main cavity is composed of a C-band double-clad co-doped Er:Yb 30 dBm fiber amplifier from Keopsys. It is pumped with the v-groove technique by laser diodes emitting about 3 W at 980 nm ensuring around 1.2 W of output power. The double clad fiber (DCF) has a length of

2.45 m and a second order dispersion β_2=-0.021ps^2/m. The wideband polarization insensitive isolator (PI-ISO) is inserted between the amplifier and the output coupler to block the counter-clockwise wave. A 1km SMF coil is inserted after the amplifier to increase the nonlinearities and the round-trip time of the cavity.

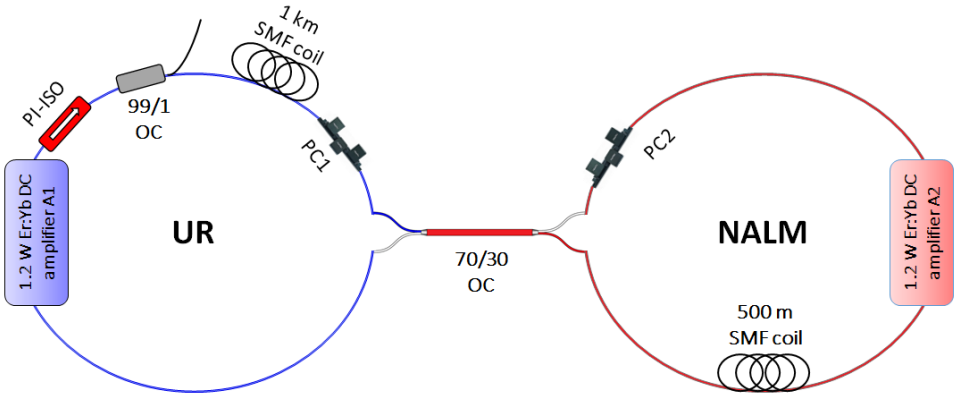

Figure 4:9. Schematic of the dual amplifier laser. OC: output coupler.

The mode-locking is achieved thanks to the intensity-dependent transmission of the NALM [24]. The latter is composed of a C-band double-clad co-doped Er:Yb 30dBm fiber amplifier from Keopsys (KPS-BT2-C-30-BO-FA). It has 8 m of double-clad fiber and two laser diodes operating at 980 nm and emitting about 2.5 W each which guarantees around 1.2 W of output power. A 500 m SMF coil is inserted after the amplifier to increase the asymmetric nonlinear phase shift between the clockwise and counter-clockwise propagating light in the NALM. Two identical polarization controllers are used symmetrically in both cavities to have additional degrees of freedom to improve the mode-locking conditions by adjusting the polarization states. The total cavity length is about 1536 m, including 1500 m of SMF with a second order dispersion β_2=-0.022 ps^2/m. The net cavity dispersion is about -33.23 ps^2 and the round-trip time is 7.65 µs corresponding to a free spectral range of 133 kHz. The output signal is extracted with a 99% output coupler, which allows us to have a maximum output power when the pump power on both sides is extremely high. The spectral properties are analyzed with an optical spectrum analyzer (Anritsu MS 9710C). The temporal trace is detected using a high-speed photodetector (TIA-1200) and visualized with a fast oscilloscope (Tektronix TDS 6124C, 12 GHz, 40 GSa). The output power is measured using a high-power wattmeter detector (Coherent Molectron PM500AD). An electronic spectrum

analyzer (Rohde & Schwarz FSP Spectrum Analyzer 9 kHz to 13.6 GHz) is used to characterize the radio frequency spectrum of the laser. The choice of inserting more fiber in the UR and less in the NALM is not hazardous since it is the result of a thorough optimization of the fiber cavity. Added to that, the usage of a 70/30 fiber coupler in the cavity is based on different experiments to get a good compromise between the stability of the desired square-wave distribution and the maximal energy per pulse [148]. The configuration reported here is the most efficient we have found in view of optimizing the pulse energy without pulse breaking.

4.3.2 High energy 10 µJ SWP emission under DSR operational mode

By pumping 500 mW in the UR and 700 mW in the NALM while adjusting the polarization controllers in both cavities, the mode-locked square-wave pulses can be directly obtained. Below these pumping powers, we don't have mode-locking. If the polarization controllers are altered during the experiment, the established distribution remains stable most of the time till we have a pulse breaking and multiple square pulses appear. Figure 4:10 shows a stable square-wave pulse emission of the laser when the amplifier in the UR is pumped at 3 W and the one in the NALM is at 1.7 W. It depicts the pulse train of the passive mode-locked laser where we have a roundtrip time of 7.65 µs, and an inset of the temporal profile where the pulse width is about 416 ns. At a maximum pump power, we obtain an average output power of 1.333 W leading to an energy per pulse of 10 µJ.

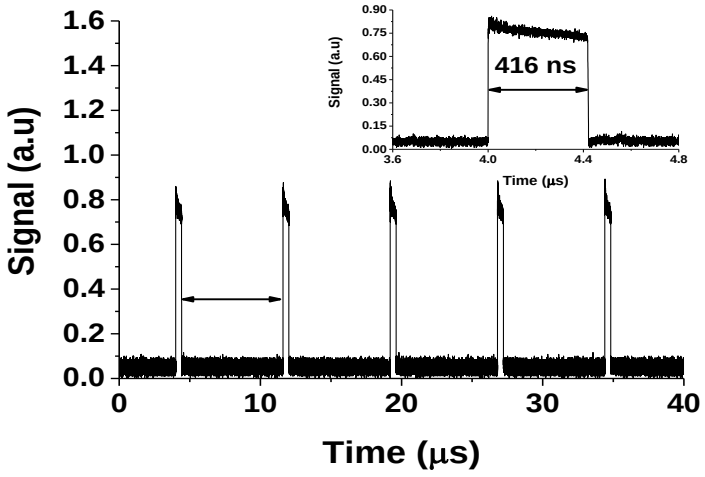

Figure 4:10. Square-wave pulse emission of the laser at a fundamental frequency of 133 kHz and with 4.7 W of total pumping power. a) Pulse train of the temporal trace. b) Temporal profile of single square-wave pulse.

The optical spectrum of the generated pulses is presented in Figure 4:11. The resolution of the spectrum analyzer is 0.03nm, with a video bandwidth VBW of 100 Hz and 10000 sampling points without averaging. In this laser configuration, in contrast to the previous experiment, we have a single wavelength centered on 1565 nm with 4 nm of spectral bandwidth at -3 dB.

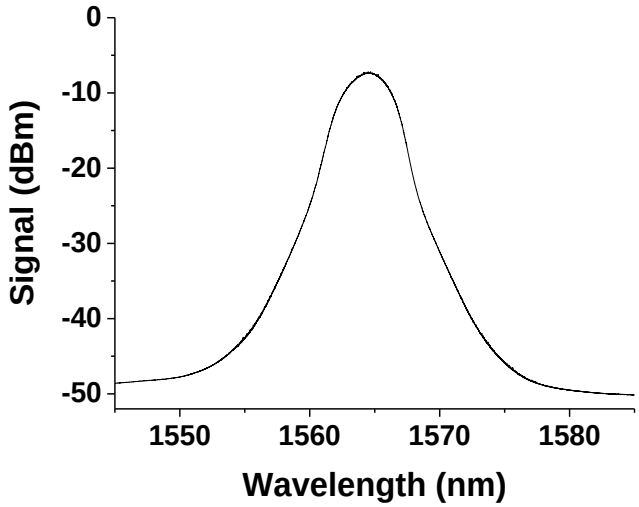

Figure 4:11. Output spectrum of the square-wave pulse at 4.7 W of pump power.

The autocorrelation trace of the square pulse is the same as the previous experiment and it is not represented here. It points out a constant level where there is not a coherent peak nor fine structures confirming that we are not in the presence of noise-like square-wave pulses [149]. Per Figure 4:12, the measured RF spectrum shows a SNR above 60 dB.

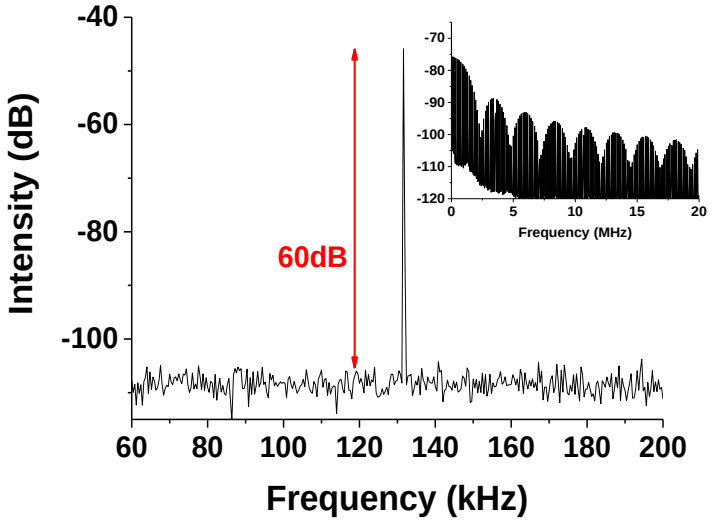

Figure 4:12. RF spectrum of the pulse with an inset of the envelope for a pumping power 4.7 W.

The resolution bandwidth (RBW) of the spectrum analyzer is 100 Hz. The inset exhibits a characteristic modulation with a period of 2.4 MHz corresponding to the duration of the generated pulses for 4.7 W of pumping power.

4.3.3 Control of the pulse's characteristics

By fixing the polarization controllers in the square-wave pulse state, we analyze the dependence of the peak power and pulse width versus the pump power of both amplifiers. The choice of the pumping power of A2 (the amplifier in the NALM) is critical since we can obtain easily a wave-breaking state when the pumping power of A1 (the amplifier in the UR) is at its maximum of 3 W and A2 is pumping above 1.7 W. We start by setting the A2 to 1.7 W and we tune the amplifier A1 from 500 mW to its maximum of 3 W. Experimental results given in Figure 4:13 shows the dependence of the pulse waveform versus A1.

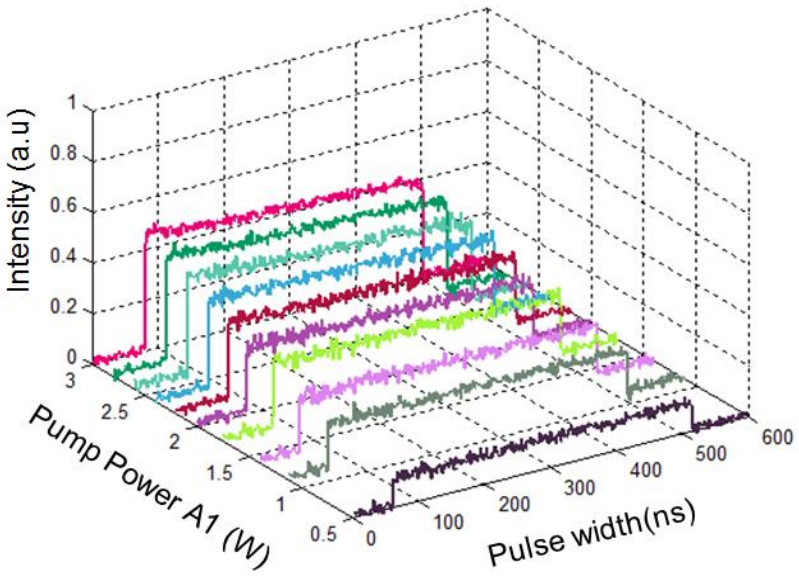

Figure 4:13. Temporal profile of the generated Square-wave pulses with a pump power of A2 fixed at 1.7 W and A1 tuned from 500 mW to 3 W.

When we tune the pump power of A1, the output pulse duration is about 416 ns, keeping almost unchanged and the peak power increases. We measured the output power of the laser, which rose from 250 mW to 1.333 W. Considering the output power, the laser's repeating frequency and the pulse width, we can show that the peak power of the square-wave pulse changes from 5 to around 24 W.

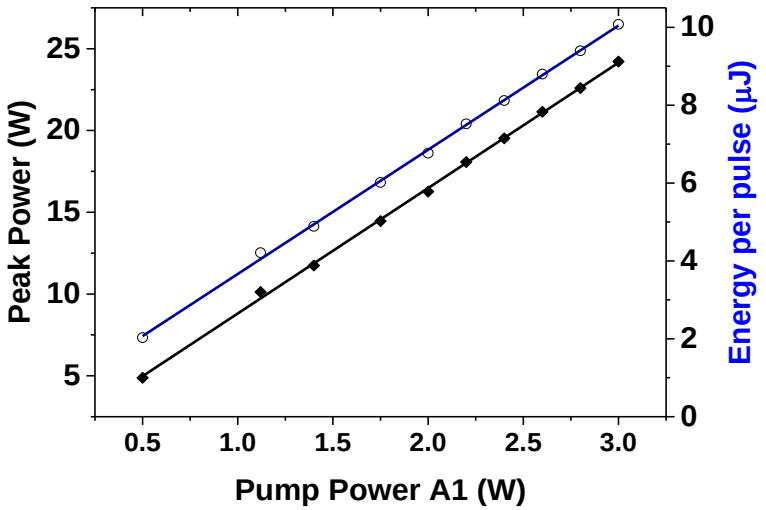

Figure 4:14. Generated Square-wave pulses with a pump power of A2 fixed at 1.7 W and A1 tuned from 500 mW to 3 W. a) Pulse energy (empty circle) and peak power (squares) vs pump power of A1

As it can be seen in Figure 4:14, the pulse energy and peak power vary linearly with the pump power of A1. By increasing the gain in the UR, we increase the peak power of the pulses without modifying the pulse width of the generated square waves in agreement with theoretical [150] and experimental results [138]. In fact, in [138] A1 was turned off after the generation of a stable mode-locked square-wave regime in order to demonstrate the independence of both amplifiers. In contrast, in our experiment, we keep the A1 pumping at a fixed non-zero value and we tune the amplifier A2. The pump power of A1 is set to 3 W and the pump power of A2 varies from 150 mW to 1.7 W.

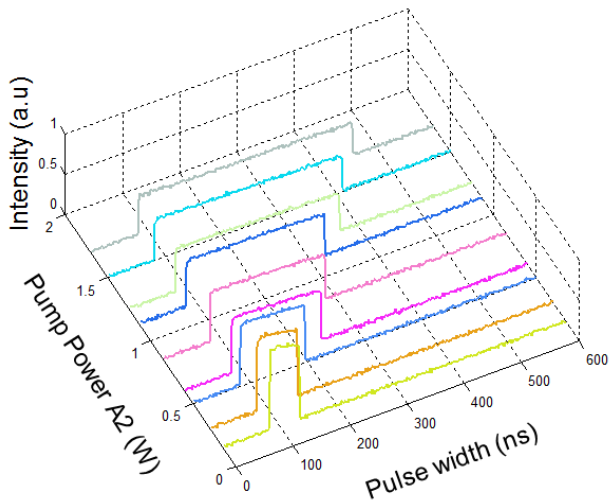

Figure 4:15. Temporal trace of the generated Square-wave pulses with a pump power of A1 fixed at 3 W and A2 tuned from 120 mW to 1.7 W.

Figure 4:15 shows the evolution of the pulse waveform versus A2. When we tune the pump power of A2, the square-wave pulse duration and energy per pulse start increasing linearly as it can be seen Figure 4:16.

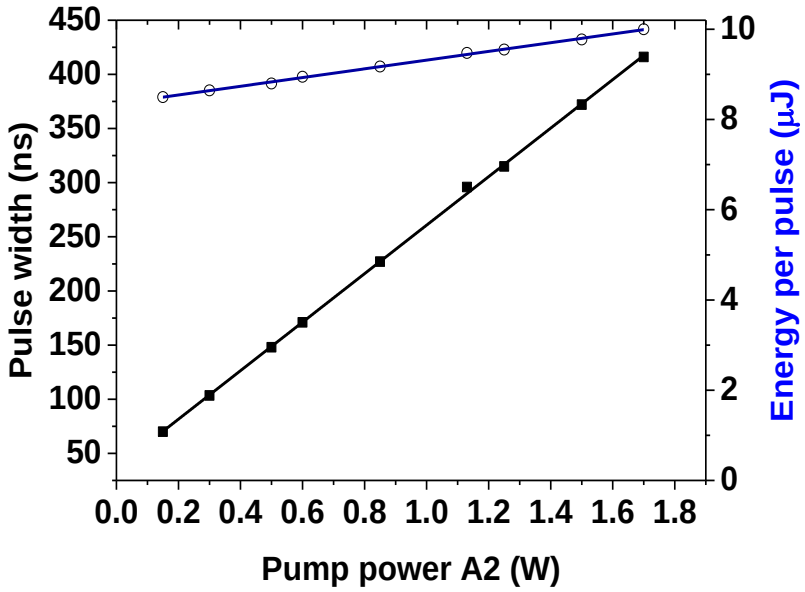

Figure 4:16. Pulse energy (empty circle) and pulse width (squares) vs pump power of A2.

By studying the peak power variation in every point of Figure 4:16 where $P_{peak} = \frac{E_{pulse}}{T_{pulse}}$, we realize that it's decreasing when the pulse width increases because the energy is slowly increasing. Thus, the operation of both amplifiers isn't totally independent in the setup except if A1 is turned off as it appeared in [138]. Indeed, we have verified that in such conditions, we find qualitatively the same results as in [138], i.e. the peak power remains nearly constant while the pulse duration linearly increases with A2. The optical configuration studied in this section has been theoretically investigated in [150] where the authors consider the use of microstructured fiber instead of long SMF fibers. It was theoretically shown that the effect of the amplifiers was independent even when A1 was operating. However, this result was established by a specific set of parameters. Preliminary results of recent simulations seem to demonstrate that for other sets of parameters the effects of the amplifiers are not independent. This behavior must be investigated in more details.

4.4 Multi-pulsing instabilities in dissipative soliton resonance

Multiple experimental results have shown existence of DSR pulses under various cavity configurations, mode locking technique and operating wavelengths. Pulses at 1 µm, 1.5 µm and 2 µm have been demonstrated in both all normal and anomalous dispersion and pulse energy as high as 10 µJ from oscillator is reported [144], [151], [152]. Amplification of DSR pulses to 240 W and 100 W average power at 1 µm and 2 µm respectively have also been demonstrated recently [153], [154]. The generation of high peak power dissipative soliton resonance pulses from linear cavities has also been demonstrated [155]. Rotating the polarization controllers (PCs) DSR pulses with different width and peak power are reported in literature for fiber lasers with both all anomalous and normal dispersion. All the previous experiments have been reported in long or very long cavities, thus low repetition rate.

In this section, we will investigate the generation of SWP in shorter fiber cavities and we will report the existence of multipulsing instabilities in the DSR region that manifests in a harmonic distribution of SWPs.

4.4.1 Mid-length fiber ring cavity employing NPR

The experimental mode-locked laser setup shown in Figure 4:17 is based on a simple all fiber ring cavity exploiting the nonlinear polarization evolution mechanism. We use the double-clad Er:Yb fiber amplifier previously detailed, with a set of polarization controllers and a high-power polarization sensitive isolator PS-ISO to form an artificial saturable absorber. The inline isolator PI-ISO is employed to improve the isolation ratio and the signal is extracted with a 30/70 fiber coupler. We splice a 250-m coil of SMF-28 taking into consideration the interest in operating in large anomalous dispersion of about -6.6 ps^2. The total cavity length is 300 m, including 295-m of SMF with a second order dispersion of -0.022 $ps^2.m^{-1}$. The round-trip time of the cavity is 1.488 µs corresponding to a free spectral range of 672 kHz. The output signal is detected using the same apparatus in the previous experiments. The slow-axis in the PS-

ISO is rejected through a port, which is connected to a high-power wattmeter (Coherent Molectron PM500AD). The laser can operate in different regimes by carefully adjusting the polarization controllers through the variation of both the linear and nonlinear losses of the cavity.

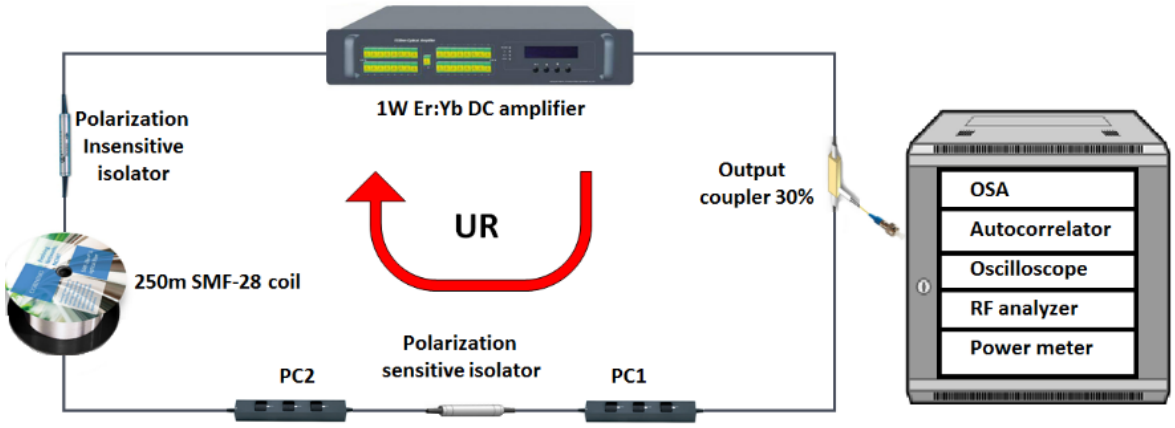

Figure 4:17. Experimental setup of the ring cavity.

4.4.2 Generation of SWP in the DSR region

Stable mode-locking in the square pulse DSR regime was achieved with proper adjustment of the polarization controllers at 400 mW pump power. The pulse repetition rate was 672 kHz matching with the cavity round-trip time. The pulse width was tunable from 95 ns to 270 ns by increasing the pump power at fixed PC orientation while the peak power remains clamped as presented in Figure 4:18.

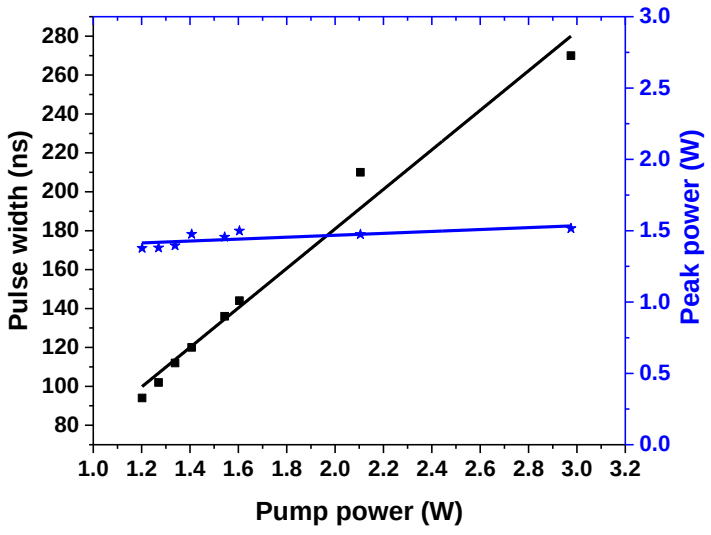

Figure 4:18. Evolution of the pulse characteristics: pulse width and peak power versus pump power (squares for the pulse width, stars for the peak power)

The pulse width and energy per pulse variation with input pump power is shown in Figure 4:19.

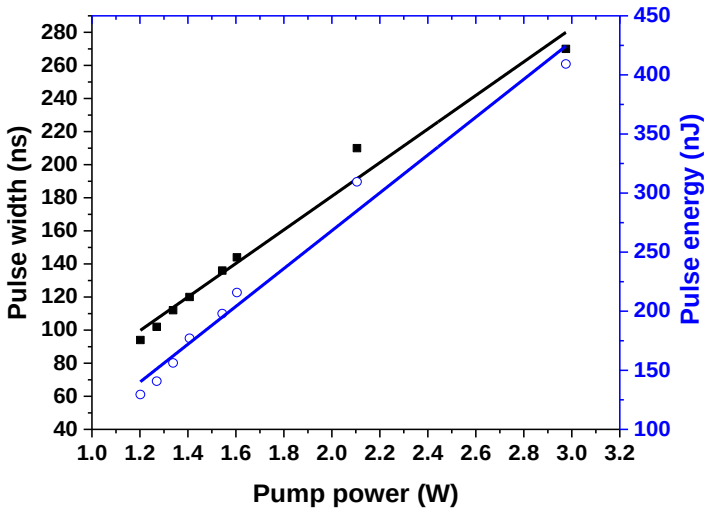

Figure 4:19. Pulse width and pulse energy versus the pumping power (square for pulse energy, empty circles for the pulse width).

We notice that the pulse duration and the pulse energy can be quasi-linearly increased with the pumping power without significantly affecting the peak power. The highest achieved pulse energy and width is 409 nJ and 270 ns respectively and are connected to the fiber coupler used as the output port of the laser. The temporal pulse trace at the fundamental repetition rate is depicted in Figure 4:20.

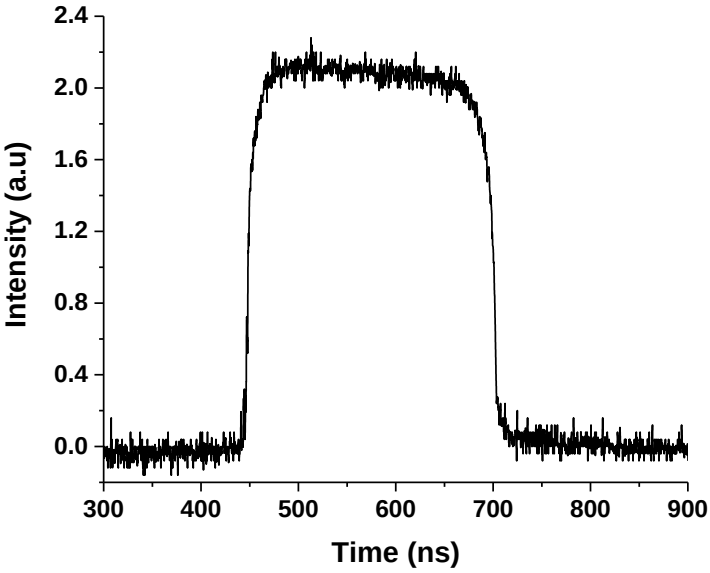

Figure 4:20. Temporal profile of the SWP at 3 W of pump power.

The corresponding spectrum is presented in Figure 4:21. The resolution of the spectrum analyzer is 0.03 nm and the central wavelength is centered on 1566 nm with 3 nm spectral bandwidth at -3 dB.

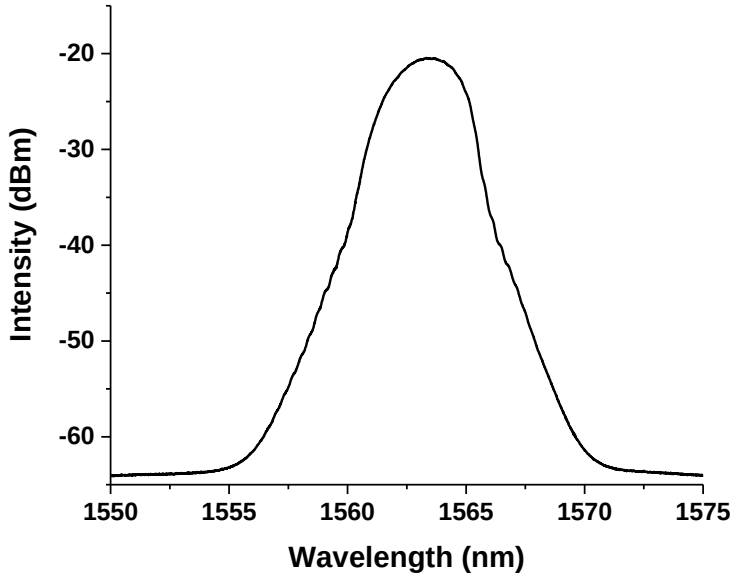

Figure 4:21. Optical spectrum trace of the generated SWP at 3 W of pump power.

In Figure 4:22, the measured RF spectrum shows a signal to noise ratio around 60 dB. The resolution bandwidth (RBW) of the spectrum analyzer is 100 Hz. The inset exhibits a characteristic modulation with a period of 3.71 MHz corresponding to the duration of the generated square pulses for 3 W.

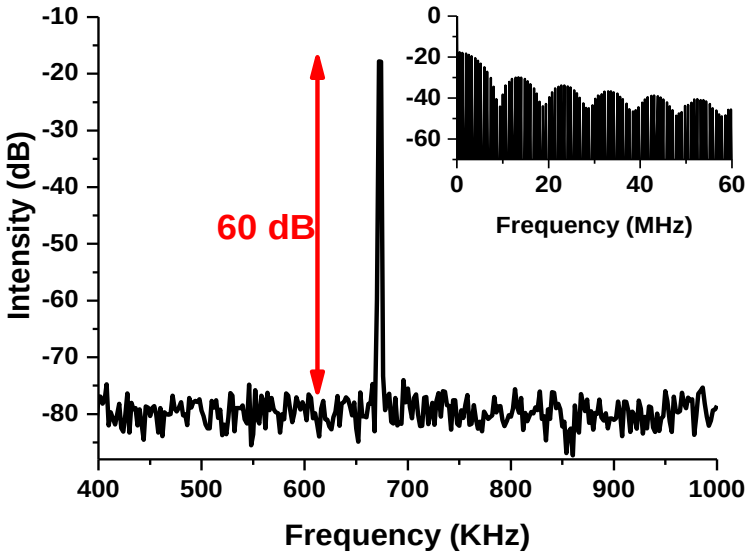

Figure 4:22. RF spectrum trace with 1 Hz bandwidth, the inset shows the RF spectrum trace with 500 MHz span.

As it has been previously demonstrated, we have verified the autocorrelation spectrum and we found no coherent peak nor fine structures thus confirming the existence of only one square pulse. In addition, our detection apparatus allows us to resolve about ±100 ps which is sufficient to validate that we did not record the envelop of a bunch of short pulses.

4.4.3 Multipulsing instabilities: A harmonically distributed SWP under DSR

As mentioned before, by continuously increasing the pump power, the square pulse operating in dissipative soliton resonance regime widens and does not suffer from wave-breaking at a maximum 3 W pump power. When the pump power is fixed and by adjusting properly the PCs, the square pulse packet can split into two or more pulses having the same shape as the original square pulse but with a smaller extent. Consequently, the laser evolves into a higher harmonic DSR mode-locking as shown in Figure 4:23.

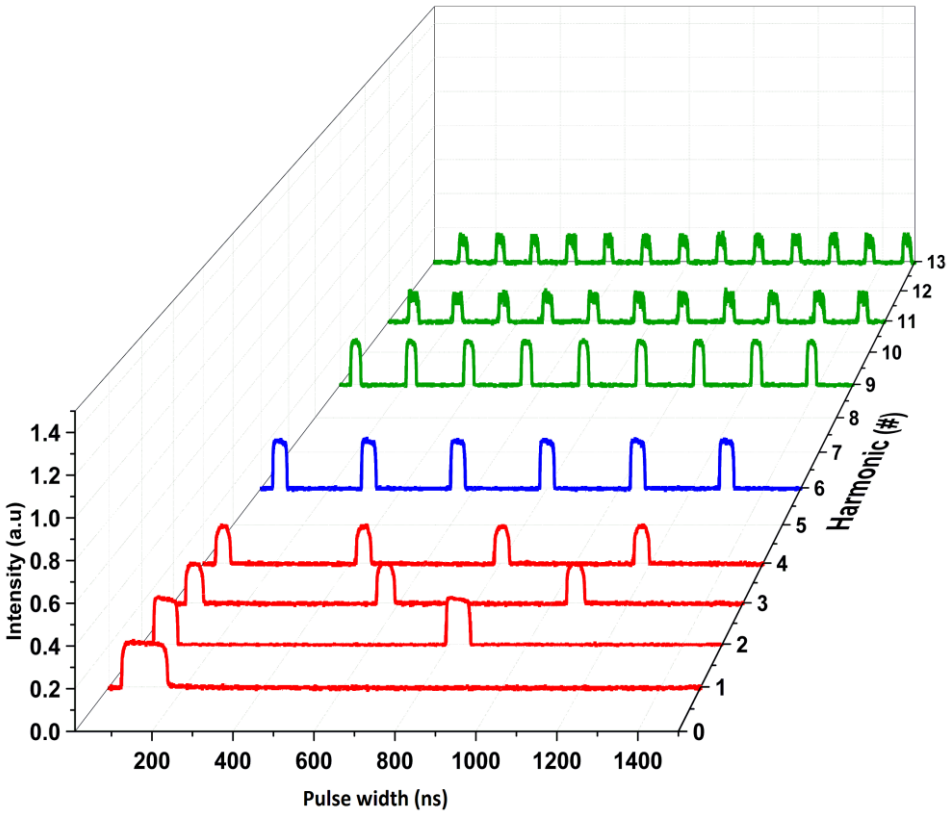

Figure 4:23. Harmonic mode-locked DSR square pulses train of different orders achieved by adjusting the PC. Each color is assigned to different pumping power (red for 1.18 W, blue for 1.6 W and green for 2.2 W).

At a pump power of 1.18 W while modifying the polarization controllers, we achieved up to the 4th harmonic order. This was the maximum harmonic that was being generated by a set of specific parameters. By increasing the pump to 1.6 W, we managed to obtain up to the 6th harmonic order while carefully adjusting the PC. Further increase of the pump power to 2.2 W while conserving the exact same optical spectrum, leads to the generation of several harmonic orders up to the 13th harmonic order. Above this pumping power, no increase in the harmonic order has been detected. The square pulse width ranged from 102 ns at the fundamental frequency to 18 ns at the 13th harmonic order. The autocorrelation trace of the harmonic mode-locked pulses showed no fine structures, indicating that the harmonic mode-locked square pulses were not considered as the envelops of noise-like pulses.

To verify that the achieved HML distribution operates under the dissipative soliton resonance regime, we compared the 4th harmonic order obtained under different pumping powers.

As shown in Figure 4:24, under the 4th harmonic order distribution, when we increase the pump power, the square pulses widen and become more energetic continuously without wave-breaking. The pulse duration increases from around 95 ns to 190 ns whereas the energy from 37 nJ to 70 nJ.

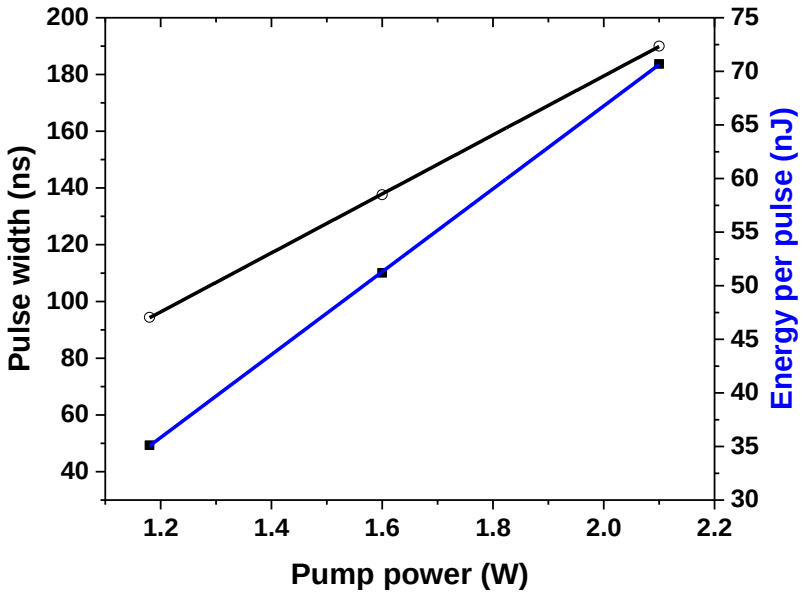

Figure 4:24. Evolution of the 4th order harmonic mode-locked square pulse's characteristics: pulse width and energy versus pump power (empty circles for pulse width, squares for pulse energy).

Also, we measured the peak power during this process as presented in Figure 4:25, and it remained nearly constant when the pulse width is modified.

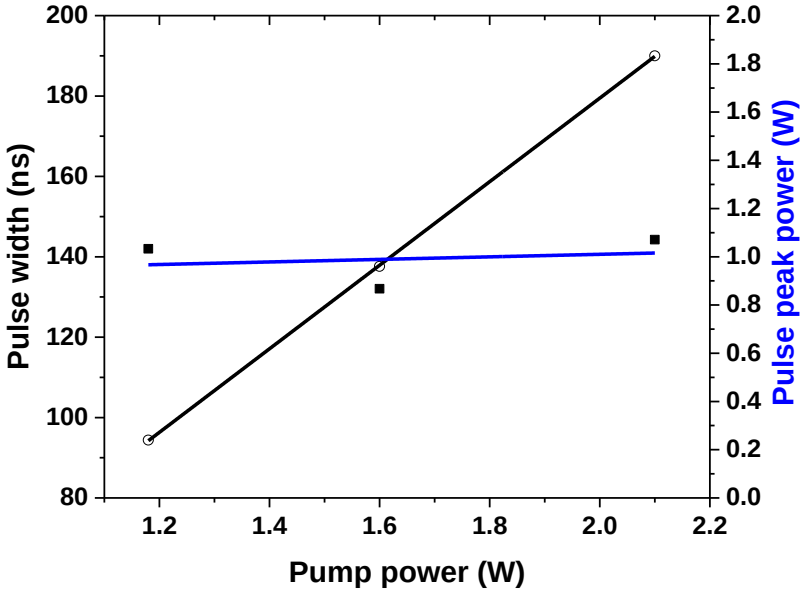

Figure 4:25. Pulse width and peak power versus pump power (empty circles for pulse width, squares for peak power).

We notice that the average output energy per pulse at a fixed pump power of 1.18 W, follows a scaling law of 1/n where the pulse energy is proportional to the harmonic order as described in Figure 4:26. This is mainly since the average output power remains nearly unchanged.

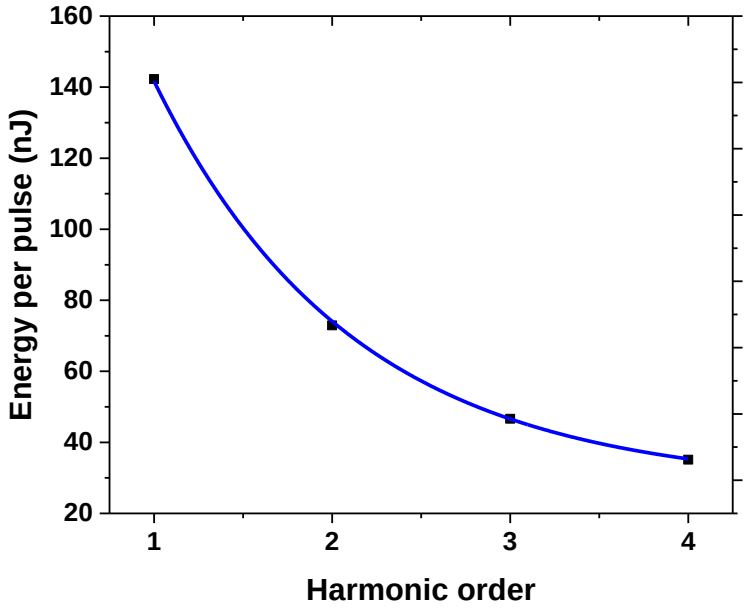

Figure 4:26. Pulse energy versus harmonic order at a fixed pump power. The solid line is a 1/n fit.

4.5 Spectral and temporal dynamics of SWP in fiber lasers

The earlier experiment presented the possibility of generating square pulses operating in the dissipative soliton resonance mode with a variety of cavity configurations. These pulses exhibited a clamped peak power with a tunable pulse width and energy which are the distinct characteristics of the DSR. Meanwhile, Komarov et al. [156] demonstrated recently the possibility of generating the same type of square pulses with a spectral doublet structure. By increasing the pump power in the fiber laser cavity, the pulses manifest the features of the DSR while the spectral lobes' 3 dB bandwidth and positions remain unchanged. In this section, first we will demonstrate an experimental observation of such behavior which could help a better understanding of the pulse dynamics in the dissipative soliton resonance regime. Then, we will report the generation of staircase pulses with spectral doublet structures.

4.5.1 Experimental schematic of a ring cavity oscillator

In this experiment, we use the same fiber setup as the previous section. It is a simple all fiber ring cavity using the NPR as mode-locking mechanism as shown in Figure 4:27. To achieve high gain and high output power, we use the C-band double clad V-groove Er:Yb 1.2 W fiber amplifier. To ensure large anomalous dispersion together with large pulses duration, we add 240 m of SMF with a second order dispersion of -0.022 $ps^2.m^{-1}$, so that the net cavity dispersion in the anomalous regime is about -5.49 ps^2.

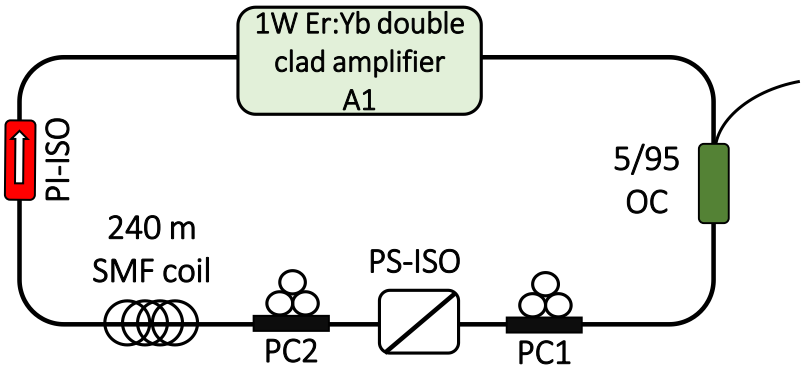

Figure 4:27. Experimental setup of the nonlinear polarization evolution: isolator (PI-ISO), PC (polarization controller), PS-ISO (polarization sensitive isolator), OC (output coupler).

The total cavity length is about 250 m. A 5/95 output coupler is used to extract 5% of the power from the cavity. The output intensity is measured using the same apparatus described in the previous sections.

4.5.2 Spectral dynamics of square pulses

When the polarization controllers' paddles are properly adjusted, mode-locked pulses are observed at the output of the laser for pump powers above 200 mW. Figure 4:28 shows the analysis of pulses generated by the laser while being pumped with 633 mW of pump. The pulse width obtained is up to 78 ns.

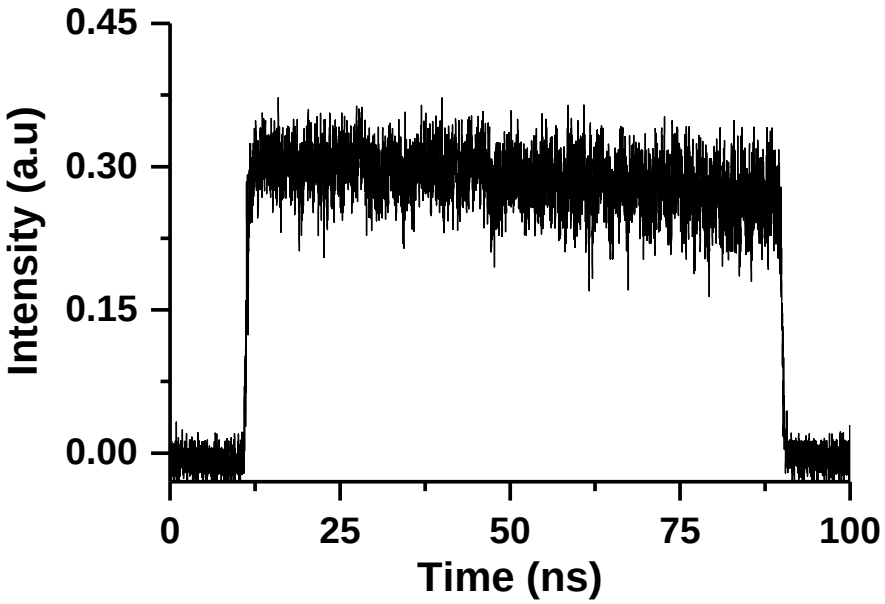

Figure 4:28. Temporal profile of the laser emission registered at 633 mW of pump power.

The purpose is not to demonstrate the generation of DSR pulses [143], [157], [158] but to study the spectral dynamics of these pulses. We choose to analyze the results at 633 mW even if our amplifier can be pumped up to 5 W. Per the registered RF spectrum in Figure 4:29, the signal to noise ratio exceeds 50 dB, and the repetition frequency of the constructed laser is ~800 kHz which corresponds to a ~250 m long cavity.

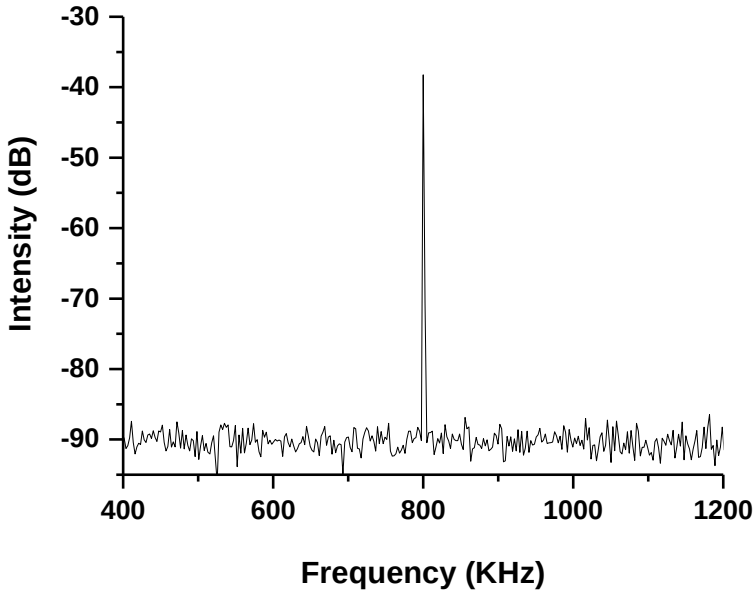

Figure 4:29. RF spectrum registered with 100 Hz BW at 633 mW of pump power.

The graph depicted in Figure 4:30 clearly shows that the average output power, pulse energy and width can be linearly tuned with pump power, while maintaining relatively stable peak power. The achieved pulse tuning ranges from 23 ns to 79 ns, and the pulse energy from 12 nJ to 37.5 nJ by taking into consideration a repetition frequency of 800 kHz. The peak power is clamped around 0.55 W.

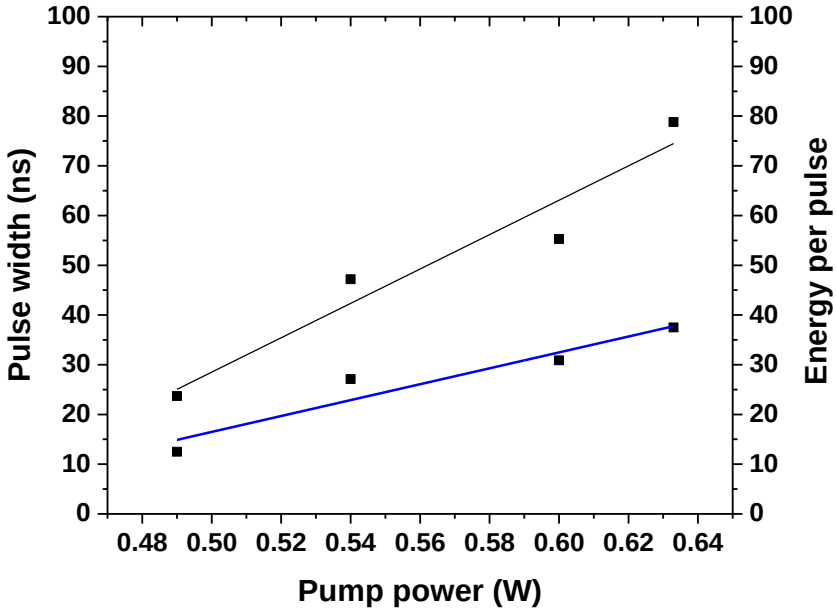

Figure 4:30. Pulse width, energy in function of pump power.

According to Komarov [156], stable square pulses with a spectral doublet can be achieved in fiber lasers and the pulse width tuning and energy scaling is determined by the spectral dynamics. In fact, it has been demonstrated that while increasing the pump power in the anomalous dispersion regime, the spectral width of the doublets is decreased while the position remains unchanged. Figure 4:31 exhibits the spectral profile of the laser emission in function of the pump power.

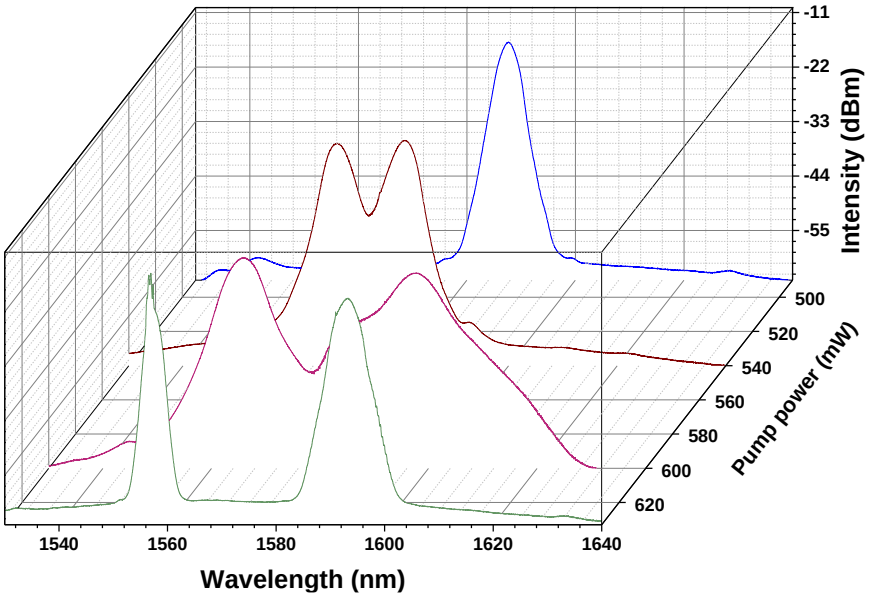

Figure 4:31. Spectral distribution in function of the pump power.

At 490 mW pump power, the spectrum is centered on 1587 nm with a band-width at -3dB of 3 nm. At 540 mW of pump power, the spectrum presents double lobes. First lobe λ_1 is centered at 1568 nm with 2.95 nm bandwidth at 3 dB, and the second lobe λ_2 is centered at 1581 nm with 3.5 nm bandwidth at 3 dB. When the pump power is increasing to 600 mW, λ_1 and λ_2 are centered at 1566 nm and 1598 nm, while their bandwidth at 3 dB is 6.7 nm and 5.85nm respectively. When we reach 633 mW of pump power, λ_1 and λ_2 are centered at 1566 nm and 1602 nm, whereas their bandwidth at 3 dB is 1.2 nm and 5.3nm respectively. It is convenient to represent the evolution of the spectral peaks as a function of the pump power as shown in Figure 4:32.

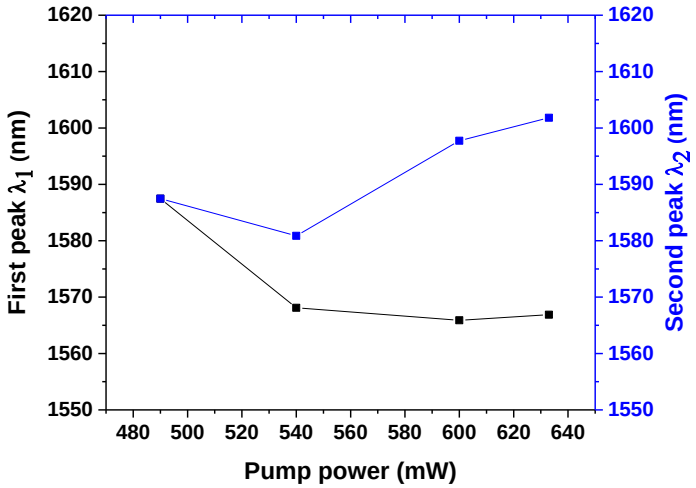

Figure 4:32. Position of the first and the second spectral lobe in function of the pump power.

In Figure 4:32, the lines connecting the points have no representation value, but are used as a guide to the readers' eyes. The region, in which we have explored the spectral lobes shifting, is 150 mW above the threshold of DSR mode-locking. In this zone, we can notice a smooth transition from a single wavelength to a splitting of the central wavelength into two wavelengths. In [156], Komarov et al. did not notice this behavior probably because they did not investigate the restrained zone above the threshold. To be able to compare both numerical and experimental results, we need to have more experimental points above 640 mW to see if the spectral doublets remain constant, and more numerical points between the threshold and the first doublet representation to confirm the obtained experimental results in this section. Correspondingly, there is a small shift in the spectral profile of some nm because the spacing between both lobes is increasing.

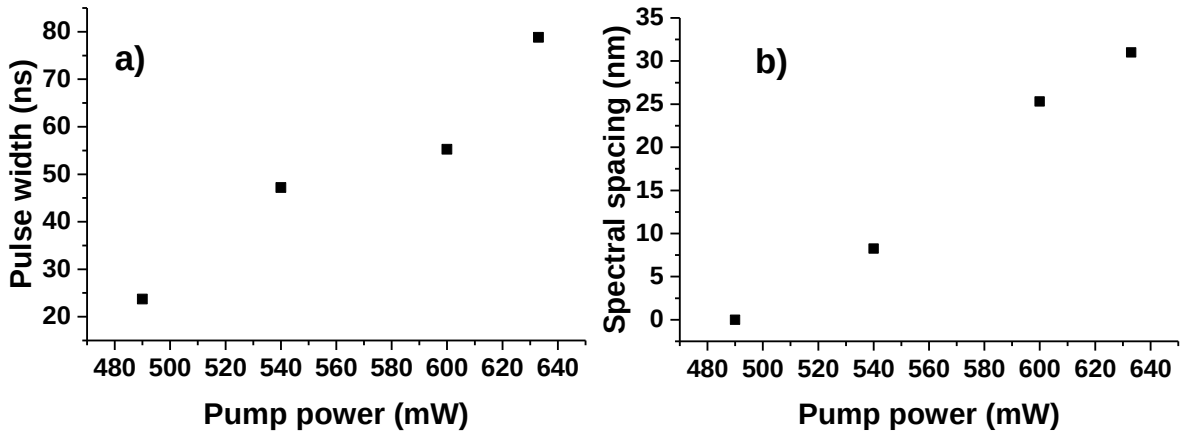

Figure 4:33. a) Pulse width and b) spectral spacing in function of pump power.

As the pump power increases, the pulse width increases linearly as shown in Figure 4:33.(a) whereas the intensity level of λ_1 remains higher than the one of λ_2 and the spectral spacing between them varies as it is demonstrated in Figure 4:33.(b).

We have also examined the temporal profile of the generated square pulses as a function of the pump power. The corresponding results depicted in Figure 4:34 demonstrate the tuning of the pulse width from 23 ns to 79 ns in function of the pump power. These results are in total agreement with the numerical simulation in [156].

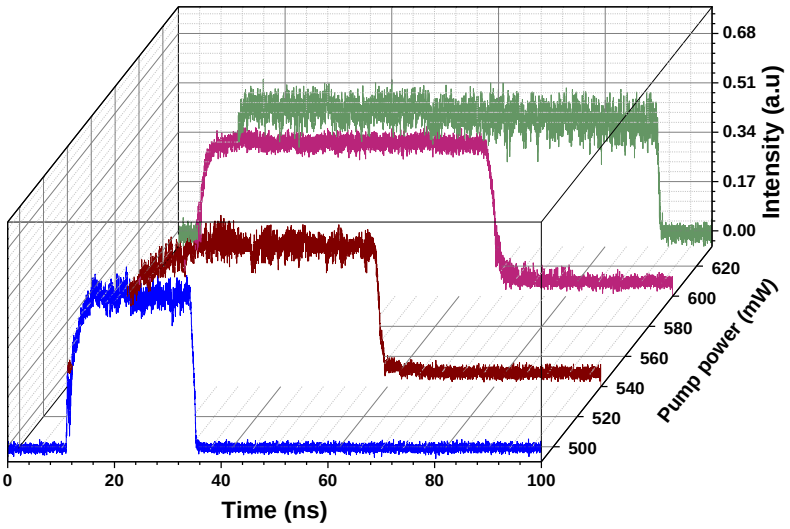

Figure 4:34. Temporal distribution in function of the pump power.

4.5.3 Generation of staircase pulse based on spectral doublet

Based on the same experimental setup in the previous section, we change the output coupler from 5 to 10%. By carefully adjusting the polarization controllers we retrieve mode-locked pulses at a pumping power of P_{pump} = 200 mW showing a conventional mode locking with sech pulse profile. After having the laser stabilized in mode locked regime, we then slightly adjust the paddles of the polarization controller and by increasing the pump power to 2 W, we obtain DSR regime. If the polarization controllers are altered during the experiment, we observe other regimes such as multiple solitons or multiple square pulses. At 2 W of pump power, the temporal trace of the generated output pulse is depicted in Figure 4:35.

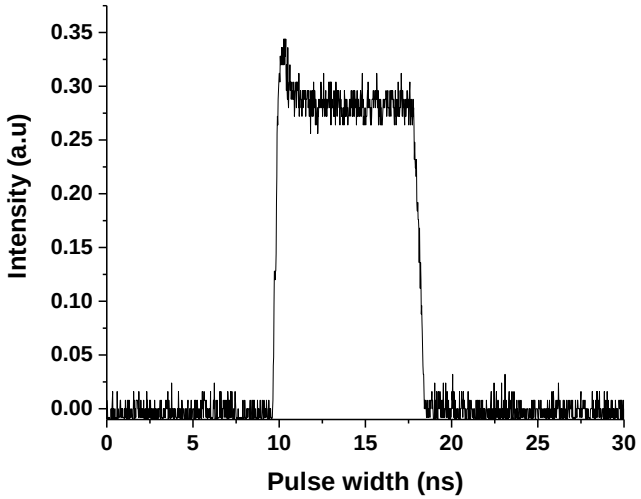

Figure 4:35. Temporal distribution of square pulse at 2W of pump power.

We notice a peak in the leading edge of the pulse as it has been reported previously [143]. The pulse has a square-shape and a pulse width of 8.3 ns. The optical output power recorded is 211.2 mW which leads to a pulse energy of 285 nJ and a peak power of 47.5 W. Figure 4:36 shows the optical spectrum trace of the generated square pulses under 2 W of pumping power. Such two peaks spectrum has been previously observed in DSR regime and have been theoretically predicted [156].

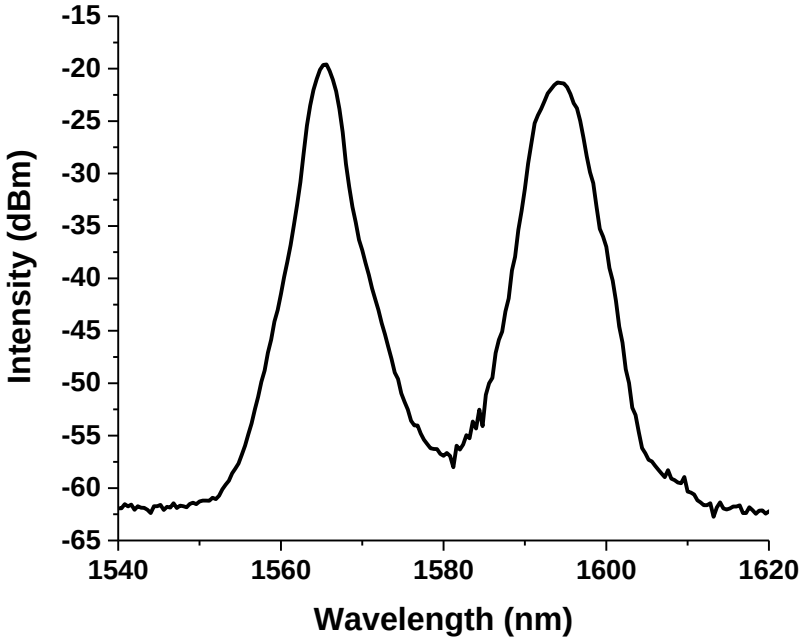

Figure 4:36. Spectral profile of the generated square pulses at 2W pump power.

The first band is centered on 1566 nm with 5 nm of spectral bandwidth at -3 dB while the second band is centered on 1593 nm with 7 nm of spectral bandwidth at -3 dB. The

spectral distance between the central wavelengths is 23 nm. The autocorrelation trace of the square pulse not represented here, points out a constant level because of the low scanning range compared to the pulse duration.

By carefully adjusting the polarization controllers' paddles, we notice that the square pulse is altered and becomes a downward staircase wave as depicted in Figure 4:37.

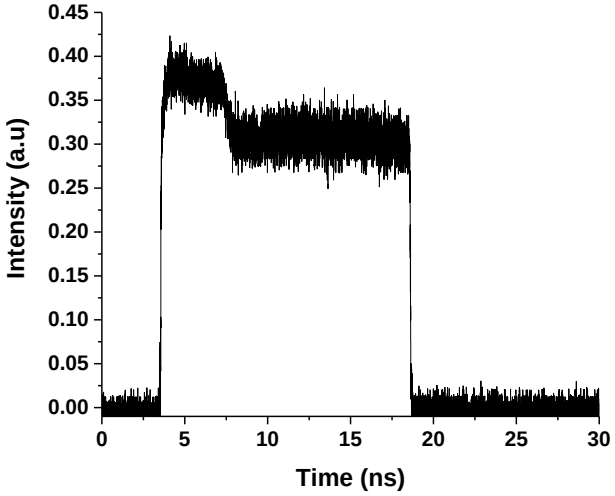

Figure 4:37. Temporal trace of the downward staircase pulse.

The obtained pulse width is 15 ns. The pulse presents two different intensity levels where the first part has 4 ns width and second part has 11 ns. The recorded output power is 200 mW and the pulse energy is 270 nJ. The spectral profile of such pulse is presented in Figure 4:38.

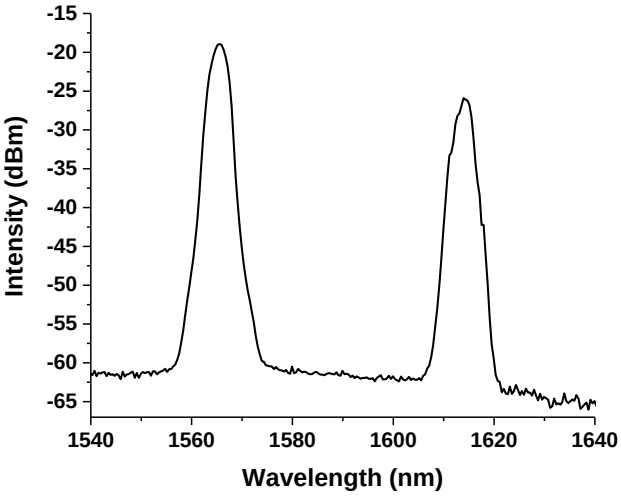

Figure 4:38. Spectral profile of the downward staircase pulse.

The spectrum presents as in Figure 4:36 two lobes centered on 1565 nm and 1615 nm with a -3dB bandwidth of 4 nm and 3.2 nm respectively. Compared to the previous obtained spectrum in Figure 4:36, the spectral separation between both lobes has increased to 45 nm.

We continue adjusting the polarization controller to search for the existence of an upward staircase pulse. Figure 4:39 exhibits the temporal profile of an upward staircase pulse. The total pulse width is 12 ns, where the first is about 5 ns and second part has a width of 7 ns. The recorded output power is 199 mW and the pulse energy is 268.5 nJ.

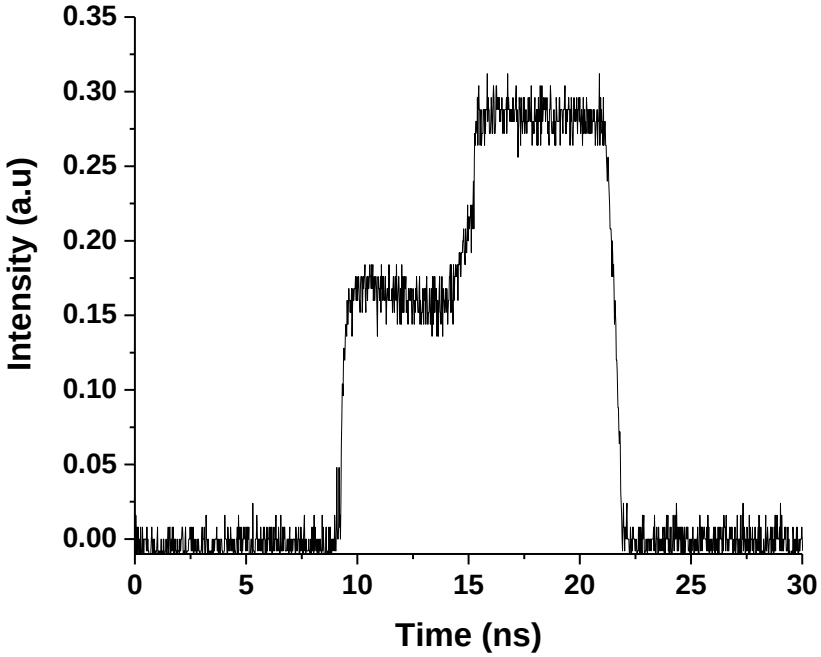

Figure 4:39. Temporal trace of the upward staircase pulse.

Let us note that this state is observed only in a very restrained range of parameters (very narrow pump power range and specific position of the PCs paddles). Figure 4:40 exhibits the spectral profile of the generated upward staircase pulse.

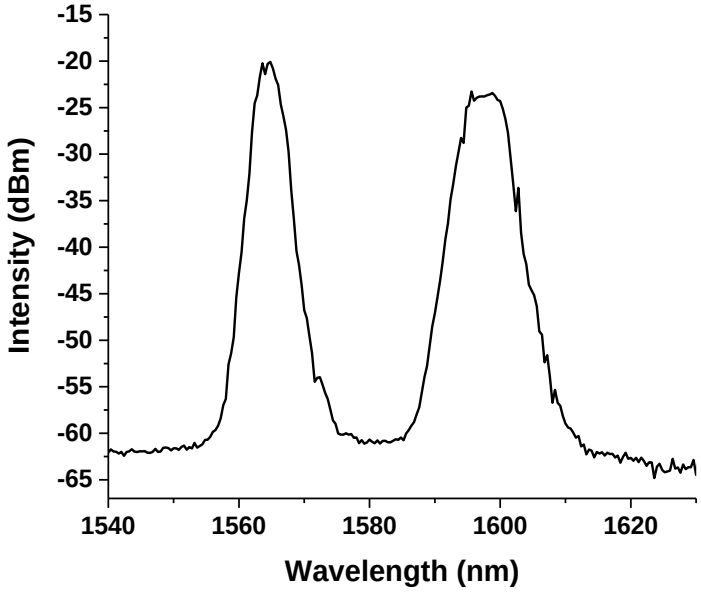

Figure 4:40. Optical spectrum of an upward staircase pulse.

Like the previous results, there is also two lobes. The first one is located at 1565 nm with 4 nm bandwidth at -3 dB while the second is located at 1598 nm with 6 nm bandwidth at – 3dB. The separating distance between both wavelengths is around 26 nm. Based on the obtained results, we notice that the spectral distance between both wavelength varies. In fact, in the case of a single pulse $\Delta\lambda = 28\,nm$ whereas in the case of downward and upward staircase pulse $\Delta\lambda = 50\,nm$ and $\Delta\lambda = 33\,nm$ respectively. At this stage of analysis since we have few points, we cannot deduce a scale law that validates a certain relation between spectral spacing and pulse width. More experiments need to be achieved.

4.5.3.1 Spectro-temporal analysis of the obtained results

To investigate the square peak appearing in the leading edge of the pulse in Figure 4:37 , a flexible tunable filter OTF 320 manufactured by SANTEC, with a spectral bandwidth of about 0.5 nm and threshold damage of 320 mW is inserted after the output coupler. By simple filtering the optical signal, we noticed that the pulse width is 4 ns when we are at 1565 nm and it is 15 ns when we are at 1615 nm. So basically, we can assume that the resulting output pulse, is the combination of two wavelengths in different spectral bands as it is presumed in Figure 4:41.

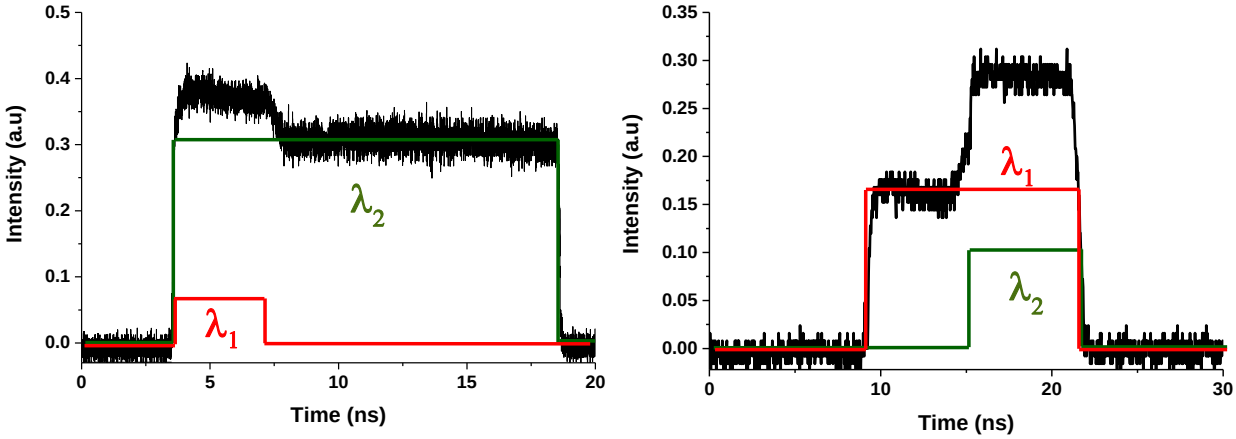

Figure 4:41. Spectro-temporal analysis of the staircase pulses.

These results are preliminary, and more investigation needs to be done to confirm the filtering of the output pulse and the link between the spectral spacing of the lobs and the pulse width in function of the pump power.

4.5.3.2 Staircase pulse numerical simulation

Previously, we have experimentally demonstrated the possibility of generating staircase pulses in a Er:Yb co-doped double-clad fiber laser passively mode-locked with nonlinear polarization evolution mechanism. As A. Komarov conducted the numerical simulations, we used the following normalized master equation describing the field evolution in a unidirectional ring laser:

$$\frac{\partial E}{\partial \zeta} = (D_r + iD_i)\frac{\partial^2 E}{\partial \tau^2} + D_{i3}\frac{\partial^3 E}{\partial \tau^3} + [g - \sigma_0 + (p+iq)I - p_2 I^2]E \qquad \text{Eq. 35}$$

where $E(\zeta,\tau)$ is the electric field amplitude, τ is the time coordinate in units $\delta t = \sqrt{\frac{|\beta_2|L}{2}}$ (here β_2 is the second-order group-velocity dispersion for the intracavity medium and L is the cavity length), ζ is the normalized propagation distance (the number of passes of the radiation through the laser cavity), D_r and D_i are the quadratic frequency dispersions of the gain-losses and the refractive index respectively and D_{i3} is the third order dispersion of the refractive index. The amplification is expressed

as $g = \dfrac{a}{1 + b\int I\, d\tau}$ in which the integration is carried out over the whole round-trip period, where a is the pumping parameter, b is the saturation parameter, and $I = |E|^2$ is the field intensity in units $(\gamma L)^{-1}$. The dimensional nonlinear refractive coefficient γ related to the nonlinear refractive index is expressed in $W^{-1}m^{-1}$. The parameter σ_0 is the linear losses and q is the Kerr nonlinearity. The term pI describes the nonlinear losses that decrease with increasing intensity I whereas $p_2 I^2$ is due to nonlinear losses that increase with increasing I .

When $D_{i3} = 0$, the master equation describes the generation of spectral-doublet square pulses which has been demonstrated experimentally in the previous section, and numerically in [156]. Typical temporal and spectral distributions of such pulses are presented in Figure 4:42. The right and left parts of the pulse in Figure 4:42(a) have different carrier frequencies which correspond to the two spectral peaks in Figure 4:42 (b). The peak in the center of the pulse in Figure 4:42 (a) is the result of the in-phase interference fields from the right and left parts of the pulse. The temporal and spectral distributions are symmetric.

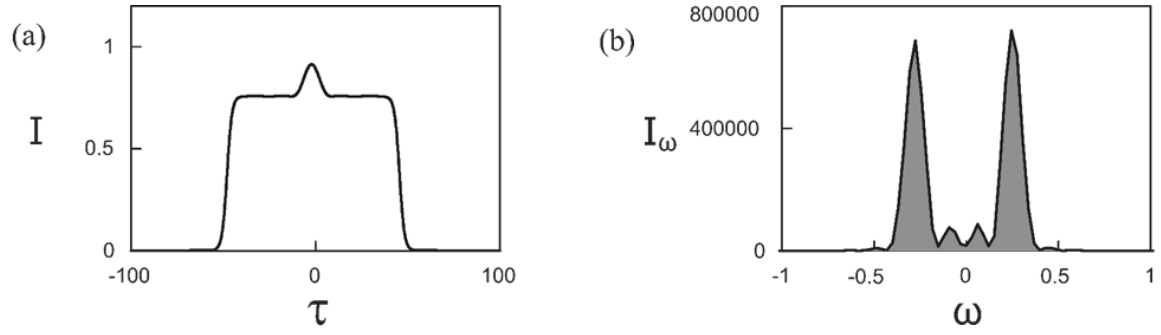

Figure 4:42. (a) Temporal and (b) spectral distributions for a steady-state rectangular pulse with spectral doublet structure. a=2.5, b=0.07, D_r=1.4, D_i=0.2, D_{i3}=0, σ_0=0.5, p=1, q=0.45, p_2=1.

The third order nonlinear dispersion of the refractive index D_{i3} breaks the symmetry. In this case, the master equation is not invariant relatively to the replacement τ by $-\tau$. The example of the transient evolution for a lasing operation with $D_{i3} \neq 0$ is presented in Figure 4:43. In this case the pulse may have a staircase shape. The upper and lower parts of the step correspond to the different peaks of the spectral

doublet. However, such staircase pulse is unstable. The boundary separating the fields with different carrier frequencies (the peak in the temporal distribution of the pulse) shifts to the edge of the pulse. Thus, the pulse becomes a single frequency one. This transient evolution is due to a competition between two fragments of the pulse which are supported from the single energy source connected with the amplification g. A fragment of the field having the best conditions for generation dominates the competition. An alternative fragment is suppressed. Numerous attempts to determine a mechanism stabilizing the staircase pulse had been taken. It has been demonstrated that such stabilization may be due to the spectral gain inhomogeneity in fiber amplifiers.

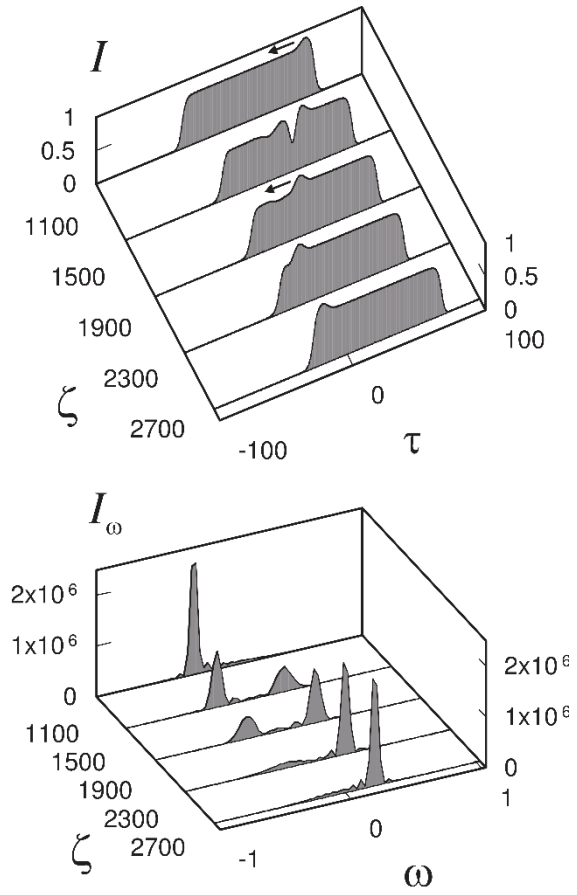

Figure 4:43. Transient process and the steady-state distributions (a) for the intensity $I(\tau)$ and (b) for the spectrum of a rectangular pulse in the case of a=2.5, b=0.07, D_r=1.4, D_i=0.2, $D_{i3}\neq 0$, σ_0=0.5, p=1, q=0.45, p_2=1. ($D_{i3}=-1$ for $\zeta \leq 1100$, $D_{i3}=1$ for $\zeta > 1100$).

Similar to the previous simulation, we use the same standard split-step Fourier method involving splitting the nonlinear-dispersion problem into nonlinear and dispersion parts [159]. The nonlinear equation was the same as in the case of the master equation:

$$\frac{\partial E}{\partial \zeta} = [g - \sigma_0 + (p + iq)I - p_2 I^2]\, E \qquad \text{Eq. 36}$$

The equation for the Fourier components of the field E_ω describing the dispersion part of the task has the form:

$$\frac{\partial E_\omega}{\partial \zeta} = -\omega^2 \left(D_r + iD_i\right) E_\omega - i\omega^3 D_{i3} E_\omega + \\ + \left(g_1 \exp\left[-D_0(\omega - \omega_1)^2\right] + g_2 \exp\left[-D_0(\omega - \omega_2)^2\right]\right) E_\omega \qquad \text{Eq. 37}$$

where ω_1 and ω_2 are the central frequencies for peaks of a spectral doublet. The parameter D_0 determines a spectral homogeneous width of an amplification. The terms proportional to $\exp\left[-D_0\left(\omega-\omega_1\right)^2\right]$ and $\exp\left[-D_0\left(\omega-\omega_2\right)^2\right]$ describe a spectrally inhomogeneous amplification near the frequency ω_1 and ω_2 , respectively [160], [161]. The values g_1 and g_2 correspond to the value of g described earlier and are determined by the expression:

$$g_i = \frac{h_i}{\left(1 + b_i \int I_\omega \exp\left[-D_0(\omega - \omega_i)^2\right] d\omega\right)} \quad , \quad i = 1, 2, \ldots \qquad \text{Eq. 38}$$

In the case of a spectrally inhomogeneous amplification, the wings have different frequencies and they are supported by independent sources which are described by the values g_1 and g_2. Therefore, the competition between these fragments of the field is suppressed, their coexistence is achieved, and the steady-state staircase pulse is stabilized. The temporal and spectral distributions of the downward stable steady-state staircase pulse are shown in Figure 4:44.

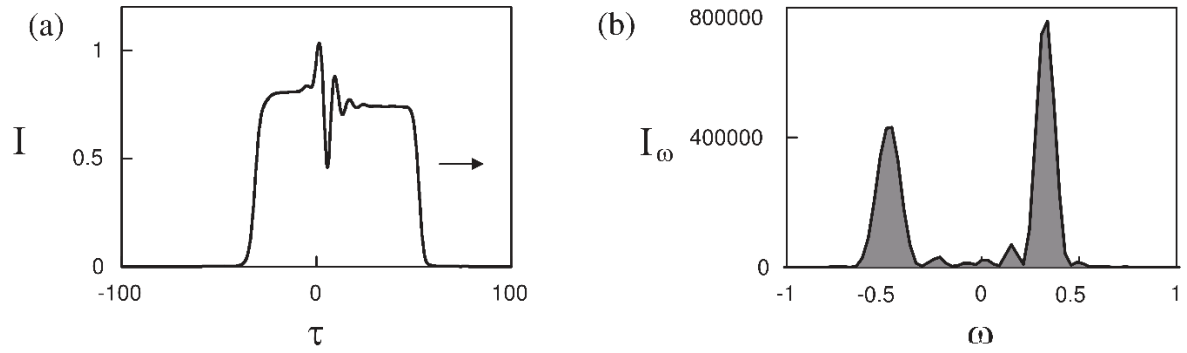

Figure 4:44. (a) Temporal and (b) spectral distributions for a steady-state staircase pulse with spectral doublet structure in the case of a spectral inhomogeneity of an amplification. a=0.5, D_{i3}=-1, h_1=h_2=0.8, b_1=b_2=0.005. Other parameters are the same as in the other figures.

In case of a replacement τ by $-\tau$, a downward staircase pulse is transformed into an upward staircase pulse as shown in Figure 4:45.

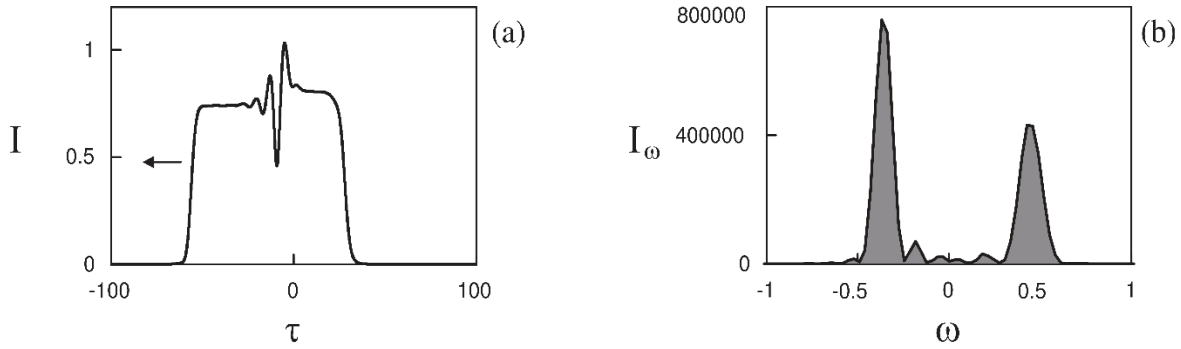

Figure 4:45. a) Temporal and (b) spectral distributions for a steady-state staircase pulse with spectral doublet structure in the case of a spectral inhomogeneity of an amplification: a=0.5, D_{i3}=1, h_1=h_2=0.8, b_1=b_2=0.005. Other parameters are the same as the previous figure.

In the numerical analysis, we have used a distributed model of a fiber laser with cubic and quintic nonlinearities of intracavity medium. To break the symmetry by time reversal, we have modified correspondingly the value of the third order dispersion of the refractive index whereas the second order dispersion remained unchanged. We have found that the generation of stable staircase pulses depends on the spectrally inhomogeneous amplification of the radiation without excluding other mechanisms responsible for such behavior that have not been detailed here. Meanwhile, the experimental results were obtained at the same fixed pump power and with a fine adjustment of the polarization controllers' paddle in every situation, which introduces a variation in the nonlinear losses but not only. We did not observe any dependency between the shape of pulse and the spectral intensity level. In fact, in the

case of a single pulse, downward staircase or upward staircase pulse, the intensity level of the shorter wavelength was always higher than the longer wavelength and the intensity level difference was 1.8 dBm, 6.9 dBm and 3.5 dBm respectively. Therefore, a comparison between the numerical simulations and the experimental results requires more investigation. At the same time, we believe that it would more appropriate to use a more realistic model based on nonlinear polarization rotation technique [111], [162] that would help in a future study.

4.6 Chapter summary

In this chapter, we studied extensively the generation of square pulses operating in the dissipative soliton resonance regime in passively mode-locked fiber lasers. Different methods of mode-locking have been used during the experiment which prove the universality of this emission. We also reported the possibility of controlling the characteristics of the DSR square pulses by means of dual amplification in a figure-of-eight. Later, we demonstrated that even in the DSR regime, there exists instabilities depending on the parameters of the laser cavity which lead to a harmonic distribution of the square pulses. The obtained results are records in energy scaling in a single fiber oscillator, and have been the subjects of different publications.

In the last part of the chapter, we investigated the spectral dynamics of the square pulses in the DSR regime. We have shown there is a possibility of generating square pulses with a spectral-doublet structure where the pulse width increases with the pump power and the spectral spacing between both lobes varies. This extensive study evolved into the first numerical and experimental demonstration of staircase pulses. Concerning the staircase pulses at theoretical scale, it is required to have a mechanism capable of breaking the invariance by time reversal which would allow these pulses to exist, and inhomogeneous gain to stabilize them.

Chapter 5 High output power mode-locked fiber lasers with nanomaterial saturable absorbers

So far, we have considered artificial saturable absorbers, but there is the possibility to use real passive saturable absorbers as a mechanism of mode-locking to build high average output power fiber lasers. In the last decade, nanomaterials have emerged in the field of ultrafast lasers as saturable absorbers thanks to their unique optical properties, such as broadband absorption, short recovery time, and high modulation depth. Even if the usage of such materials is well extent, the actual development of novel methods of creating the saturable absorber device is still very much ongoing, especially in the framework of high average output power lasers.

In this chapter, we discuss the recent advances in mode-locked fiber lasers based on real saturable absorbers: **Graphene** and topological insulators $\mathbf{Bi_2Se_3}$. The optical properties and deposition techniques of these materials will be discussed and their usability in high power laser setups will be demonstrated.

5.1 Introduction

Since the isolation of a single layer of graphene from a layered graphite source in 2004 [163], [164] and the discovery of its unique optical and electronical properties [165], the study of two-dimensional layered materials also known as atomically thin layered materials, has exploded with both popularity and beautiful results. After that success, the scientists around the world extensively investigate other thin layered materials, such as topological insulators TIs, transition metal dichalcogenides TMDCs, black phosphorus BP, and many others. Bulk crystals of these layered materials can be thought of like a ream of paper: composed of many individual sheets which are strongly bound in-plane, though only weakly bound, via van der Waals forces, between sheets. These crystals have interesting properties in their own right, but with

minimal effort, using mechanical exfoliation [165], a single layer may be isolated displaying remarkably different properties than the bulk crystal. Electrons in these materials are absolutely confined in the out of plane direction leading to some very interesting quantum physics arising from their two-dimensional nature. Additionally, since these materials are all surface area they are particularly sensitive to changes in their environment; for instance, as sensors for chemicals absorbed onto their surfaces, or, as will be the focus of this thesis, as sensors for incident light. Finally, they may be easily stacked on top of each other to form vertical hetero-structures [166], [167]. Since different layered materials act as metals, insulators, semiconductors, or superconductors in their monolayer limit [164], different hetero-structures of different materials can run the full spectrum of imaginable device architectures [168], [169]. These materials are also characterized by multiple unique optical properties, such as broadband and almost wavelength-independent absorption or optical bistability (saturable absorption with ultrashort recovery time and high modulation depth). Those properties make 2D materials useful in laser technology, e.g., as saturable absorbers for lasers emitting ultrashort optical pulses. The research on novel 2D materials strongly contributes to the development of novel laser sources, enabling generation of shorter pulses and broader bandwidths at new wavelength regions, previously uncovered by any other coherent light source.

In this thesis, we will focus our investigations on the implementation of Graphene and Bismuth Selenide Bi_2Se_3 as SA in passively mode-locked fiber lasers.

5.2 Fundamentals of nanomaterial based SA

A saturable absorber can be defined as an optical material that has high light absorbance for low intensity light and an eventual saturated absorption causing a low degree of absorbance for high intensity light. The key parameters for a SA are, in general, its frequency or wavelength range, the Modulation Depth (MD), relaxation time, the saturation intensity or saturation fluence, and its dynamic response [170]. These macroscopic parameters can be explained by considering an ideal absorber with only two energy levels separated by an energy gap. Supposing that initially only the lower

level is occupied, a photon impinging on the material excites an electron from the lower to the higher energy state, if the photon energy matches the energy gap between the states. The excited carrier then undergoes a non-instantaneous recombination process; it eventually recombines with a hole in the lowest energy state. By progressively increasing the photon flux, the number of electrons promoted to the higher state per unit time increases consequently, until a condition of strong excitation is reached, which results in the saturation of the absorber, i.e. the initial state is depleted of electrons while the final one is almost completely occupied, and it cannot accommodate new excited carriers. This condition, associated to an increase in transmittance of the material, is a consequence of Pauli principle [68].

Modulation depth of the saturable absorbers can be defined as the difference ΔT between the transmittance of the saturated absorber and its transmittance in ordinary linear behavior, in other terms the maximum change in absorption. It is a wavelength-dependent parameter. Typically, a large modulation depth is required for fiber lasers, where the round-trip gain and loss is high, and dispersion and nonlinearity strongly influence pulse formation.

Saturation intensity is the optical intensity in the steady state required to reduce the absorption to half of its unbleached value. For a low-gain laser amplifier, saturation intensity can be calculated using $I_{sat} = \frac{h\upsilon}{\sigma\tau}$ where $h\upsilon$ is the photon energy at the signal wavelength, σ is the absorption cross-section at the emission wavelength and τ is the upper-state lifetime. In some cases, it's more convenient to use the saturation fluence F_{sat} which is the pulse energy per unit area needed to obtain a change in the transmission equal to $\frac{1}{e}$ of the modulation depth, and expressed by $F_{sat} = \frac{h\upsilon}{\sigma}$.

Relaxation time of a saturable absorber is its intrinsic response time, which can strongly influence the pulse duration, particularly in a bulk laser without dispersion management. Saturable absorbers based on their relaxation time can be divided into fast saturable absorber, with relaxation time of hundreds of femtoseconds or a few

picoseconds and slow saturable absorber, with relaxation time of tens of picoseconds to nanoseconds.

Non-saturable loss refers to the part of the losses, which cannot be saturated. It is an intrinsic material property but can be strongly influenced by fabrication process.

5.2.1 Dynamics of saturable absorption

Following the master equation described by Haus [116], we have:

$$T_R \frac{\partial A(z,t)}{\partial z} = -iD\frac{\partial^2 A}{\partial t^2} + i\delta|A|^2 A + \left[g - \Gamma + \left(\frac{g}{\Omega_g^2} + \frac{1}{\Omega_f^2} \right) \frac{\partial^2}{\partial t^2} - \alpha(z,t) \right] A \qquad \text{Eq. 39}$$

where $A(z,t)$ is the slowly varying field envelope, T_R is the cavity round-trip time, Γ is the intracavity linear losses, D is the intracavity group-delay dispersion, Ω_f and Ω_g the filter bandwidth and gain bandwidth respectively. The SPM-coefficient δ is given by $\delta = \left(\frac{2\pi}{\lambda_0 A_{eff}} \right) n_2 L$, where n_2 is the intensity dependent refractive index of the laser crystal, λ_0 the center wavelength of the pulse, A_{eff} and L are the effective mode area in the laser crystal and length of the light path through the laser within one round-trip, respectively. We assume a gain medium with a long relaxation time and large saturation energy, therefore, the gain g is saturated to its stationary value corresponding to the average power $P_{avg} = \frac{E_p}{T_R}$ and it is defined by $g = \frac{g_0}{1 + \frac{E_p}{P_{sat,medium} T_R}}$ where g_0 is the small signal gain, E_P is the pulse energy defined by $E_p = \int_{-\infty}^{+\infty} |A(t)|^2 dt$ and $P_{sat,medium}$ is the saturation power of the gain medium. $\alpha(t)$ is the response of the saturable absorber or the saturable absorption coefficient.

Thus, the dynamics ruling the saturation of an ideal two-level absorber exposed to a pulsed laser source can be described by the following rate equation [171]:

$$\frac{d\alpha(t)}{dt} = -\frac{\alpha(t)-\alpha_0}{\tau_A} - \frac{\alpha(t)P(t)}{F_{sat}A_{eff}} = -\frac{\alpha(t)-\alpha_0}{\tau_A} - \frac{\alpha(t)P(t)}{E_{sat}} \qquad \text{Eq. 40}$$

where α_0 is the unsaturated absorption coefficient, $\alpha(t)$ is the saturable absorption coefficient that does not include non-saturable losses, τ_A is the recovery time, $P(t)$ is the peak power incident on the SA, F_{sat} is the saturation fluence and A_{eff} is the incident beam area. This equation can be rearranged as:

$$\alpha'(t) + \left(\frac{1}{\tau_A} + \frac{P(t)}{E_{sat,A_{eff}}}\right)\alpha(t) = \frac{\alpha_0}{\tau_A} \qquad \text{Eq. 41}$$

It is possible to distinguish between two types of saturable absorbers: slow and fast SAs.

a) Slow saturable absorber model

When a slow saturable absorber is used, a dynamic gain with the passage of a pulse must be taken into consideration instead of a time-independent gain. The duration of the pulses that hit the absorber is much shorter than the relaxation time of the absorber $\tau_p << \tau_A$, and the response of saturable absorbers to pulses is not considered instantaneous, therefore the term in Eq. 40 related to the recovery time of the absorber is negligible since $P(t) >> E_{sat}$. The generated pulse duration is not purely limited by the relaxation time of saturable absorbers, but by the window of net gain between the saturation of the absorber and the saturation of the gain. The behavior of a slow saturable absorber is described by a time-dependent power loss coefficient, depending on the parameters of the absorber and the incident pulse. The rate equation becomes:

$$\frac{d\alpha(t)}{dt} \approx -\frac{\alpha(t)P(t)}{E_{sat}} \qquad \text{Eq. 42}$$

This approximation yields:

$$\alpha(t)\big|_{slow} \approx \alpha_0 \exp\left[-\frac{1}{E_{sat}}\int_0^t P(t')dt'\right] = \alpha_0 \exp\left[-\frac{E_p}{E_{sat}}\int_0^t f(t')dt'\right] \qquad \text{Eq. 43}$$

where we have substituted $P(t)=E_p f(t)$, implying that if τ_p is the time interval between two light pulses $\int_0^{\tau_p} f(t')dt'=1$ and E_p is the pulse energy. The overall loss that a pulse undergoes in a slow saturable absorber is:

$$\alpha_p(E_p)\Big|_{slow}=\int_0^{\tau_p}\alpha(t')f(t')dt' \approx \alpha_0\frac{E_p}{E_{sat}}\left[1-exp\left(\frac{E_p}{E_{sat}}\right)\right] \quad \text{Eq. 44}$$

Since

$$\frac{F_p}{F_{sat}}=\frac{E_p}{E_{sat}}\times\frac{area}{area}=\frac{E_p}{E_{sat}} \quad \text{Eq. 45}$$

Therefore

$$\alpha_p(F_p)=\alpha_0\frac{F_{sat}}{F_p}\left(1-\exp\left[-\frac{F_p}{F_{sat}}\right]\right) \quad \text{Eq. 46}$$

Thus, it is clearly independent of the pulse shape, and depends only on its amplitude. Therefore, the absorber is assumed to saturate per:

$$\alpha(t)=\frac{\Delta\alpha\left[1-\exp\left(-\frac{F(t)}{F_{sat}}\right)\right]}{\frac{F(t)}{F_{sat}}} \quad \text{Eq. 47}$$

where $\Delta\alpha$ is equivalent to the modulation depth, $F(t)$ and F_{sat} are the instantaneous and saturation fluence, respectively. Following [172]–[174], the analytical solution of the corresponding pulse width in slow saturable absorber based mode-locking models can be derived. In most experimental cases, however, the absorber normally operates at few times its saturation fluence, and the estimated pulse duration is given by:

$$\tau^2=\frac{1.15g_0}{\Delta\alpha\Omega_g^2} \quad \text{Eq. 48}$$

b) Fast saturable absorber model

When a fast-saturable absorber is employed, the gain is assumed to be time-independent and constant during the passage of the pulse since the relaxation time of the rare-earth ions is much greater than the cavity round-trip time. Pulse durations in this situation are mainly dependent on the relaxation time of saturable absorbers. If the pulse duration is much longer than the relaxation time of the absorber $\tau_p >> \tau_A$, then the response of saturable absorbers to pulses are considered instantaneous $\frac{d\alpha(t)}{dt} = 0$ and it is assumed that the absorber can fully recover within the round-trip time of the laser cavity. Therefore, the Eq.40 becomes:

$$0 = -\frac{\alpha(t) - \alpha_0}{\tau_A} - \frac{\alpha(t)P(t)}{E_{sat}} \Rightarrow \alpha(t) = \frac{\alpha_0}{\tau_A\left[\frac{1}{\tau_A} + \frac{P(t)}{E_{sat}}\right]} \qquad \text{Eq. 49}$$

Since $\frac{\tau_A}{E_{sat}} = \frac{1}{P_{sat}}$ and $\frac{P(t)}{P_{sat}} = \frac{I(t)}{I_{sat}} \times \frac{area}{area} = \frac{I(t)}{I_{sat}}$, therefore the saturable absorber response becomes:

$$\alpha(t) = \frac{\alpha_0}{1 + \frac{I(t)}{I_{sat}}} \qquad \text{Eq. 50}$$

where α_0 is identified as the non-saturable loss, $I(t)$ is the instantaneous pulse intensity as a function time and I_{sat} is the saturation intensity of the SA. This theory, describing the absorption through a fast saturable absorber was developed by Haus et al. in 1975 [116].

By assuming the saturation of the absorber device is relatively weak, the corresponding analytical results for the pulse durations of passive mode-locked saturable absorber based lasers can be written as [24]:

$$\tau^2 = \frac{2g_0}{\delta\left|A_0\right|^2 \Omega_g^2} \qquad \text{Eq. 51}$$

where A_0 is the pulse peak amplitude. While analytical solutions of pulse width using either a fast or slow saturable absorber model are shown previously, the achievable pulse durations can be affected by nonlinear effects and dispersion, which play a dominant role in pulse formation in fiber lasers. One of the most common phenomenon observed in fiber lasers is soliton pulse mode-locking, where negative dispersion (group velocity dispersion (GVD)) is involved. In the case of strong soliton pulse shaping, the absorber does not have to be fast since the pulse shaping relies on the combination of GVD and SPM. This leads to a reduction of the pulse width: by a factor of 2-3 shorter than using pure saturable absorber mode-locking [24], and is dramatically larger in a slow saturable absorber than a fast one [175]. For soliton pulse shaping, it should be noted that the absorber is only used to initiate and stabilize the soliton against the continuum.

While the combined effects of GVD and SPM can significantly shorten the durations, instabilities such as pulse breaking are often observed. For soliton pulse shaping, the full width at half maximum (FWHM) pulse width is proportional to the square root of negative dispersion β_2 , the inverse of the pulse energy E_p and the square root of nonlinear coefficient γ :

$$T = \frac{1}{E_p}\sqrt{\frac{|\beta_2|}{\gamma}} \qquad \text{Eq. 52}$$

As the pulse duration decreases, the pulse energy increases, and the absorber will be saturated without providing any further pulse stabilization at a certain power. The pulse energy continues to increase until either continuum breakthrough or the pulse breaks up to reduce the energy of each sub pulse, with each single pulse breaking up into double or multi-pulses. It should be noted that once the absorber is strongly saturated by a high energy single pulse before pulse breaking, it will also be saturated for the multi-pulse solution. Pulse breaking can be overcome by precisely adjusting the intra-cavity power, to lower the peak power and reduce the nonlinear effects.

5.2.2 2D material integration structures as SA

There are several techniques of fabricating saturable absorber devices using 2D materials and make them suitable for use in high power mode-locked fiber lasers. The most popular approaches are illustrated in Figure 5:1. The material might be deposited on a glass plate and inserted into the cavity as a free-space transmission saturable absorber. This approach is most suitable for solid-state lasers [113–115]. For example, in the work of Ugolotti et al., a graphene monolayer grown via chemical vapor deposition (CVD) was transferred from a copper substrate on to a 1 mm thick quartz plate, with the use of poly (methylmethacrylate) (PMMA) polymer. Such SA exhibited 0.75% of modulation depth at 1 μm wavelength and supported mode locking with around 32 μm spot size on the graphene surface. The world's first TI-based fiber laser used a Bi_2Te_3 layer deposited on a quartz plate and inserted into the cavity between two collimators [179].

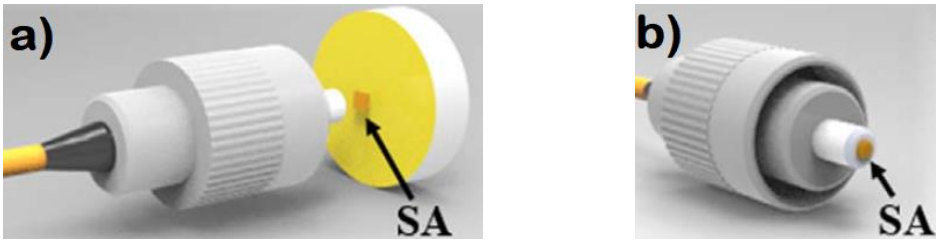

Figure 5:1. Common techniques of depositing SA material on optical substrates: a) glass mirrors, and b) fiber connectors' end.

The SA material might also be deposited on a mirror as in Figure 5:1 (a) and inserted into a linear laser cavity (both fiber based or free space). In the case of a fiber ring-shaped resonator, one can use a circulator to couple the mirror with the cavity. This approach was used, e.g., by Xu et al. [180], [181] for the generation of femtosecond pulses from Er-doped fiber lasers. Graphene-coated mirrors might also serve as saturable absorbers in linear laser cavities as demonstrated by Cunning et al. [182]. However, usually graphene-coated mirrors serve as saturable absorbers for solid-state lasers [183]–[186]. The most impressive results were obtained by Ma et al. [186]. The SA was based on high-quality, CVD-grown monolayer graphene transferred onto a highly

reflecting dielectric mirror. The spot size on the SA was about 60 μm. The laser can generate 30 fs pulses at 50 nm bandwidth centered at 1070 nm.

The probably most popular and common technique of fabricating saturable absorbers with 2D materials is based on fiber connectors as shown in Figure 5:1 (b). This approach was already demonstrated with graphene [35], [36], topological insulators [187], Transition metal dichalcogenide [188], [189], and other recently used materials such as Black Phosphorus [190]. It is a very convenient method since it is alignment free and very robust. It allows to keep the cavity fully fiberized, which is very advantageous—the lasers are more compact, stable, and invulnerable to external disturbances.

The newest technique of SA fabrication is based on the evanescent field interaction effect. For this purpose, tapered fibers (microfibers) or side-polished (D-shaped) fibers might be used as in Figure 5:2. The saturable absorption is based on the interaction between the evanescent field propagating in the cladding of the fiber and the deposited material. Such saturable absorbers were first used in combination with carbon nanotubes [191]. In 2010, Song et al. [192] demonstrated the usage of a graphene-coated D-shaped fiber as a saturable absorber. The laser can generate pulses at 1561 nm with 2 nm of full width at half maximum (FWHM) bandwidth. Afterward, the deposition of TIs and TMDCs on such fibers was demonstrated [193]. The alternative approach, using tapered fibers, is also used and was demonstrated by several authors [34], [194], [195].

Figure 5:2. Saturable absorbers with evanescent field interaction: a) fiber taper (b) and side-polished (D-shaped) fiber.

The performance of fiber lasers with evanescent field interaction is incontrovertible: 70 fs pulses were generated with a Sb_2Te_3 deposited on a tapered fiber [196], whereas it down performed on a D-shaped fiber with the generation of 128 fs pulses [197]. However, a saturable absorber based on a D-shaped fiber, due to its asymmetry,

is always characterized by a polarization-dependent loss (PDL), which mostly depends on the material type (its refractive index), interaction length, and the distance between the polished region and the fiber core. In some reports, the PDL was kept at quite low levels (e.g., 1 dB in [198] with 6 μm distance between the material and the core), but sometimes it exceeds several dB [199]. In this situation, it is difficult to distinguish whether the mode locking originates from nonlinear polarization rotation or from the saturable absorption in the 2D material. In 2015, Bogusławski et al. [200] performed an experiment, which has unambiguously proven that mode locking in such oscillators is a combination of both effects. The study revealed that the hybrid mode-locking mechanism (combined NPR with saturable absorption of Sb_2Te_3 topological insulator) allows to achieve the best performance (in terms of bandwidth and pulse duration), when compared with a truly NPR or a topological insulator saturable absorber TISA mode-locked laser. In the case of taper-based SAs, authors who investigated evanescent field interaction claim higher optical power-induced damage threshold for such SA in comparison to connector end-face deposition due to better thermal management [192].

A variety of mode-locked fiber lasers implementing 2D materials as saturable absorbers has been reported in Table 1. The list is not exhaustive, but it presents the versatility of 2D materials as SA. It groups the materials by type, methods of integration in cavities and resulting average output power at a specific wavelength.

Material	**Deposition method**	**λ (nm]**	**Output power (mW)**	**References**
Graphene	Ferrule	1610	52	[35]
Graphene	Taper	1557.56	4.2	[194]
Graphene	D-shaped fiber	1557	0.5	[201]
Graphene	Mirror	1562	-	[202]
Graphene	D-shaped fiber	1563	11.22	[203]
MoS_2	Ferrule	1556	5.9	[204]
MoS_2	D-shaped fiber	1590	6.91	[205]
MoS_2	Taper	1557-1558	2.51-5.39	[206]
MoS_2	Mirror	1905	150	[207]
WS_2 (Film)	Ferrule	1052	30	[208]
WS_2	D-shaped fiber	1557	110	[209]
WS_2	Mirror	1560	5.28	[210]
WS_2	Taper	1563	2.77	[211]
BP (Film)	Ferrule	1561	5.1	[212]

BP	Taper	1532-1570	5.6	[213]
BP	Fiber ferrule	1910	1.5	[190]
BP	Mirror	1053	820	[214]
Bi_2Se_3	Taper	1559	5.02	[215]
Bi_2Se_3	Taper	1610	308	[34]
Bi_2Se_3	PCF	1563	5.5-75	[216]
Bi_2Te_3 (Film)	Fiber ferrule	1558.5	1.82	[217]
Bi_2Te_3	Taper	1063.4	12.4	[218]
Bi_2Te_3	D-shaped fiber	1547	0.8	[219]
Sb_2Te_3	D-shaped fiber	1047.1	4	[220]
Sb_2Te_3	Fiber ferrule	1558.5	4.5	[221]
Sb_2Te_3	Taper	1542	63	[196]

Table 1. List of mode-locked lasers with 2D materials as saturable absorber. BP: black phosphorus.

5.2.3 Nonlinear measurements of saturable absorber devices

It is possible to see saturation in a saturable absorber by shining a continuous beam of light on it, but the light's intensity is usually not high enough since the saturation intensity of a fast-saturable absorber is often in the order of GW. cm^{-2}. A CW laser provides pulses of infinite duration, which is infinitely long compared to the relaxation time of any saturable absorber. Thus, all saturable absorbers behave like fast saturable absorber when stimulated in this laser regime. To achieve high intensities required to observe saturable absorption in a fast or slow saturable absorber, it is necessary to generate ultrashort pulses.

Experimentally, absorption as function of peak intensity or absorption as a function of pulse fluence is the same. Thus, the three basic nonlinear parameters of a saturable absorber e.g. modulation depth, saturation intensity/fluence, and nonsaturable loss, can be extracted by fitting the experimental data from a two-arm power-dependent transmission setup. In the case of fiber-based saturable absorbers (e.g., 2D material deposited on connectors or tapered fibers/D-shaped fibers), the schematic of an all-fiber power-dependent transmission experiment is depicted in Figure 5:3.

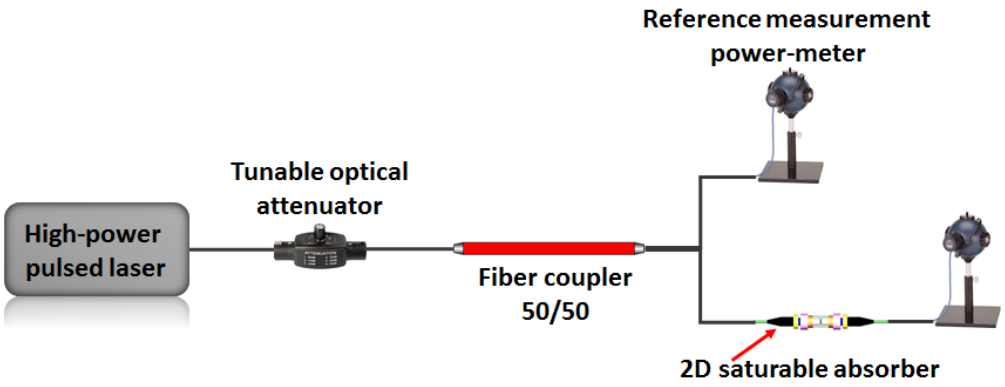

Figure 5:3. Two-arm power-dependent transmission measurement of a saturable absorber.

This method of measurement can be presented as the fiber version of the Z-scan measurement. The light beam from a pulsed laser propagates in the optical fiber through the variable optical attenuator VOA and is split into two parts by using a fiber coupler with defined coupling ratio, e.g., 50%/50%. One portion of the average output power is measured by a power meter for reference, whereas the other portion is injected into the saturable absorber device and measured by a second power meter. The power from the light source is adjusted using the VOA to change the light intensity on the SA, which allows us to plot the transmission through the sample as a function of the incident light average power. Taking into consideration the intensity independent losses, the absorption coefficient in a fast-saturable absorber is expressed as:

$$\alpha = \alpha_{ns} + \frac{\alpha_s}{1 + \frac{I}{I_{sat}}} \qquad \text{Eq. 53}$$

where α_{ns} is the non-saturable absorption coefficient, α_s is the saturable absorption coefficient, I is the incident optical intensity and I_{sat} is the saturation intensity. When $I \ll I_{sat}$, the absorption becomes $\alpha = \alpha_{ns} + \alpha_s$ and if $I \gg I_{sat}$, the absorption will be as a function of the nonsaturable absorption only. The absorption coefficient is normalized to the material thickness L to eliminate the influence of different sample thickness.

With the relation between transmission and absorption, the transmission can be expressed as:

$$T = 1 - \alpha_{ns} + \frac{\alpha_s}{1 + \frac{I}{I_{sat}}} \qquad \text{Eq. 54}$$

The model in Eq.54 is used to fit the measured data to retrieve the different parameters related to the saturable absorber. Sometimes, this model does not work well because the incident intensity I needs to be increased to saturate the SA [222]. Therefore, different ad-hoc models originating from an approximation of Eq. 53 are available in the literature as referenced in Table 2.

Transmission equations	**Reference**
$T = 1 - \frac{\alpha_s}{1 + I/I_{sat}} - \alpha_{ns}$	[223], [224]
$T = 1 - \alpha_s \exp\left[-\frac{I}{I_{sat}}\right] - \alpha_{ns}$	[224]– [226]
$T = 1 - \exp\left[\frac{-\alpha_s}{1 + I/I_{sat}}\right] - \alpha_{ns}$	[222]
$T = \frac{\alpha_s}{\sqrt{(F/F_{sat}) + (F/F_{sat})^2}} .\text{atanh}\left(\sqrt{\frac{F}{F + F_{sat}}}\right) + (1 - \alpha_{ns})$	[228], [229]
$T = 1 - \frac{\alpha_s}{\sqrt{1 + 3I/I_{sat}}} - \alpha_{ns}$	[230]
$T = \exp\left[1 - (\alpha_s + \alpha_{ns})\right]$	[231]

Table 2. Transmission fitting equations for fast saturable absorbers.

5.3 Microfiber taper based graphene saturable absorber (MF-GSA)

Graphene is a two-dimensional crystal of carbon atoms arranged in a honey-comb lattice. It is considered as most revolutionary material of the 21st century, thanks to its unique opto-electronic properties and the wide variety of applications it can be used in. Besides the application in pulsed lasers, graphene was successfully used in many optoelectronic devices, such as photodetectors, modulators, polarizers, sensors, and solar cells [232]–[236]. The lack of the band gap in pristine graphene [237] might

generally be unwanted in some electronic applications, but makes it extremely useful in photonics. Thanks to this unique property, graphene is characterized by a constant absorption coefficient in a wide spectral range. In consequence, it might act as a saturable absorber in lasers operating at different wavelengths. The historically first mode-locked lasers with graphene were developed in 2009 [82], [83]. Shortly after those reports, a number of papers appeared, demonstrating novel concepts of ultrafast lasers utilizing various forms of graphene and its derivatives [238]–[243], [180], [36], [194], [244], [245], [57], [35], [245]–[249], [201]. However, since the first demonstration of mode-locking mechanism using graphene as saturable absorber (GSA), passively mode-locked fiber lasers based on GSA reported low average output power in the order of tens of milliwatts to barely a hundred of milliwatts. A limiting factor leading to low average output power, is the low saturation power of the graphene if it is deposited on the fiber ferrule since the effective area of interaction is limited to the area of the fundamental mode [35]. To circumvent this problem, different methods of graphene deposition have been investigated earlier in this chapter. Graphene can be deposited on side polished D-shaped fiber [201], [203], [250], on collimator [251], in photonic crystal fiber (PCF) [249] and on optical tapers [194], [252]. Obviously, collimator based SA will alter the all-fiber structure of the fiber laser inducing difficulties in the alignment; the side-polished fiber based SA is not easy to fabricate and has smaller interaction area between the light and graphene, whereas the PCF SA requires a complex procedure and a considerable amount of time to fabricate. Optical tapers can improve the laser induced damage threshold and saturation power of graphene while offering an effective absorption effect. In an optical taper, when the light propagating in the fiber reaches the waist of the taper where the diameter is reduced gradually, the fundamental mode is transformed adiabatically into a compressed mode with an evanescent field that extents outside the fiber clad. Since the graphene nanoplatelets are deposited on the surface of the taper, the graphene particles absorb a part of the evanescent field and a saturable absorber is created [253].

5.3.1 Behind the fabrication of the optical taper

A fiber taper consists of a core embedded in a finite cladding, which is surrounded by air. Its diameter at the waist is comparable to the wavelength of the light. At the entrance of a fiber taper, the fundamental mode, linearly polarized (LP) mode, LP_{01} is the only propagation mode in the fiber and propagates as the core mode, which is defined to be the state when its effective refractive index n_{eff} lies between the cladding index n_{cl} and the core index n_{co}. When the core diameter is reduced during tapering, n_{eff} of the core mode decreases continually. The guided core mode exists in the infinite-cladding geometry with an effective index n_{eff}, which satisfies $n_{cl} < n_{eff} < n_{co}$. The thickness of the cladding can be assumed to be infinite and the cladding-air interface is negligible. Each cladding mode with an effective index n_{eff} that satisfies $n_{air} < n_{eff} < n_{cl}$ is guided by the core infinite cladding air waveguide. n_{air} is the refractive index of surrounding air. In the tapered region, since the core is reduced, the evanescent field extends further outside the core and into the air.

In this section, the taper was designed and manufactured by P. Mouchel at Keopsys as the main part of his PhD work. By using different sets of parameters, P. Mouchel has developed an optimized and efficient technique to design low loss optical tapers easily implemented with a good versatility in fiber cavities. The fabricated taper's waist is 5.7 mm long with a diameter of about 20.5 µm as presented in Figure 5:4.

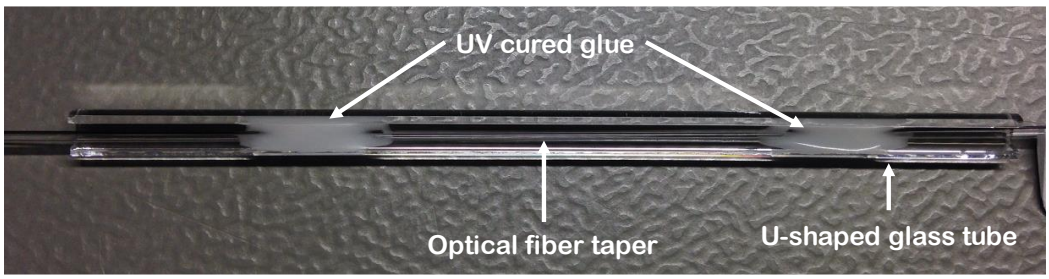

Figure 5:4. Manufactured packaging of the optical fiber taper.

In this model, the transitions are hybrid: the diameter changes linearly with the position from 125 µm to 70 µm then exponentially to the waist diameter. The evolution of

the taper's diameter as well as the hybrid evolution represented by the fitted curve are shown in Figure 5:5.

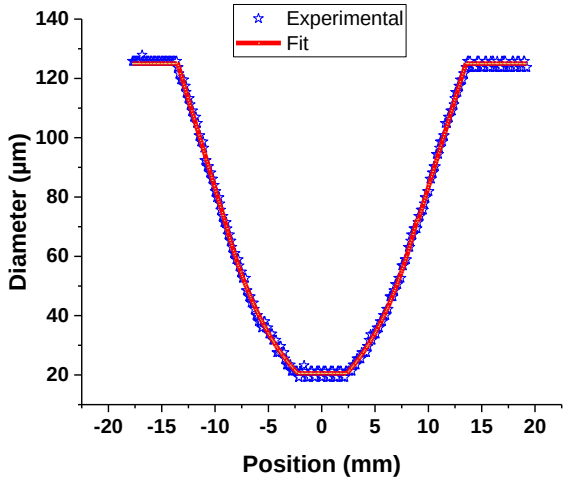

Figure 5:5. Diameter evolution as a function of the probe position.

It is important to note that the curve is symmetrical. Hence, it allows a high transmittance for which the insertion losses are estimated to be around 0.36 dB. While other transition shapes are possible [254], [255], minimal insertion losses were obtained with the hybrid transitions.

Since tapers allow the propagation of modes other than the fundamental mode at 1550 nm when their waist diameter is less than 30 µm [256], this results in a phenomenon of interference between the propagating modes [257]. Therefore, the transmission of the taper depends on the wavelength injected in the taper and it can be seen in Figure 5:6.

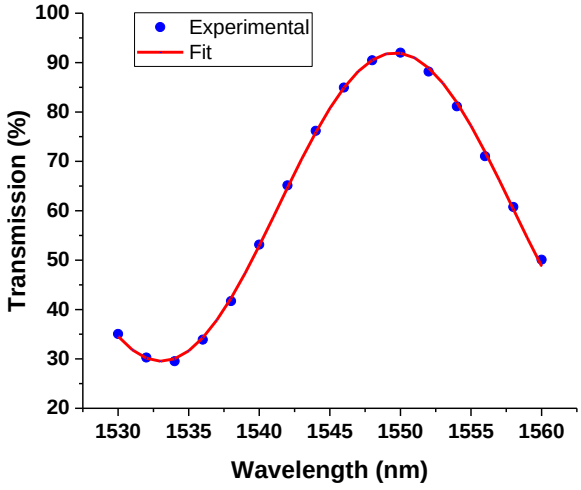

Figure 5:6. Measured transmission of the optical taper as a function of wavelength.

The experimental data is fitted using a typical equation of a two-mode interference:

$$T(\lambda) = T_1 + T_2 + 2\sqrt{T_1 \cdot T_2} \cdot \cos(2\pi \frac{\lambda}{P} + \varphi) \qquad \text{Eq. 55}$$

where T_1 and T_2 are the transmissions of both modes, λ is the wavelength of the injected signal, P is the period and φ is a phase shift.

The optical deposition of graphene onto the taper has been elaborated with a vast collaboration of P. Mouchel at the laboratory. To prepare the MF-GSA, we used a commercial multilayer graphene nanoplatelets dispersion (GNP) in water with a concentration of 1 mg. mL^{-1} from Sigma-Aldrich (799092-50ML) instead of the pristine graphene monolayer dispersion in alcohol from Graphene Supermarket (PGF-1-50). The droplets of GNP were injected via a micro syringe on the center of the tube so that the waist of the taper is completely immersed into the aqueous solution as shown in Figure 5:7.

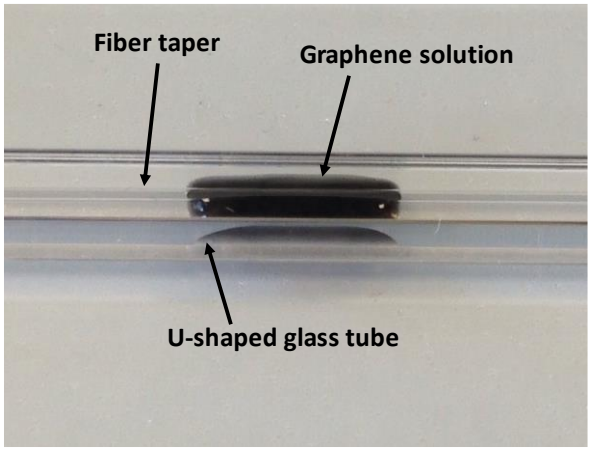

Figure 5:7. Graphene solution in the tube before the optical deposition.

After that, a continuous wave laser with output power of 95 mW centered at 1550 nm was injected into the taper and the transmission was monitored during the deposition time. As water from the solution evaporated, the strain applied on the taper changed its spectral response which led to a fluctuation in the transmitted power. After 20 minutes, the optical deposition of graphene onto the taper by the optical tweezers effect [194] started which triggered a significant loss of the transmission average power.

After a total of 27 minutes, the solution completely disappeared from the tube where only graphene was left on the taper as it is presented in Figure 5:8.

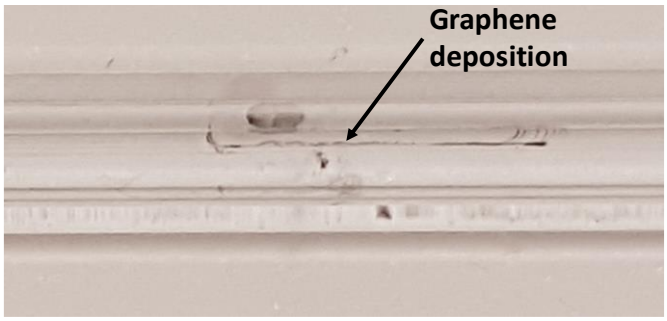

Figure 5:8. Deposited graphene on the waist of the taper.

5.3.2 Graphene saturable absorption characterization

The process of saturable absorption in a graphene was extensively studied by researchers in the recent years [258]–[260]. The process is schematically explained in Figure 5:9.

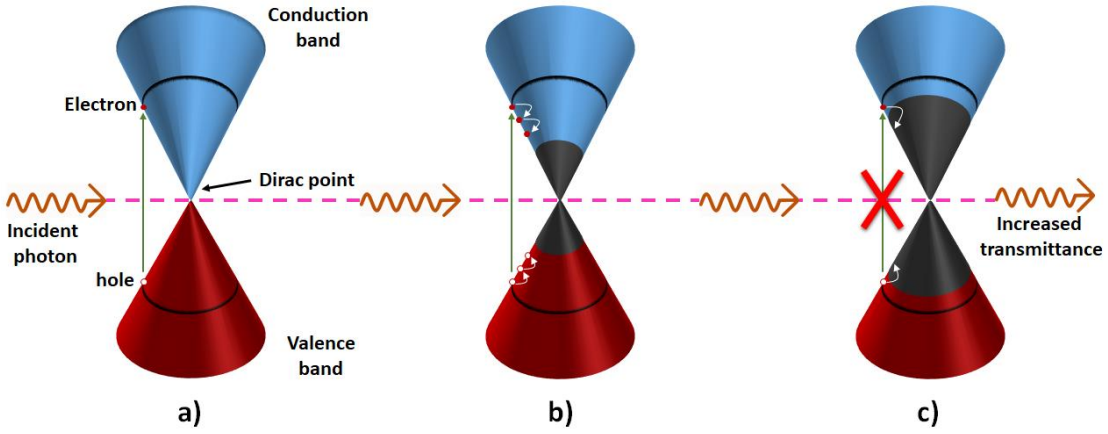

Figure 5:9. Saturable absorption in graphene under optical excitation. a) Light absorption and excitation of carriers, (b) carrier relaxation to a Fermi–Dirac distribution due to scattering, (c) Pauli blocking.

A single graphene layer absorbs approximately a 2.3% fraction of the incident light [261]. The illumination causes excitation of the electrons from the valence band to the conduction band. After a very short relaxation time, these electrons cool down to a Fermi–Dirac distribution. If high intensity light continues to interact with graphene, the energy states in both bands will be filled, which blocks the absorption. This

is the Pauli blocking and we have a saturable absorption at this level [238], [260]. Graphene is known to have a fast 70 – 150 fs relaxation time, followed by a slower relaxation process in the order of 0.5 – 2.0 ps, which was confirmed by pump-probe measurements [258], [259]. The absorption coefficient of graphene remains constant over a broad bandwidth, ranging from the visible to the mid-infrared [262]. The nonlinear optical properties of the fabricated graphene based SA are measured in an all-fiber power-dependent transmission setup as in Figure 5:3 [248]. The radiation source used is a homemade pulsed laser centered at 1563 nm with 5 ps pulse width and a repetition rate of 2 MHz, capable of delivering up to 450 mW of mean output power. A 3-dB fiber coupler is spliced to the output of the laser, where one of the output fibers stands as a reference and the other is spliced to the taper. The mean power transmitted by both ends is monitored by two integrating spheres (Thorlabs S145C and S146C). The measured saturable absorption curves of the multilayer graphene nanocoated optical taper with the modulation depth and the theoretical fitting are plotted in Figure 5:10.

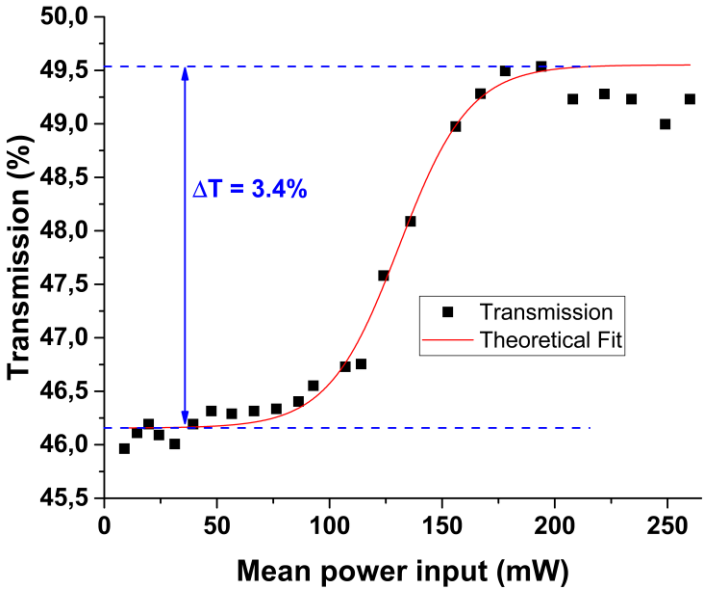

Figure 5:10. Measured power-dependent transmission of the multilayer graphene nanocoated optical taper.

Since graphene is considered as a fast saturable absorber, its nonlinear transmission is described by different, more complex formula [228], [229]:

$$T = \frac{\alpha_s}{\sqrt{\left(P/P_{sat}\right)+\left(P/P_{sat}\right)^2}}.\text{atanh}\left(\sqrt{\frac{P}{P+P_{sat}}}\right)+(1-\alpha_{ns}) \qquad \text{Eq. 56}$$

where ΔT is the modulation depth, α_{ns} the non-saturable absorption and P_{sat} the saturation power. For an input power, less than 50 mW, the transmission of the taper is around 46.2 %. When the input power is increased, the transmission reaches around 49.6 % and fluctuates in a range of 0.4 % of the transmitted power when the input mean power is greater than 180 mW. This leads to a saturation power around 131 mW, a 50.4 % non-saturable absorption and a modulation depth of 3.4 %.

5.3.3 High average output power mode-locked laser with MF-GSA

The proposed fiber setup is a typical standard unidirectional ring cavity that we have used in different parts of this manuscript. The schematic presented in Figure 5:11 consists of the MF-GSA spliced with an inline polarization insensitive isolator (PI-ISO), a polarization controller (PC) and a 70% output coupler. The cavity length is about 120 m, including 112 m standard single mode fiber (SMF) with GVD of −22 $ps^2.km^{-1}$. The total cavity dispersion is about −2.632 ps^2. The performance of the laser is monitored using the available instruments that have been described along the manuscript.

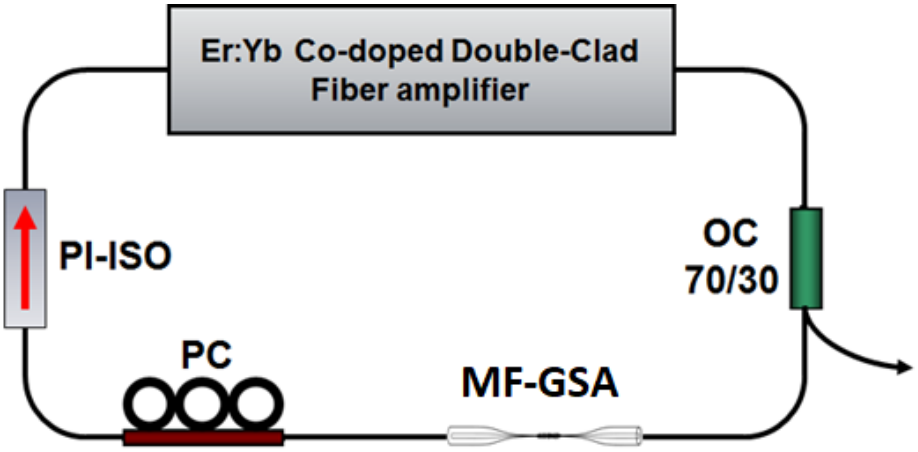

Figure 5:11. Experimental setup. OC: output coupler, PC: polarization controller, MGF-GSA: microfiber taper graphene saturable absorber, PI-ISO: polarization-insensitive isolator.

a. Multipulse soliton distribution

By carefully adjusting the polarization controllers, mode locking appears when the pump power is increased to 863 mW. Once the mode locking state is achieved, the laser starts operating in multiple soliton regime as demonstrated in Figure 5:12 which shows the temporal trace of the output intensity over one round-trip with the pump power of about 900 mW. The temporal trace repeats from one round-trip to the other meaning that the solitons are at rest relative to each other.

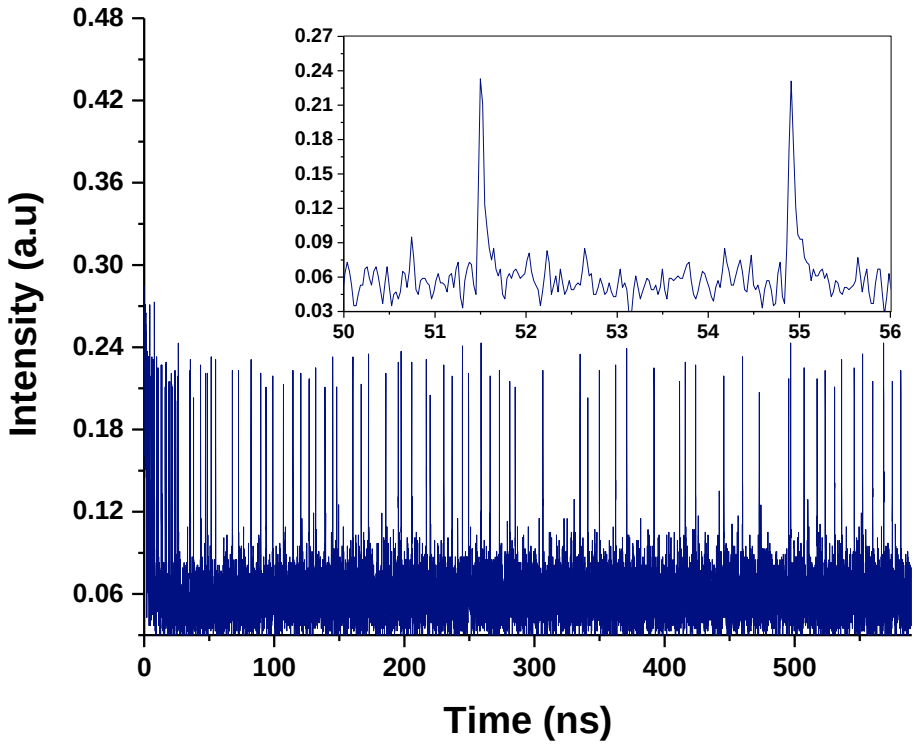

Figure 5:12. Temporal profile of the multiple soliton regime at 900 mW of pump power.

The corresponding spectral profile is plotted in Figure 5:13. The spectrum is visualized with a resolution of 0.05 nm, VBW 200 Hz, 1000 sampling points without averaging. It is centered on 1559 nm with a 3-dB bandwidth of 0.85 nm.

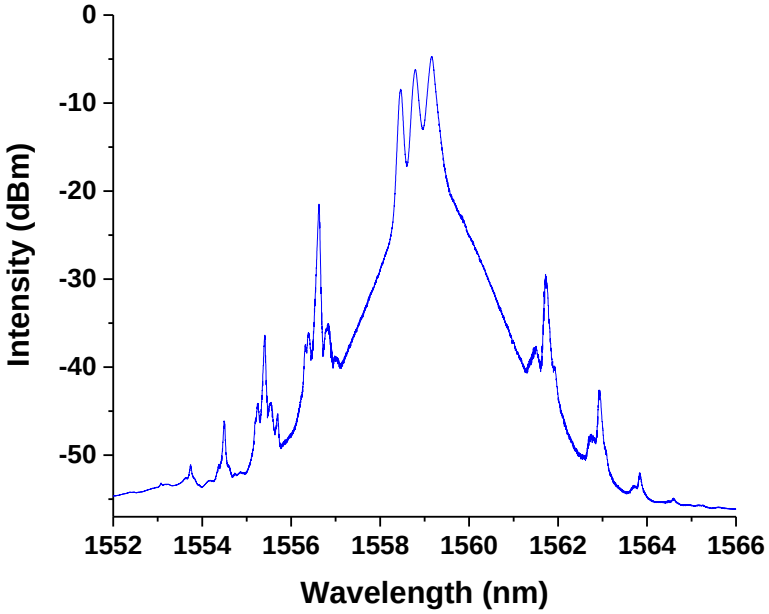

Figure 5:13. Spectral profile of the multiple soliton at 900 mW of pump power.

The symmetric Kelly sidebands on the spectrum indicate that the laser operates in the soliton regime. The peaks on the top of the spectrum reveals the existence of some continuous wave component. Such component plays an important role on the management of the interactions between neighboring solitons [41]. The autocorrelation is shown in Figure 5:14.

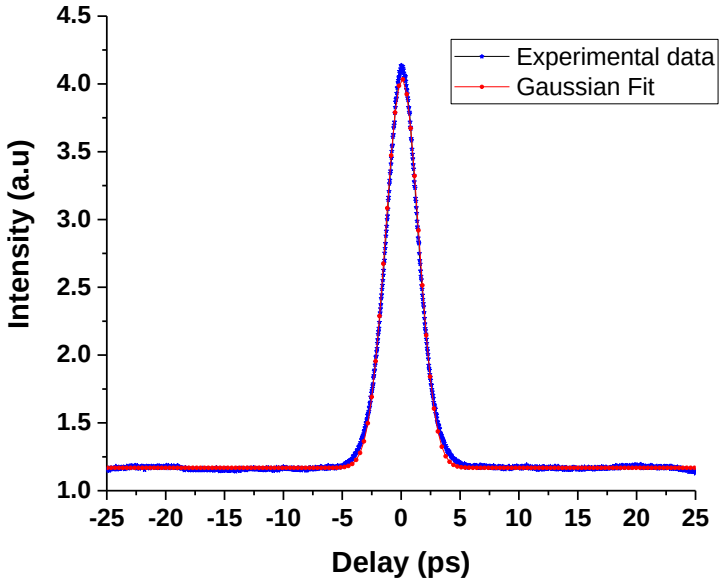

Figure 5:14. Autocorrelation of the corresponding multiple soliton regime.

The pulse duration is 4.3 ps after deconvolution with a time-bandwidth product of ~0.45. The small deviation from the 0.44 transform limit for a typical Gaussian soliton

shape indicates that the pulses are almost transform-limited. The absence of any pedestal in the autocorrelation trace confirms that solitons are not in relative motion [114]. The fundamental repetition rate of the cavity is 1.67 MHz and the signal to noise ratio is 22 dB as shown in Figure 5:15.

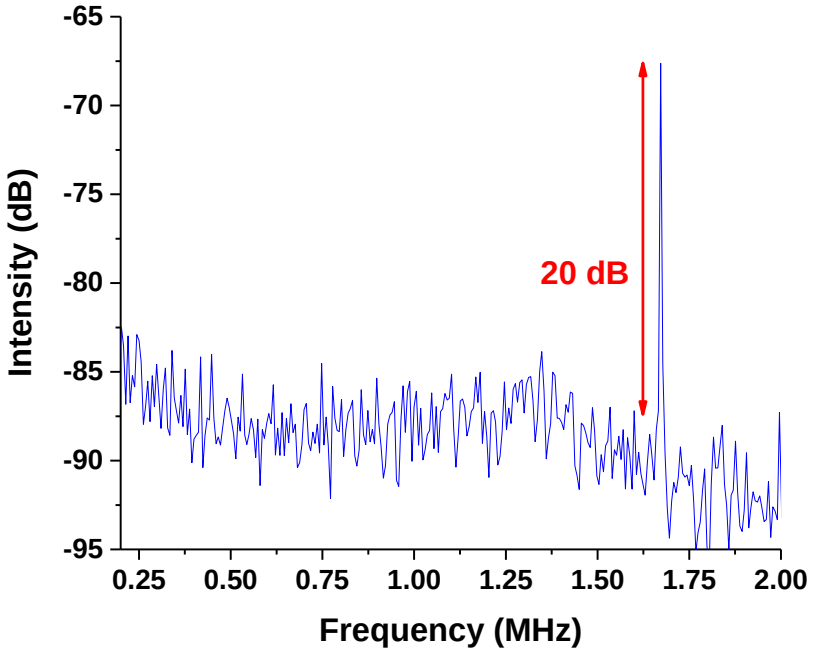

Figure 5:15. RF spectrum of the multiple soliton regime.

At this stage and for any pumping power above mode-locking threshold, a careful adjustment of the polarization controller allows to modify the soliton distribution.

b. Harmonic soliton bunch distribution

We have systematically modified the position of the polarization controller's paddles to obtain a harmonic distribution of soliton bunches in which isolated pulses are grouped into small packets regularly spaced along the cavity. Each packet, usually called a soliton bunch, contains many isolated solitons in relative motion. An example of harmonic mode-locking of soliton bunches is given in Figure 5:16 for a pump power of 1.2 W.

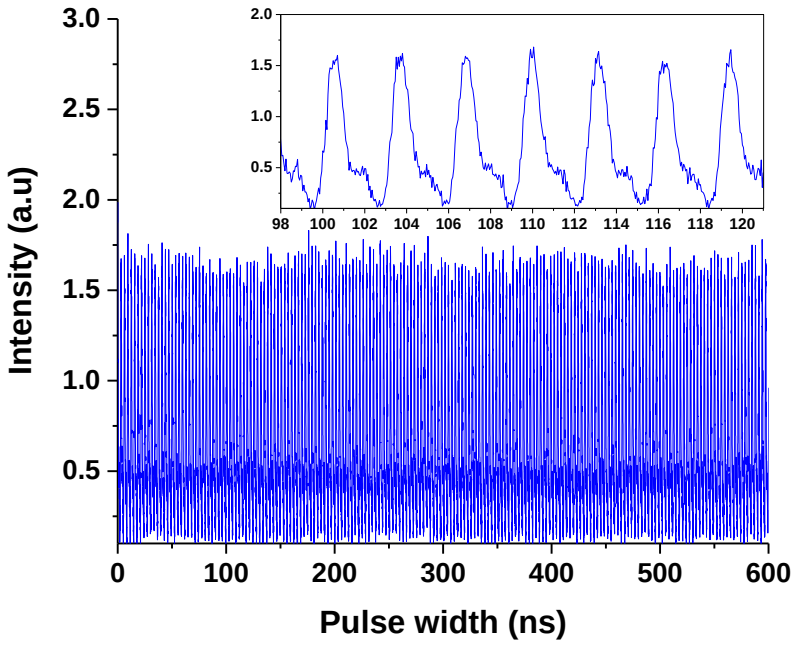

Figure 5:16. Temporal profile of the emitted harmonic soliton bunches.

The temporal distribution in Figure 5:16 shows a regular series of bunches of about 2 ns width. The observed spectrum shown in Figure 5:17 has the same resolution in Figure 5:13. It is centered on 1559 nm with a 3-dB bandwidth of 0.7 nm. We also notice the disappearance of the continuous wave components on the top of the spectrum.

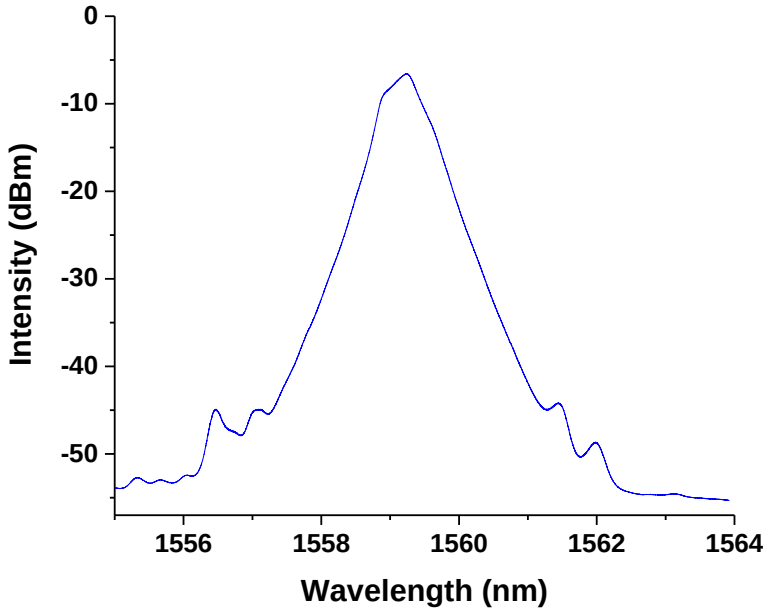

Figure 5:17. Spectral profile of harmonic soliton bunches.

The large pedestal in the autocorrelation trace in Figure 5:18 reveals that the solitons are in relative motion. The measured pulse width is 7 ps after deconvolution.

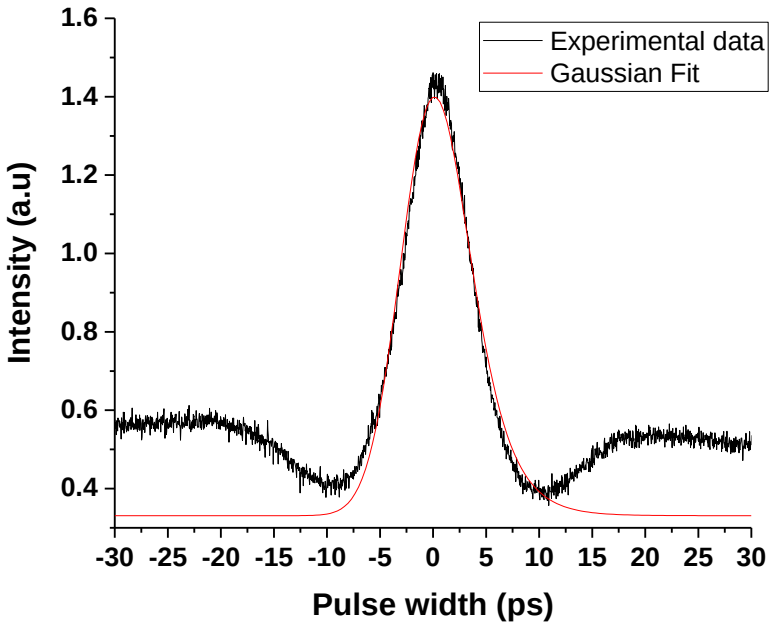

Figure 5:18. Autocorrelation of harmonic soliton bunches.

The RF spectrum in Figure 5:19 shows a repetition rate of about 366 MHz corresponding to the 219th harmonic order. The signal to noise ratio measured with 1 MHz resolution bandwidth (RBW) is around 22 dB. The measured average output power is 156 mW.

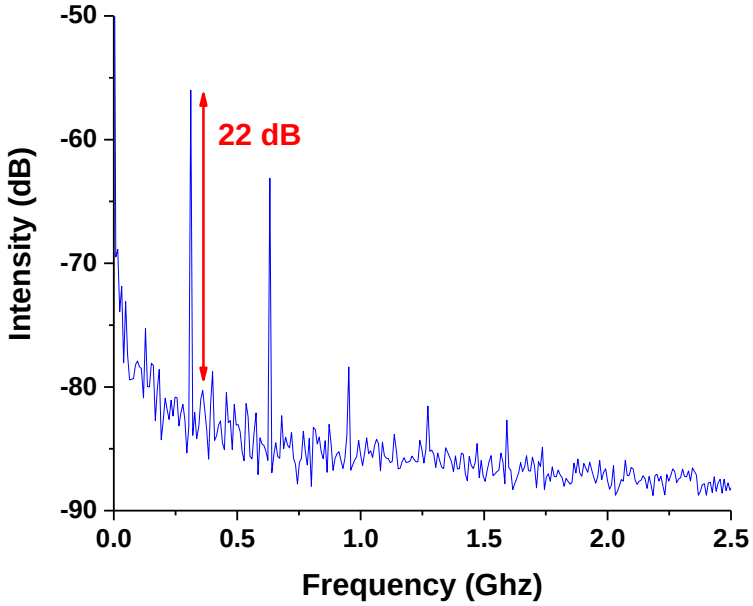

Figure 5:19. RF spectrum of harmonic soliton bunches.

By finely modifying the polarization controllers and increasing the pump power, high order harmonic mode-locking of equally spaced soliton bunches can be

obtained. It is worth mentioning that at different pump powers of the harmonic mode-locked regime, the spectral and pulse widths of the solitons remain nearly invariant. At a maximum pump power of 3 W, the 326th harmonic order of soliton bunches is obtained with an average output power of 520 mW as it can be observed in Figure 5:20.

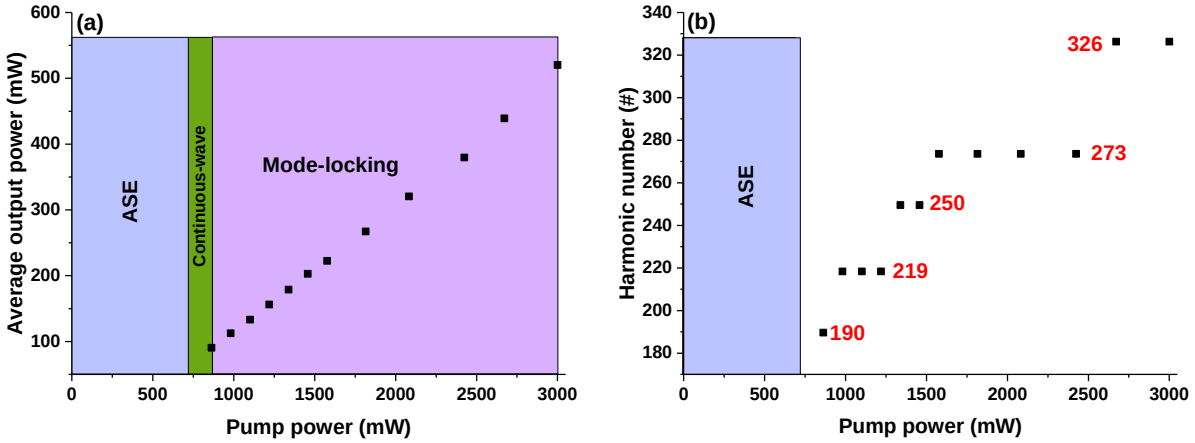

Figure 5:20. (a) Evolution of the output power as a function of the pump power. (b) Evolution of the harmonic order as a function of the pump power.

In Figure 5:20 (a) and Figure 5:20 (b), we report the evolution of the output power and the harmonic order as a function of the pump power, respectively. While the pump power increases to 3 W, the average output power reaches 520 mW. We have carefully verified that if the graphene nanocoated optical taper is removed from the cavity no mode-locking effect occurs while adjusting the polarization controller.

5.4 Microfiber taper topological insulator saturable absorber (MF-TISA)

TI is a new class of Dirac materials with a small band gap in its bulk state and a gapless metallic state in its edge/surface confirmed by the investigation of carrier recombination mechanism using time resolved angle resolved photoelectron spectroscopy [263]–[265]. The surface state has a Dirac electronic spectrum like graphene, but the directions of spin and momentum are locked together [266]–[270]. Among all the identified topological insulators, three have attracted much attention as it can be seen

in the extensive number of publications in the last decade: bismuth telluride (Bi_2Te_3), bismuth selenide (Bi_2Se_3) and antimony telluride (Sb_2Te_3).

5.4.1 Brief background of the TIs

The excitation process that explains the process of light absorption in topological insulators is shown in Figure 5:21. Any photon with energy larger than the insulating bandgap value can excite electrons in the valence band towards the corresponding conduction band at the bulk state [271]. It also means that under weak light intensity, by absorbing any photon with energy larger than the insulating bandgap value, electrons in the valence band can be excited to the conduction band, which accounts for the broadband linear absorption mechanism of the topological insulator. However, under more intensive light with single photon energy larger than this value, due to the Pauli blocking principle, the generated carriers filling the valence bands prevent further excitation of electrons at valence band, leading to the saturable absorption.

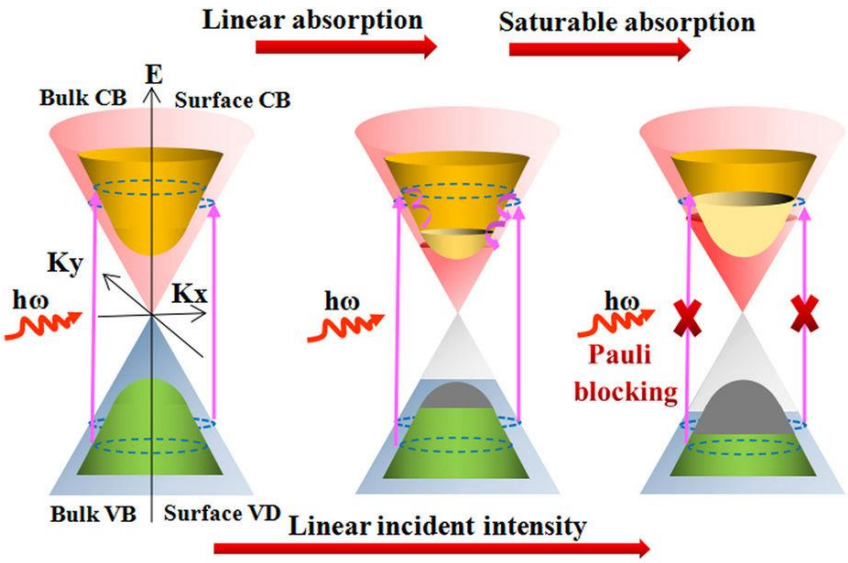

Figure 5:21. Schematic of optical saturable absorption in topological insulator Bi_2Se_3 [272].

Zhao et al. proposed for the first time an experimental demonstration of a mode-locked fiber laser incorporating a TISA by dropping Bi_2Te_3 nanosheets onto a quartz plate [179]. The fiber oscillator generated short pulses in the C-band at 1558 nm with a pulse width around 1.21 ps. Extensive investigation of the nonlinear properties of Bi_2Te_3 performed by the same group showed that this material has a modulation

depth of 61.2% and a third-order nonlinear refractive index as high as 10^{-14} $m^2.W^{-1}$ [273]. In the same family of TI, Bi_2Se_3 presents a linear dispersion Dirac-like electronic-band structure like graphene. Due to Pauli blocking, when it is excited by strong light with single-photon energy larger than the bandgap (0.2~0.3 eV), saturation absorption occurs [270]. Zhao et al. have reported that the absolute modulation depth of Bi_2Se_3 can be as high as 98% [274]; the SA wavelength range is calculated to be from ultraviolet to 4.1 μm [224], [270]. Zhao et al. also reported the first demonstration of a Bi_2Se_3 based mode-locked fiber laser [274]. Among the most prominent and important research results on TI we can highlight the first demonstration of harmonic mode locking with Bi_2Te_3 [215], first demonstration of the usage of Sb_2Te_3 topological insulator for mode locking [187], harmonic mode locking with Sb_2Te_3 [221], or development of TI-polymer composites. The shortest pulse achieved directly from an oscillator mode-locked only by a TI-based SA is 128 fs and was reported in 2014 by Sotor et al. [197]. Liu et al. demonstrated the generation of pulses as short as 70 fs at 1542 nm wavelength with a spectral bandwidth at 3-dB of 63 nm by using a hybrid cavity [196]. The oscillator has a repetition rate of 95.4 MHz with Sb_2Te_3 TI deposited on a tapered fiber. However, the mode locking was not truly SA based since the cavity contained an additional polarizer and wave-plates. Thus, the mode locking was a result of a hybrid combination of saturable absorption and NPR.

All the previous results were focused on the generation of ultrashort pulses using the TI, but few or none investigated the average output power as shown in Table 1. Therefore, we investigate in this section, the possibility of achieving high average output power short pulses using Bi_2Se_3.

5.4.2 Production and characterization of TISA

Our colleague Z.C Luo and his team from South China Normal University conceived and fabricated the TISA. We are very grateful because they managed to send us a prototype to use in high power laser cavities. In this section, we will present the TISA as it has been originally developed.

Bismuth Selenide Bi_2Se_3 (99.999%, Alfa Aesar) has been used to make the solution as it is exhibited in Figure 5:22.

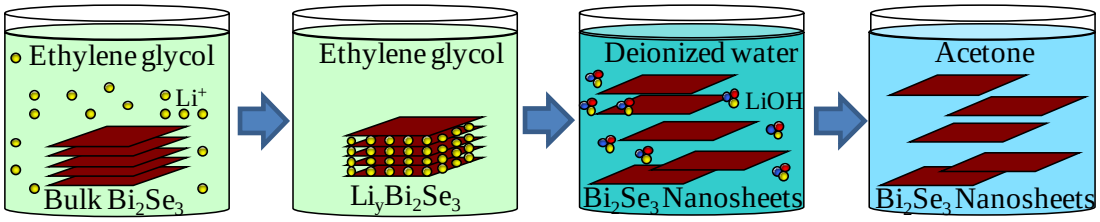

Figure 5:22. Schematic representation of the formation of Bi_2Se_3 nanosheets.

The Bi_2Se_3 nanosheets were synthesized by cost-effective hydrothermal intercalation and exfoliation method [275]. After preparing the Bi_2Se_3 nanosheets, they were dispersed in an acetone solution with 0.1 $mg.ml^{-1}$ concentration, and ultrasonicated for 30 minutes. The tapered fiber which has a waist diameter of about 11 µm was made using a dedicated machine (Optic Fiber Conic Clink). The schematic for the fabrication of fiber taper is shown in Figure 5:23.

Figure 5:23. Microfiber optical taper schematic.

After having the nanomaterial and the fiber taper prepared, the TI acetone solution is dropped onto the taper which has been previously fixed onto a piece of glass. By injecting a laser light into the SMF, a strong evanescent field is formed at the waist of the taper and spreading outside the microfiber, which will trigger the optical deposition process because of the principle of optical tweezers [276]. The length and thickness of the deposited TI can be roughly adjusted by controlling both the size of liquid drop and the deposition time. After the optical deposition, the fabricated TISA is evaporated at room temperature and the tapered fiber based TISA is finished as it can be seen in Figure 5:24 a). Figure 5:24 b) shows microscopy image of fabricated microfiber-based TISA.

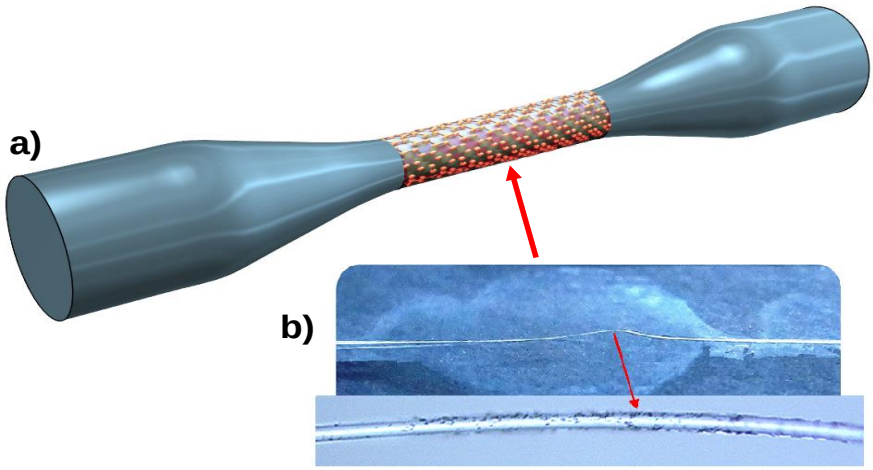

Figure 5:24. a) Microfiber optical taper with deposited TI, forming a TISA. b) microscopic image of TISA.

When we received the TISA from China, we used a 1.61 µm home-made mode-locked pulsed source [277] to characterize its nonlinear optical properties. We measured the transmission of the TISA with different average powers as shown in Figure 5:25 where the data and the corresponding fitting curve have been plotted.

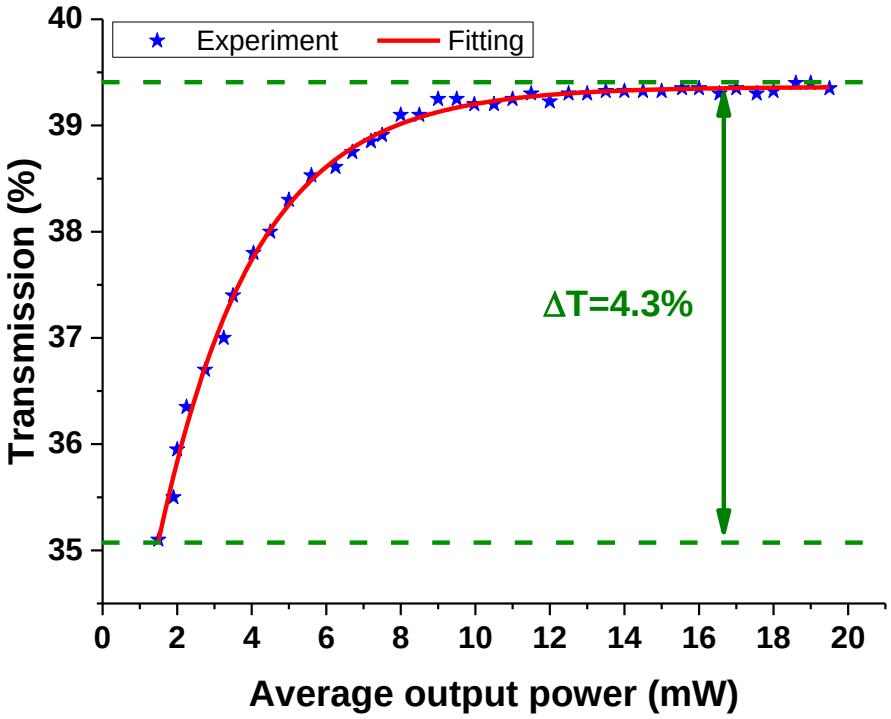

Figure 5:25. Nonlinear transmission measurement of Bi_2Se_3 on a microfiber taper

By using the fitting equation for fast saturable absorber $T = 1 - \alpha_s \exp\left[-\frac{I}{I_{sat}}\right] - \alpha_{ns}$ appearing in Table 2, we extracted the nonlinear parameters. The modulation depth is ~4.3% and the non-saturable loss is ~60.7%, whereas the saturation power intensity is around 5 mW.

5.4.3 Variability of ultrashort pulse generation regimes

The experimental schematic of the fiber laser setup incorporating the TISA is shown in Figure 5:26. It consists of a unidirectional ring where the TISA and a polarization controller (PC) are spliced and the latter is used to adjust the state of polarization in the cavity. A 20% output coupler is used to extract the power from the cavity. It is a good compromise allowing to maximize the output power as well as to get L-band mode-locked operation [33], [278], [279]. The cavity length is about 29.2 m, including 21.2 m standard single mode fiber (SMF) with GVD of −22 $ps^2.km^{-1}$. The net cavity dispersion is about −0.586 ps^2.

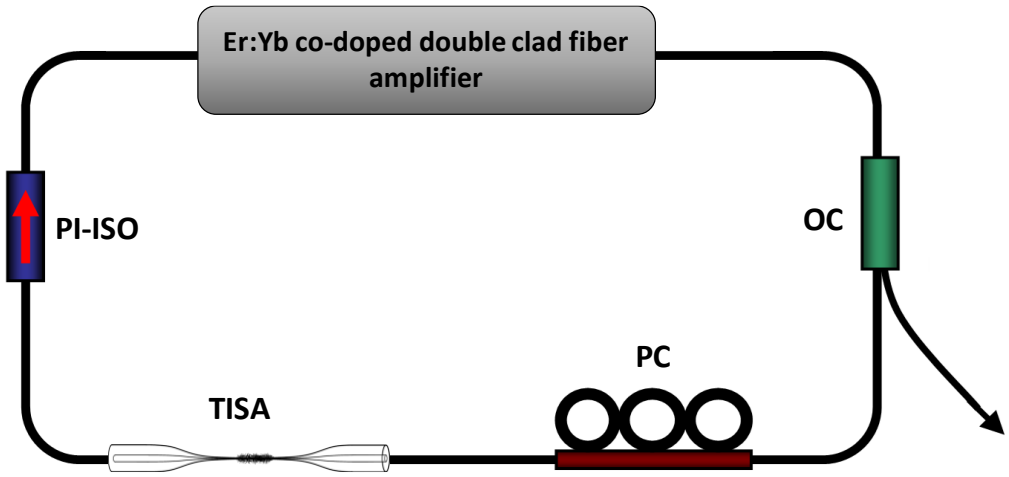

Figure 5:26. Experimental setup of the fiber cavity. OC: output coupler, PC: polarization controller, TISA: topological insulators saturable absorber, PI-ISO: polarization-independent isolator.

Er:Yb co-doped double clad fiber lasers have shown their ability to emit multiple ultra-short pulses in both normal and anomalous dispersion regimes. Hundreds or even thousands of pulses can indeed coexist in the cavity regardless the mechanism of mode-locking. The coexistence of pulses produces complex and varied dynamics

within the cavity. The pulses may be either organized or disorganized in a part of the cavity or distributed throughout the cavity or grouped in a packet or several packets.

a. Multipulse soliton distribution

By exploiting the topological insulator nonlinear characteristics, mode-locking appears when the pump power reaches ~1.2 W. Once the mode locking state is achieved, the laser operates in multiple-soliton regime with dynamical patterns depending on the exact cavity parameters [114]. The fundamental repetition rate of the cavity is 7.04 MHz. Figure 5:27 shows the temporal trace of multiple-solitons with the pump power of ~2 W.

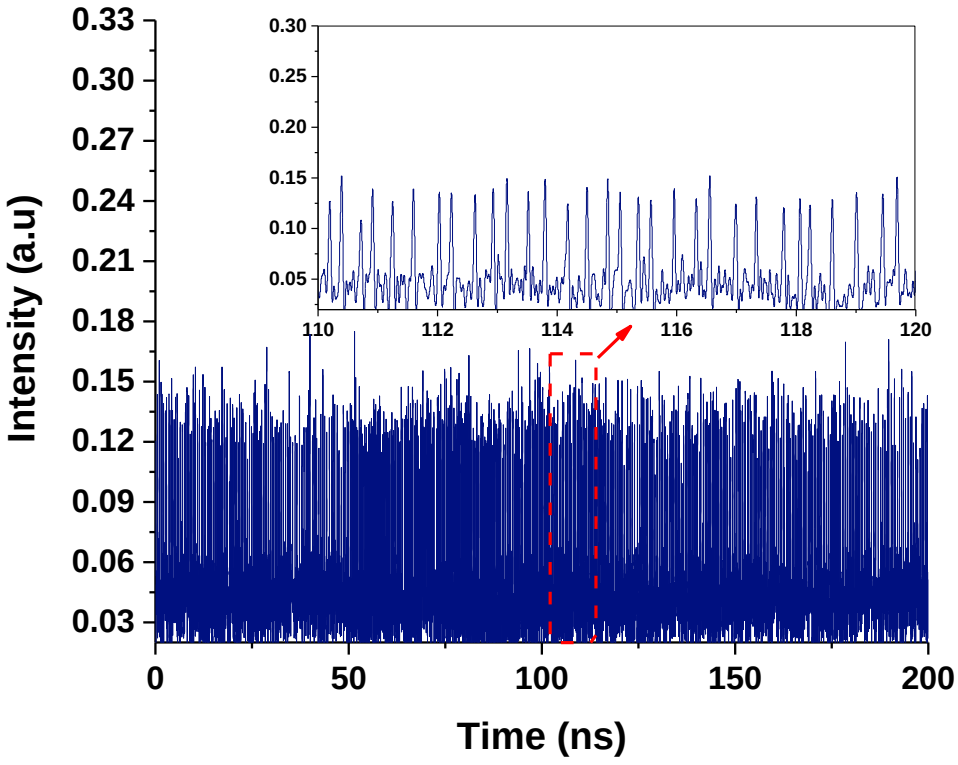

Figure 5:27. Optical spectrum of the multiple soliton regime at 2 W.

The laser emits pulses in the L-band. The corresponding spectrum is shown in Figure 5:28. It exhibits a central wavelength at 1610 nm with a 3-dB bandwidth of 0.91 nm.

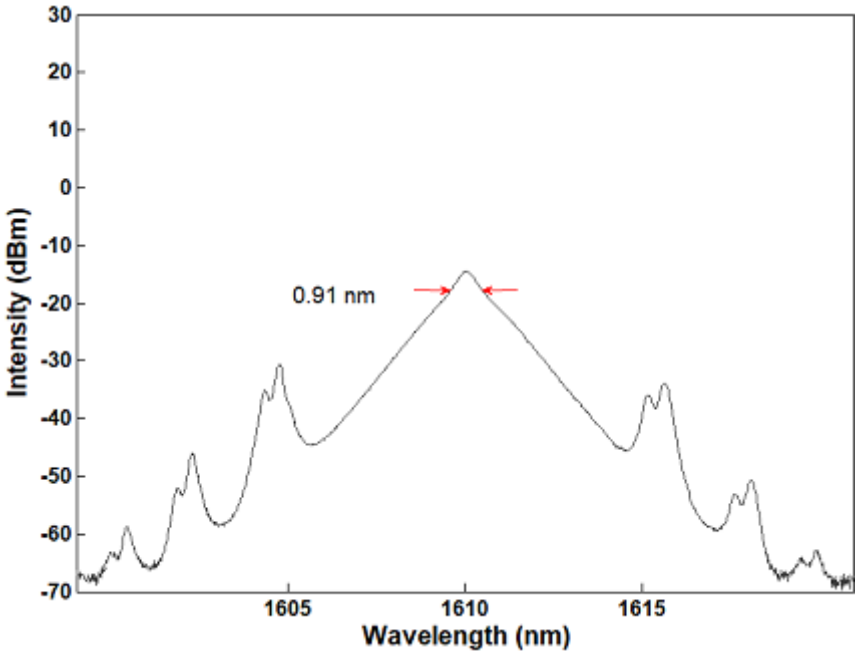

Figure 5:28. Corresponding spectrum of the generated pulse regime

Such long wavelength emission is the consequence of the low-loss cavity. The symmetric Kelly sidebands on the spectrum indicate that the laser operates in the soliton regime. The autocorrelation of the optical pulses is measured at the output of the oscillator and the estimated pulse duration is 3.1 ps as it is shown in the autocorrelation trace in Figure 5:29.

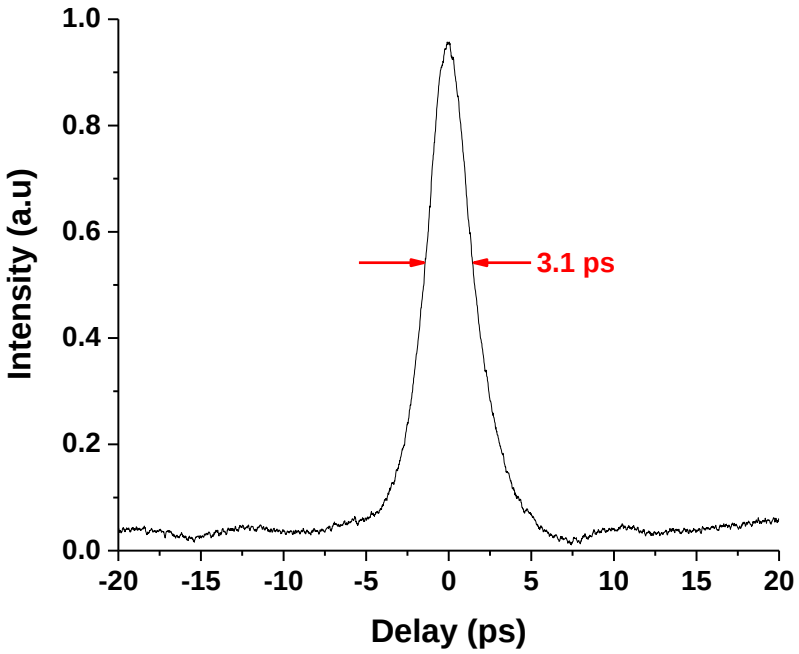

Figure 5:29. Autocorrelation trace.

The time-bandwidth product of the pulses is ~0.32, the small deviation from the 0.315 transform limit for a typical hyperbolic-secant soliton shape indicates that the pulses are almost transform-limited. By varying the pump power while keeping the polarization controller at a fixed position, we noticed that the spectral width and pulse width of the solitons did not change significantly.

b. Soliton bunch distribution

As the pump power increases in the cavity, the number of solitons in the cavity grows. By finely adjusting the polarization controller, the solitons in the cavity tend to form a soliton bunch, in which many soliton pulses group themselves in a tight packet whose duration is much larger than the individual pulse width. The temporal profile of the generated optical bunch of solitons is highlighted in Figure 5:30. It exhibits high intensity bunches of solitons with few nanoseconds width.

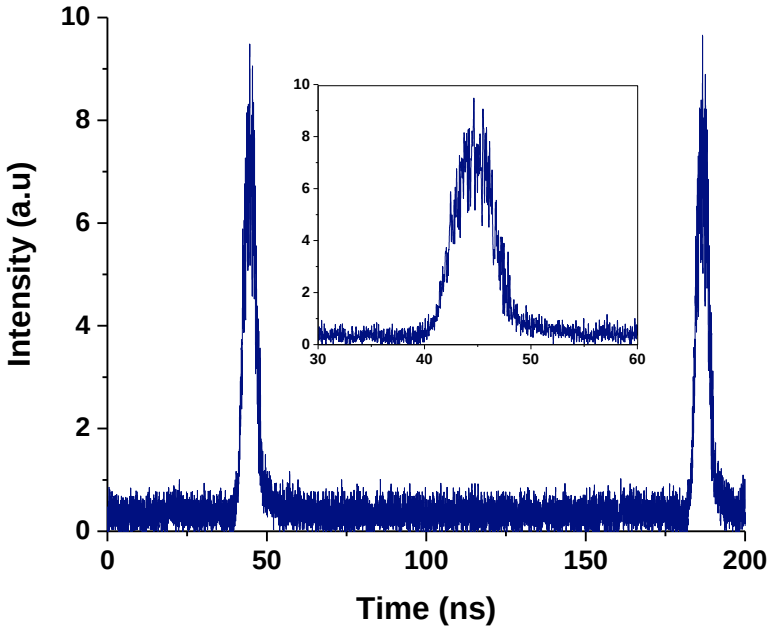

Figure 5:30. Temporal profile of a selected soliton bunch inside the cavity.

The corresponding spectrum and autocorrelation trace are presented in Figure 5:31. The spectral profile does not show any modulation demonstrating that the states between solitons are not bonded. The spectrum is centered at 1610 nm with a 3-dB bandwidth of 1.06 nm. The soliton pulses in the bunch have width of ~2.76 ps. The

large pedestal in the autocorrelation indicates that solitons are in relative motion inside the soliton bunch.

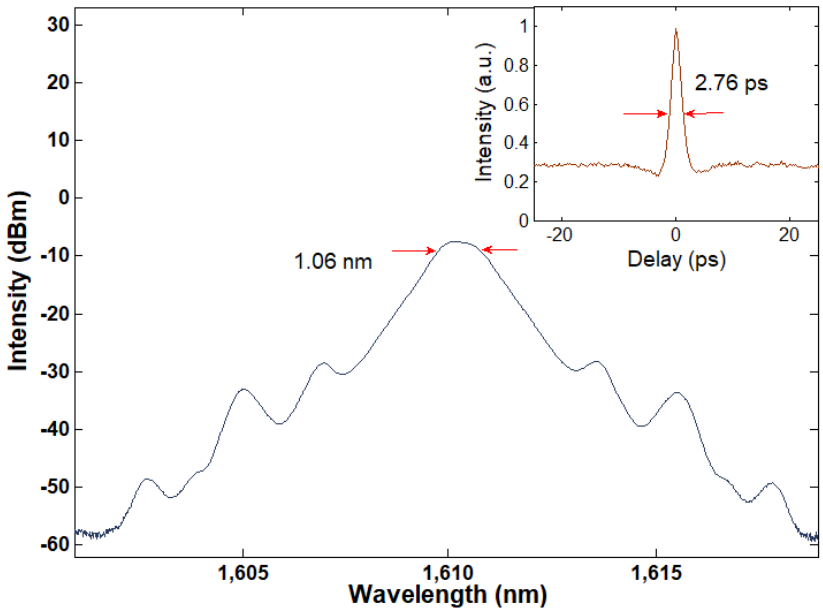

Figure 5:31. Optical spectrum and inset autocorrelation trace of the soliton bunch.

c. Harmonic distribution of soliton bunches

When the pump power is between 1.2 and 3.7 W, the states of multiple-soliton and soliton bunches can be changed to each other by a simple adjustment of the PC. However, when the pump power exceeds 3.7 W, only soliton bunch operation can be observed. At this stage, if we change the position of the polarization controller paddles, the soliton bunch can be split into many small soliton bunches distributed along the cavity with equal spacing. At a maximum pump power of 5 W delivered by the fiber amplifier, we obtain the 91st harmonic mode-locking of soliton bunches. Figure 5:32 shows the temporal trace of the soliton bunches with a bunch width of ~0.7 ns.

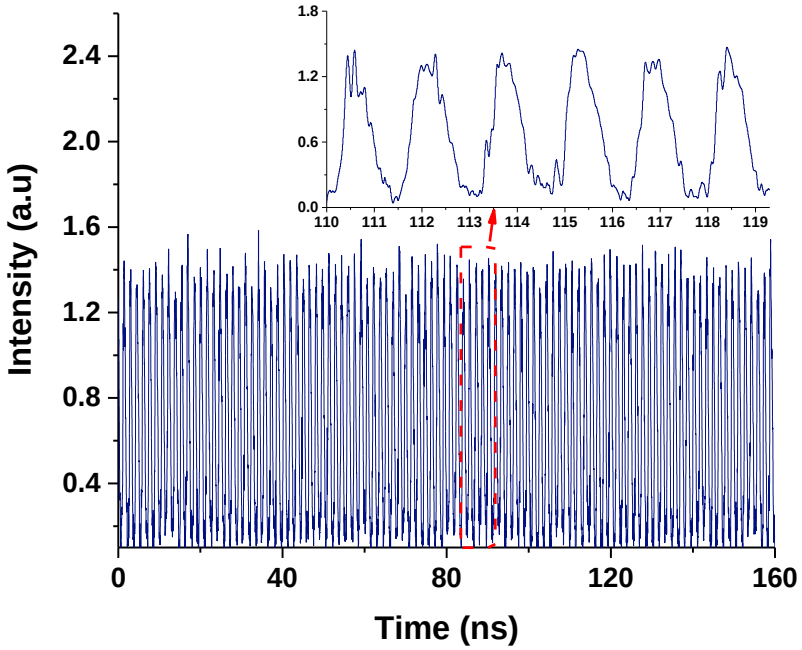

Figure 5:32. Temporal profile of harmonic soliton bunches (inset zoom on soliton bunch).

The spectral profile and the autocorrelation are reported in Figure 5:33. The spectrum is centered at 1611 nm, where the bandwidth at 3-dB is approximatively 1 nm. The spectral modulation see in the figure, is not big enough to demonstrate any binding between the existing solitons. These various partially phase-locked solitons are in every bunch as it is suggested by the optical spectrum.

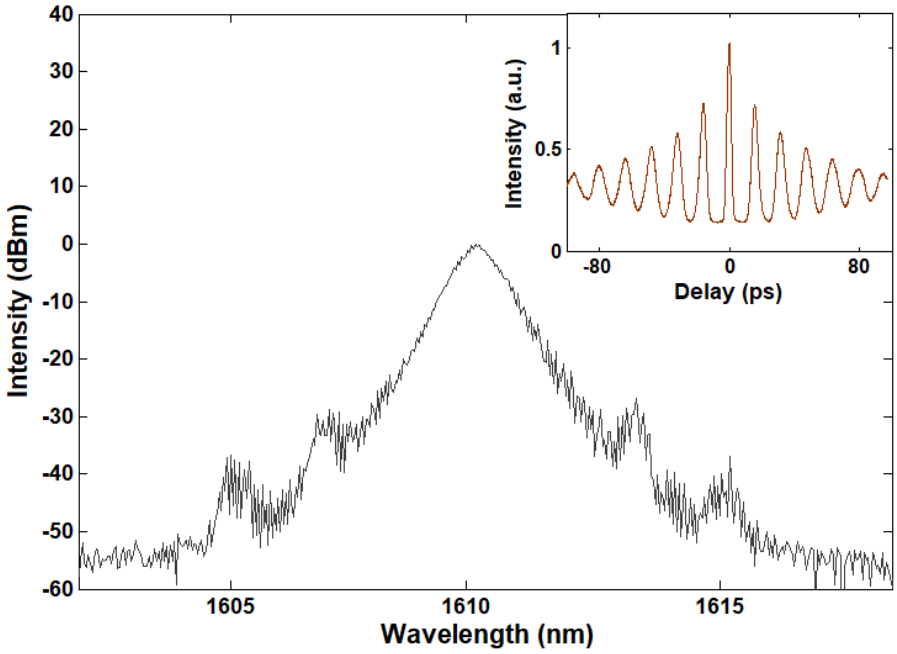

Figure 5:33. Spectral profile of harmonic soliton bunches. (inset is the corresponding autocorrelation trace).

The corresponding autocorrelation in the inset, shows multiple coherent peaks which is an indicator that the pulses are relatively close to each other. The measured soliton width inside the bunch is 3.2 ps. Figure 5:34 shows the corresponding radio frequency (RF) spectrum.

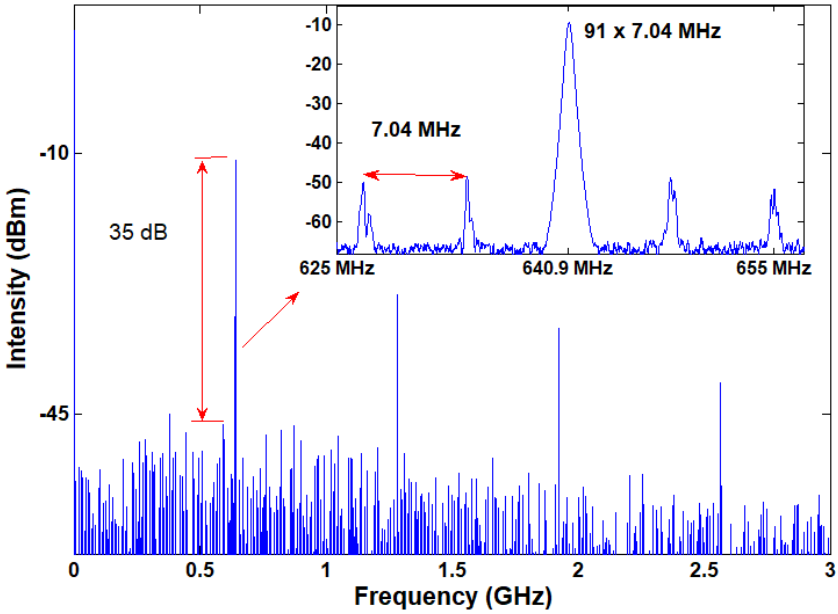

Figure 5:34. RF spectrum of the corresponding harmonic soliton bunch.

The repetition frequency of the 91st harmonic mode locking is 640.9 MHz, the super-mode suppression ratio is 35 dB.

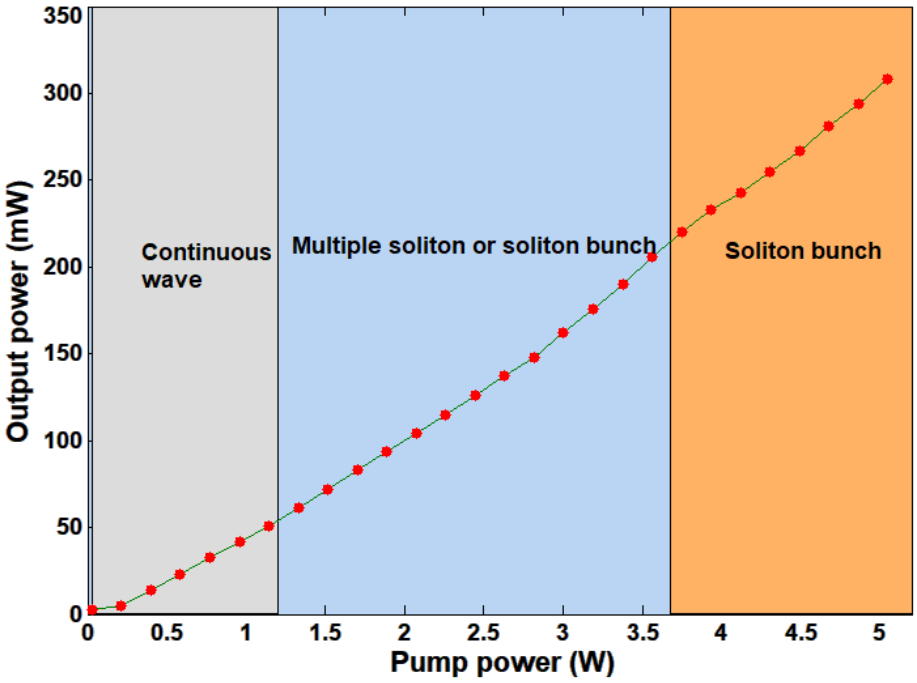

Figure 5:35. Evolution of the output power and soliton distribution as a function of the pump power.

The output power increases almost linearly with the pump power as shown in Figure 5:35. Meanwhile, we notice that the threshold of mode-locking is at around 1.2 W of pump power, while the threshold of only soliton bunch operation is above 3.7 W. At a maximum pump power of 5 W, the average output power reaches 308 mW which is a record in fiber oscillator incorporating Bi_2Se_3 as SA. For higher pumping powers, the absorption of the TISA saturates, and the laser becomes continuous.

5.5 Chapter summary

Since the first successful isolation of single-layer graphene in 2004, we have witnessed tremendous progress in the implementation of nanomaterials based saturable absorbers in fiber lasers setups. In this chapter, we report that **Graphene** and **Bismuth Selenide** saturable absorbers can be implemented in fiber lasers for the generation of high average output power ultrashort pulses at 1559 nm and 1610 nm respectively. Both nanomaterials were deposited on optical tapers because of the long light-matter interaction that improves the laser's induced damage threshold and the nanomaterials' saturation power while offering an effective absorption effect and high average output power.

By using a deposited graphene on fiber taper as saturable absorber device, the generation of the 326^{th} harmonic bunch of solitons with an average output power of 520 mW and 22 dB of signal to noise ratio has been demonstrated in a fiber ring setup. The isolated pulses inside the bunch had 7 ps pulse width. The long cavity length plays an important role in increasing the nonlinearity. Therefore, the low modulation depth of the saturable absorber and the accumulation of nonlinear phase-shift during the cavity round-trip causes the generation of multiple pulses. On the other hand, long cavity length could have potential to generate energetic pulses with low repetition rate if the single pulse operation can be maintained.

At the same time, ultrashort pulses were emitted by using a Bi_2Se_3 saturable absorber device instead of the graphene. Therefore, we report the generation of different regimes of ultrashort pulses up to the 91^{st} harmonic mode-locking of soliton bunches with an average output power of 308 mW.

These are the highest average output power recorded in an all-fiber laser incorporating graphene or Bi_2Se_3 coated optical taper as saturable absorber.

Chapter 6 Conclusion and outlook

The overriding purpose of this thesis is to investigate the spectro-temporal dynamics of solitons in co-doped Er:Yb fiber lasers to generate high average output power and high energy pulses. To carry out the goal, it is necessary to reach some prerequisites. Finding the nature of interactions between propagating pulses in a fiber cavity and how they relate to the emission of specific optical distributions, assumed a high degree of importance during the literature review conducted for this thesis. Related to that effort, it was important to reach an understanding about the importance of cavity design and optimization. In this course, we report a variety of experiments directed toward the study of harmonic mode-locked laser stability by external injection, the generation of high energy pulses in the dissipative soliton resonance regime and the emission of high average output power pulses in fiber lasers. This covers a large spectrum of different results: optical pulses from picosecond to nanosecond, low and very high pulse energy, low and high repetition rate cavities, artificial saturable absorbers and nanomaterial based saturable absorbers. To conclude this work, we wish to return to some important results that we have put forward, in the external injection influence on laser distribution, the high energy pulses generation and high output power nanomaterial saturable absorber fiber laser, and to draw on these some research perspectives and recommendations.

By reproducing the context in which Niang et al. [48], [49] have demonstrated the influence of optical injection on a mode-locked fiber laser, we have investigated another aspect of the external injection influence on an established harmonic mode-locked distribution. The results presented in Chapter 3 demonstrate a significant improvement of the output pulse SNR when the external CW signal respects certain constraints. In fact, when it is tuned in the spectral bandwidth of the oscillator, it can increase the SNR if its amplitude is less than the internal CW component. Under these circumstances, we obtain a passively mode-locked fiber laser using the NPR mechanism with output pulses of 1.4 ps width and a repetition rate of 1.76 GHz demonstrating an improvement of the pulse stability up to +14 dB.

Traditionally, and still currently, solid state systems have been used to provide high energy and peak power laser systems to the industry. However, compared to these solid states systems, fiber lasers can provide better pulse quality since the tight confinement of the beam within the core provides better output modal quality with excellent heat dissipation and higher repetition rates. To produce low cost, compact mode-locked fiber laser systems that can provide pulse energies compatible with application requirements and comparable to solid state counterparts, we have investigated in Chapter 4, the dissipative soliton resonance operational mode and built two laser setups using different mode-locking mechanism NPR and NALM, from which we successfully generated very high pulse energies with tunable pulse width. In the NPR setup configuration, square-wave pulses SWP were obtained at a 373 kHz repetition rate frequency, providing 2.27 μJ energy and a tunable width in a range of 190 ns. In the NALM configuration, we demonstrated that by adjusting the amplifiers' gain in the loops, we can control the pulse characteristics accordingly. As a result of various cavity optimizations [148], we obtained a SWP emission at 133 kHz repetition rate frequency with 10 μJ energy and a width up to 416 ns. Meanwhile, we studied the multi-pulsing instabilities in the ring configuration. By reducing the length of the cavity to a very few hundreds of meters, we were in a zone of parameters in which both solitons and square-wave pulses can co-exist. We noticed that by controlling the linear and nonlinear losses in the cavity, the obtained SWP at the fundamental frequency can be split into several SWP with equal width and spacing having a DSR profile. Consequently, we reported the generation of the 13^{th} harmonic order of DSR SWP at 672 kHz repetition rate frequency.

Meanwhile, Komarov et al. [156] demonstrated the possibility of generating the same type of square pulses with a spectral doublet structure. By increasing the pump power in the fiber laser cavity, the pulses manifest the features of the DSR while the spectral lobes' 3 dB bandwidth and positions remain unchanged. In this context, we investigated the spectral dynamics of the square pulses in the DSR regime. We have shown there is a possibility of generating square pulses with a spectral-doublet structure where the pulse width increases with the pump power and the spectral spacing

between both lobes varies. The experimental results were in complete agreement with the numerical results in [156]. This extensive study evolved into the first numerical and experimental demonstration of staircase pulses, where a two-intensity level pulse is emitting while having a spectral profile comparable to square pulses with spectral doublets.

All the pulses obtained in Chapter 4 operate in dissipative soliton resonance regime using artificial saturable absorbers such as NPR or NALM. Besides these saturable absorbers, real nanomaterial based saturable absorbers have proven in the last decades their ability when implemented in laser cavities to obtain ultrashort pulses. The world of photonics, among others, is particularly keen in exploiting the peculiar absorption characteristic of 2D or 3D materials for various applications, from photo-detectors and Terahertz devices to transparent conductors and plasmonic devices. In Chapter 5, we demonstrated the possibility of emitting high average output power ultrashort pulses from fiber lasers implementing Graphene and Bismuth Selenide as saturable absorbers. Both nanomaterials were deposited on optical tapers because of the long light-matter interaction that improves the laser's induced damage threshold and the nanomaterials' saturation power while offering an effective absorption effect and high average output power. Consequently, we successfully obtained the 326th harmonic bunch of solitons with an average output power of 520 mW and 22 dB of signal to noise ratio was demonstrated in a fiber ring setup with graphene deposited on fiber taper. We also generated up to the 91st harmonic mode-locking of soliton bunches with an average output power of 308 mW by using a Bi_2Se_3 as saturable absorber.

Recommendations for Future Works

All the works about optical injection focused on the soliton regime, whereas it could be very interesting to explore in the future, the influence of external CW injection in longer cavities emitting square wave pulse in the DSR regime. In parallel, much work has been carried out on the generation of high energy pulses in the DSR regime. However, it can be further explored in the future. The performance

of square-wave pulse energy can be improved by implementing cascaded amplifiers inside the cavity. Future study on mode-locked DSR pulses may also focus on higher pulse repetition rate and better signal to noise ratio SNR to meet industrial standards. At the same time, it would be much of an interest to explore the implementation of nanomaterial SA in lengthy cavities to generate energetic pulses.

Moreover, the results concerning the emission of staircase pulses are very interesting and need more investigation. By filtering the output pulse, it can be of a great interest to investigate its nature and the mechanism on which it is built. Based on the recent works [152], [280] where DSR pulses can be spectrally tuned in a range of few tens of nanometers by adjusting the cavity losses and the birefringent filter [277], it would be very challenging to demonstrate this behavior by using a tunable output coupler in very long cavities pumped by Er:Yb amplifiers.

Future directions can include the approach attempted in Chapter 5 with tapered fibers, for example by choosing more appropriate deposition techniques of nano-materials. Indeed, a very promising deposition technique is spray-coating: apart for the tremendous advantages in terms of cost and scalability of such process, this method, if properly optimized, allows a very even, precise and fast deposition of the material. Other possible works in this fields could include the use of other layered materials, such as Black Phosphorus, MoS_2 and other TMDs (Transition Metal Dichalcogenenides): the former, for example, shows a direct bandgap only when it is isolated in the form of a monolayer, and excellent saturable absorption responses.

With this, it is hoped that this work will bring its contribution to the field of high power and energy fiber optics.

List of author's publications and conference proceedings

Publications

1. Y. Meng, M. Salhi, A. Niang, K. Guesmi, **G. Semaan**, and F. Sanchez, "Mode-locked Er:Yb-doped double-clad fiber laser with 75-nm tuning range," Opt. Lett., vol. 40, no. 7, p. 1153, Apr. 2015
2. Y. Meng, **G. Semaan**, M. Salhi, A. Niang, K. Guesmi, Z-C. Luo and F. Sanchez, "High power L-band mode-locked fiber laser based on topological insulator saturable absorber," Opt.Express, vol. 23, no. 18, p. 23053-23058, Aug. 2015
3. **G.Semaan**, F. Ben Braham, M.Salhi, Y.Meng, F.Bahloul and F.Sanchez, "Generation of high energy square-wave pulses in all anomalous dispersion Er :Yb passive mode locked fiber ring laser, " Opt.Express, vol. 24, no. 8, p. 8399-8404, Apr. 2016
4. K. Guesmi, **G.Semaan**, M. Salhi, Y. Meng, F.Bahloul, H. Leblond and F. Sanchez "L-band harmonic mode locked of single, two and three soliton bunches from C-band amplifier in a figure of eight fiber laser", Romanian Journal of Physics, vol. 61, issue 7-8 (2016)
5. **G. Semaan**, F. Ben Braham, J. Fourmont, M. Salhi, F.Bahloul, F. Sanchez, "10 μJ dissipative soliton resonance square pulse in a dual amplifier figure-of-eight double clad Er:Yb mode-locked fiber laser", Optics Letters, vol. 41, issue 20 (2016)
6. **G. Semaan**, F. Ben Braham, M. Salhi, F. Sanchez "Roadmap to high energy square pulses in anomalous dispersion fiber laser", Photonics Letters of Poland, vol. 8, issue 4 (2016).
7. **G. Semaan**, A.Komarov, M. Salhi and F. Sanchez "Study of harmonic mode lock stability under external continuous wave injection" Optics Communications, vol. 387 (2017).
8. K. Guesmi, F. Bahloul, **G. Semaan**, Y. Meng, M. Salhi, F. Sanchez "Widely tunable, narrow line width and low optical noise continuous wave all fiber Er :Yb co-doped double clad ring laser", Journal of Optics, vol. 19, issue 1 (2017)
9. **G. Semaan**, A. Niang, M. Salhi, F. Sanchez "Harmonic dissipative soliton resonance square pulses in an anomalous dispersion passively mode-locked

fiber ring laser", Laser Physics Letters, vol. 14, issue 5 (2017) (**IOPSELECT paper in 2017**).

10. F. Ben Braham, **G. Semaan**, F. Bahloul, M. Salhi, F. Sanchez "Experimental optimization of dissipative soliton resonance square-pulses in all anomalous passively mode-locked fiber laser", Journal of Optics (publishing in progress), 2017.
11. P. Mouchel, **G. Semaan**, A. Niang, M. Salhi, M. Le Flohic, F. Sanchez "High power passively mode-locked fiber laser based on graphene nanocoated optical taper ", Applied Physics Letters, vol. 111, issue 3 (2017).
12. **G. Semaan**, A. Komarov, A. Niang, M. Salhi and F. Sanchez "Spectral dynamics of square pulses in passive mode-locked fiber lasers", JSTQE (submitted), 2017.
13. A. Komarov, A. Dimitriev, K. Komarov, D. Meshcheriakov, **G. Semaan** and F. Sanchez "On the theory of passive mode-locked fiber lasers with phase-modulated rectangular pulses", PRA (Review in Progress), 2017.

Conference proceedings

1. **G. Semaan**, Y. Meng, M. Salhi, A. Niang, K. Guesmi and F. Sanchez "Laser à fibre double gaine dopée Er :Yb : Etude de l'accordabilité en longueur d'onde sur une plage de 75 nm en régime multi-impulsionnel" , Optique Bretagne 2015 – JNOG'35, Rennes, 3-6 July 2015,.
2. Y. Meng, K. Guesmi, A. Niang, M. Salhi, F. Bahloul, **G. Semaan** and F. Sanchez "1.6 μm laser emission from the Er:Yb doped double-clad fiber amplifier", ICTON'15, Budapest, 5-9 July 2015.
3. **G. Semaan**, Y. Meng, K. Guesmi, M. Salhi, Z-C Luo and F. Sanchez "High power passive mode-locked L-band fiber laser based on microfiber topological insulator saturable absorber", SPIE Photonics Europe, Brussels, 3-7 April 2016.
4. **G. Semaan**, P. Mouchel, M. Salhi, M. Le Flohic and F. Sanchez "Laser à fibre verrouillé en phase à base de graphène comme absorbant saturable depose sur un taper", Optique Bordeaux 2016 – JNOG'36, Bordeaux, 3-6 July 2016.
5. **G. Semaan**, F. Ben Braham, M. Salhi, Y. Meng, F. Bahloul and F. Sanchez "High energy square-wave generation from the Er:Yb passive mode-locked fiber ring laser", ICTON'16, Trento-Italy, 5-9 July 2016.
6. **G. Semaan**, P. Mouchel, M. Salhi, M. Le Flohic and F. Sanchez "Mode-locked fiber laser based on graphene saturable absorber", NNN Workshop Telecom 2016, Le Mans, 21 September 2016.
7. **G. Semaan**, P. Mouchel, M. Salhi, Y. Meng, M. Le Flohic and F. Sanchez "L'utilisation du graphène pour le verrouillage de mode dans les lasers à fibre", ICOPA4, ICMCB-CNRS Pessace Bordeaux, 5-7 December 2016.

8. M. Salhi, **G. Semaan**, F. Ben Braham, J. Fourmont, F. Bahloul and F. Sanchez "Route to high-energy dissipative soliton resonance pulse in a dual amplifier figure-of-eight fiber laser", SPIE Optics + Photonics, Prague, May 2017.
9. A. Niang, **G. Semaan**, F. Ben Braham, M. Salhi and F. Sanchez "Dynamics of dissipative soliton resonance square pulses in fiber lasers", ICTON'17, Gerona-Spain, 3-7 July 2017.
10. **G. Semaan**, F. Ben Braham, Y. Meng, M. Salhi and F. Sanchez "10 µJ square-wave pulses generation from a passively mode-locked figure-of-eight fiber laser", ACP 2017, Guangzhou China, 10-13 November 2017.

References

[1] T. H. Maiman, "Stimulated Optical Radiation in Ruby," *Nature*, vol. 187, no. 4736, pp. 493–494, août 1960.

[2] A. L. Schawlow and C. H. Townes, "Infrared and Optical Masers," *Phys. Rev.*, vol. 112, no. 6, pp. 1940–1949, décembre 1958.

[3] C. H. Townes, *A century of Nature*, Garwin, L. & Lincoln, T. University of Chicago Press, 2003.

[4] G. Overton, A. Nogee, D. Belforte, and C. Holton, "Annual Laser Market Review & Forecast: Where have all the lasers gone?," 23-Jan-2017. .

[5] R. W. Hellwarth, "Control of Fluorescent Pulsations," presented at the Advances in Quantum Electronics, 1961, p. 334.

[6] F. J. McClung and R. W. Hellwarth, "Characteristics of giant optical pulsations from ruby," *Proc. IEEE*, vol. 51, no. 1, pp. 46–53, Jan. 1963.

[7] K. Gürs and R. Müller, "Breitband-modulation durch steuerung der emission eines optischen masers (Auskoppelmodulation)," *Phys. Lett.*, vol. 5, pp. 179–181, juillet 1963.

[8] K. Gürs, "Beats and modulation in optical ruby laser," *Quantum Electron. III Columbia Univ. Press N. Y. 1964*, 1964.

[9] H. Statez and C. Tang, "Zeeman effect and nonlinear interactions between oscillationg laser modes," *Quantum Electron. III Columbia Univ. Press N. Y. 1964*, 1964.

[10] "Small-Signal Analysis of Internal (Coupling-Type) Modulation of Lasers," *J. Appl. Phys.*, vol. 35, no. 10, pp. 2870–2876, Oct. 1964.

[11] L. E. Hargrove, R. L. Fork, and M. A. Pollack, "Locking Of He–Ne Laser Modes induced by synchronous intracavity modulation," *Appl. Phys. Lett.*, vol. 5, no. 1, pp. 4–5, Jul. 1964.

[12] H. Mocker W. and R. J. Collins, "Mode competition and self-locking effects in a q-switched ruby laser," *Appl. Phys. Lett.*, vol. 7, no. 10, pp. 270–273, Nov. 1965.

[13] A. J. DeMaria, D. A. Stetser, and H. Heynau, "Self mode-locking of lasers with saturable absorbers," *Appl. Phys. Lett.*, vol. 8, no. 7, pp. 174–176, avril 1966.

[14] E. Snitzer, "Optical Maser Action of Nd^{+3} in a Barium Crown Glass," *Phys. Rev. Lett.*, vol. 7, no. 12, pp. 444–446, décembre 1961.

[15] C. J. Koester and E. Snitzer, "Amplification in a Fiber Laser," *Appl. Opt.*, vol. 3, no. 10, pp. 1182–1186, Oct. 1964.

[16] K. C. Kao and G. A. Hockham, "Dielectric-fibre surface waveguides for optical frequencies," *Proc. Inst. Electr. Eng.*, vol. 113, no. 7, pp. 1151–1158, Jul. 1966.

[17] R. J. Mears, L. Reekie, S. B. Poole, and D. N. Payne, "Neodymium-doped silica single-mode fibre lasers," *Electron. Lett.*, vol. 21, no. 17, pp. 738–740, Aug. 1985.

[18] R. J. Mears, L. Reekie, I. M. Jauncey, and D. N. Payne, "Low-noise erbium-doped fibre amplifier operating at 1.54 μm," *Electron. Lett.*, vol. 23, no. 19, pp. 1026–1028, Sep. 1987.

[19] D. C. Hanna *et al.*, "Continuous-wave oscillation of a monomode ytterbium-doped fibre laser," *Electron. Lett.*, vol. 24, no. 17, pp. 1111–1113, août 1988.

[20] D. C. Hanna *et al.*, "Continuous-wave oscillation of a monomode thulium-doped fibre laser," *Electron. Lett.*, vol. 24, no. 19, pp. 1222–1223, Sep. 1988.

[21] J. Y. Allain, J. F. Bayon, M. Monerie, P. Bernage, and P. Niay, "Ytterbium-doped silica fibre laser with intracore Bragg gratings operating at 1.02 μm," *Electron. Lett.*, vol. 29, no. 3, pp. 309–310, Feb. 1993.

[22] H. A. Haus, "Mode-locking of lasers," *IEEE J. Sel. Top. Quantum Electron.*, vol. 6, no. 6, pp. 1173–1185, Nov. 2000.

[23] T. Brabec, C. Spielmann, P. F. Curley, and F. Krausz, "Kerr lens mode locking," *Opt. Lett.*, vol. 17, no. 18, pp. 1292–1294, Sep. 1992.
[24] H. A. Haus, J. G. Fujimoto, and E. P. Ippen, "Structures for additive pulse mode locking," *JOSA B*, vol. 8, no. 10, pp. 2068–2076, Oct. 1991.
[25] K. Tamura, H. A. Haus, and E. P. Ippen, "Self-starting additive pulse mode-locked erbium fibre ring laser," *Electron. Lett.*, vol. 28, no. 24, pp. 2226–2228, Nov. 1992.
[26] M. E. Fermann, M. L. Stock, M. J. Andrejco, and Y. Silberberg, "Passive mode locking by using nonlinear polarization evolution in a polarization-maintaining erbium-doped fiber," *Opt. Lett.*, vol. 18, no. 11, pp. 894–896, Jun. 1993.
[27] C.-J. Chen, P. K. A. Wai, and C. R. Menyuk, "Soliton fiber ring laser," *Opt. Lett.*, vol. 17, no. 6, pp. 417–419, Mar. 1992.
[28] N. J. Doran and D. Wood, "Nonlinear-optical loop mirror," *Opt. Lett.*, vol. 13, no. 1, pp. 56–58, Jan. 1988.
[29] M. E. Fermann, F. Haberl, M. Hofer, and H. Hochreiter, "Nonlinear amplifying loop mirror," *Opt. Lett.*, vol. 15, no. 13, pp. 752–754, Jul. 1990.
[30] M. Salhi, A. Haboucha, H. Leblond, and F. Sanchez, "Theoretical study of figure-eight all-fiber laser," *Phys. Rev. A*, vol. 77, no. 3, p. 033828, Mar. 2008.
[31] M. Salhi, F. Amrani, H. Leblond, and F. Sanchez, "Analytical investigation of a figure-eight single-pulse all-fiber laser based on a nonlinear amplifying loop mirror," *Phys. Rev. A*, vol. 82, no. 4, p. 043834, Oct. 2010.
[32] F. Amrani, M. Salhi, P. Grelu, H. Leblond, and F. Sanchez, "Universal soliton pattern formations in passively mode-locked fiber lasers," *Opt. Lett.*, vol. 36, no. 9, p. 1545, May 2011.
[33] K. Guesmi *et al.*, "1.6 µm emission based on linear loss control in a Er:Yb doped double-clad fiber laser," *Opt. Lett.*, vol. 39, no. 22, p. 6383, Nov. 2014.
[34] Y. Meng *et al.*, "High power L-band mode-locked fiber laser based on topological insulator saturable absorber," *Opt. Express*, vol. 23, no. 18, pp. 23053–23058, Sep. 2015.
[35] Y. Meng, A. Niang, K. Guesmi, M. Salhi, and F. Sanchez, "1.61 µm high-order passive harmonic mode locking in a fiber laser based on graphene saturable absorber," *Opt. Express*, vol. 22, no. 24, pp. 29921–29926, Dec. 2014.
[36] Y. Meng, S. Zhang, X. Li, H. Li, J. Du, and Y. Hao, "Multiple-soliton dynamic patterns in a graphene mode-locked fiber laser," *Opt. Express*, vol. 20, no. 6, p. 6685, Mar. 2012.
[37] J. Proctor and J. N. Kutz, "Nonlinear mode-coupling for passive mode-locking: application of waveguide arrays, dual-core fibers, and/or fiber arrays," *Opt. Express*, vol. 13, no. 22, pp. 8933–8950, Oct. 2005.
[38] K. Intrachat and J. N. Kutz, "Theory and simulation of passive modelocking dynamics using a long-period fiber grating," *IEEE J. Quantum Electron.*, vol. 39, no. 12, pp. 1572–1578, Dec. 2003.
[39] A. Hasegawa and F. Tappert, "Transmission of stationary nonlinear optical pulses in dispersive dielectric fibers. I. Anomalous dispersion," *Appl. Phys. Lett.*, vol. 23, no. 3, pp. 142–144, août 1973.
[40] A. K. Komarov, K. P. Komarov, and F. M. Mitschke, "Phase-modulation bistability and threshold self-start of laser passive mode locking," *Phys. Rev. A*, vol. 65, no. 5, p. 053803, Apr. 2002.
[41] A. Komarov, K. Komarov, H. Leblond, and F. Sanchez, "Spectral-selective management of dissipative solitons in passive mode-locked fibre lasers," *J. Opt. Pure Appl. Opt.*, vol. 9, no. 12, p. 1149, 2007.
[42] A. Komarov, F. Amrani, A. Dmitriev, K. Komarov, and F. Sanchez, "Competition and coexistence of ultrashort pulses in passive mode-locked lasers under dissipative-soliton-resonance conditions," *Phys. Rev. A*, vol. 87, no. 2, Feb. 2013.

[43] F. Amrani *et al.*, "Passively mode-locked erbium-doped double-clad fiber laser operating at the 322nd harmonic," *Opt. Lett.*, vol. 34, no. 14, p. 2120, Jul. 2009.
[44] F. Sanchez *et al.*, "Manipulating dissipative soliton ensembles in passively mode-locked fiber lasers," *Opt. Fiber Technol.*, vol. 20, no. 6, pp. 562–574, Dec. 2014.
[45] F. Amrani, M. Salhi, A. Niang, A. Komarov, and F. Sanchez, "<title>Soliton pattern formation in figure-of-eight laser</title>," 2012, pp. 843403-843403–7.
[46] A. K. Komarov, K. P. Komarov, H. Leblond, and F. Sanchez, "Spectral control over the interaction of ultrashort pulses in fiber lasers," *Opt. Spectrosc.*, vol. 103, no. 5, pp. 825–830, Nov. 2007.
[47] A. Komarov, K. Komarov, A. Niang, and F. Sanchez, "Nature of soliton interaction in fiber lasers with continuous external optical injection," *Phys. Rev. A*, vol. 89, no. 1, p. 013833, Jan. 2014.
[48] A. Niang, F. Amrani, M. Salhi, H. Leblond, A. Komarov, and F. Sanchez, "Harmonic mode-locking in a fiber laser through continuous external optical injection," *Opt. Commun.*, vol. 312, pp. 1–6, Feb. 2014.
[49] A. Niang, F. Amrani, M. Salhi, H. Leblond, and F. Sanchez, "Influence of gain dynamics on dissipative soliton interaction in the presence of a continuous wave," *Phys. Rev. A*, vol. 92, no. 3, p. 033831, 2015.
[50] A. B. Grudinin, D. J. Richardson, and D. N. Payne, "Energy quantisation in figure eight fibre laser," *Electron. Lett.*, vol. 28, no. 1, pp. 67–68, Jan. 1992.
[51] N. N. Akhmediev, A. Ankiewicz, and J. M. Soto-Crespo, "Multisoliton Solutions of the Complex Ginzburg-Landau Equation," *Phys. Rev. Lett.*, vol. 79, no. 21, pp. 4047–4051, Nov. 1997.
[52] A. Chong, W. H. Renninger, and F. W. Wise, "All-normal-dispersion femtosecond fiber laser with pulse energy above 20nJ," *Opt. Lett.*, vol. 32, no. 16, pp. 2408–2410, Aug. 2007.
[53] W. H. Renninger, A. Chong, and F. W. Wise, "Pulse Shaping and Evolution in Normal-Dispersion Mode-Locked Fiber Lasers," *IEEE J. Sel. Top. Quantum Electron. Publ. IEEE Lasers Electro-Opt. Soc.*, vol. 18, no. 1, pp. 389–398, 2012.
[54] F. Li, P. K. A. Wai, and J. N. Kutz, "Geometrical description of the onset of multi-pulsing in mode-locked laser cavities," *JOSA B*, vol. 27, no. 10, pp. 2068–2077, Oct. 2010.
[55] W. Chang, A. Ankiewicz, J. M. Soto-Crespo, and N. Akhmediev, "Dissipative soliton resonances," *Phys. Rev. A*, vol. 78, no. 2, p. 023830, Aug. 2008.
[56] W. Chang, J. M. Soto-Crespo, A. Ankiewicz, and N. Akhmediev, "Dissipative soliton resonances in the anomalous dispersion regime," *Phys. Rev. A*, vol. 79, no. 3, p. 033840, Mar. 2009.
[57] N. Zhao *et al.*, "Dual-wavelength rectangular pulse Yb-doped fiber laser using a microfiber-based graphene saturable absorber," *Opt. Express*, vol. 22, no. 9, p. 10906, May 2014.
[58] A. C. S. Van Heel, "A New Method of transporting Optical Images without Aberrations," *Nature*, vol. 173, no. 4392, pp. 39–39, Jan. 1954.
[59] L. E. Curtiss, "Glass fiber optical devices," US3589793 A, 29-Jun-1971.
[60] D. Keck and P. Schultz, "Method of producing optical waveguide fibers," US3711262 A, 16-Jan-1973.
[61] W. G. French, J. B. MacChesney, P. B. O'Connor, and G. W. Tasker, "Optical Waveguides With Very Low Losses," *Bell Syst. Tech. J.*, vol. 53, no. 5, pp. 951–954, May 1974.
[62] M. J. . Digonnet, *Rare-Earth-Doped Fiber Lasers and Amplifiers, Revised and Expanded*. CRC Press, 2001.
[63] G. P. Agrawal, *Nonlinear Fiber Optics - 5th Edition*. Academic Press, 2012.
[64] D. Gloge, "Dispersion in Weakly Guiding Fibers," *Appl. Opt.*, vol. 10, no. 11, pp. 2442–2445, Nov. 1971.

[65] D. Marcuse, "Interdependence of waveguide and material dispersion," *Appl. Opt.*, vol. 18, no. 17, pp. 2930–2932, Sep. 1979.
[66] S. D. Jackson and T. A. King, "High-power diode-cladding-pumped Tm-doped silica fiber laser," *Opt. Lett.*, vol. 23, no. 18, pp. 1462–1464, Sep. 1998.
[67] R. H. Stolen and C. Lin, "Self-phase-modulation in silica optical fibers," *Phys. Rev. A*, vol. 17, no. 4, pp. 1448–1453, Apr. 1978.
[68] R. Boyd, *Nonlinear optics - 3rd edition*, Academic Press. San Jose, 2008.
[69] R. Stolen, "Phase-matched-stimulated four-photon mixing in silica-fiber waveguides," *IEEE J. Quantum Electron.*, vol. 11, no. 3, pp. 100–103, Mar. 1975.
[70] K. Tai, A. Hasegawa, and A. Tomita, "Observation of modulational instability in optical fibers," *Phys. Rev. Lett.*, vol. 56, no. 2, pp. 135–138, Jan. 1986.
[71] F. P. Kapron, D. B. Keck, and R. D. Maurer, "Radiation Losses in Glass Optical Waveguides," *Appl. Phys. Lett.*, vol. 17, pp. 423–425, Nov. 1970.
[72] J. Stone and C. a. Burrus, "Neodymium-doped silica lasers in end-pumped fiber geometry," *Appl. Phys. Lett.*, vol. 23, no. 7, pp. 388–389, Oct. 1973.
[73] J. T. Kringlebotn, K. Bl∅tekjaer, and C. N. Pannell, "Fiber optic sensor based on a sagnac interferometer including a recirculating-ring delay line with an edfa," *Fiber Integr. Opt.*, vol. 14, no. 3, pp. 265–285, Jan. 1995.
[74] E. Matsubara, K. Yamane, T. Sekikawa, and M. Yamashita, "Generation of 2.6 fs optical pulses using induced-phase modulation in a gas-filled hollow fiber," *JOSA B*, vol. 24, no. 4, pp. 985–989, Apr. 2007.
[75] F. X. Kaertner, L. R. Brovelli, D. Kopf, M. Kamp, I. G. Calasso, and U. Keller, "Control of solid state laser dynamics by semiconductor devices," *Opt. Eng.*, vol. 34, no. 7, pp. 2024–2036, 1995.
[76] C. Hönninger, R. Paschotta, F. Morier-Genoud, M. Moser, and U. Keller, "Q-switching stability limits of continuous-wave passive mode locking," *JOSA B*, vol. 16, no. 1, pp. 46–56, Jan. 1999.
[77] D. Kuizenga and A. Siegman, "FM and AM mode locking of the homogeneous laser - Part I: Theory," *IEEE J. Quantum Electron.*, vol. 6, no. 11, pp. 694–708, Nov. 1970.
[78] H. Haus, "A theory of forced mode locking," *IEEE J. Quantum Electron.*, vol. 11, no. 7, pp. 323–330, Jul. 1975.
[79] U. Keller *et al.*, "Semiconductor saturable absorber mirrors (SESAM's) for femtosecond to nanosecond pulse generation in solid-state lasers," *IEEE J. Sel. Top. Quantum Electron.*, vol. 2, no. 3, pp. 435–453, Sep. 1996.
[80] O. Okhotnikov, A. Grudinin, and M. Pessa, "Ultra-fast fibre laser systems based on SESAM technology: new horizons and applications," *New J. Phys.*, vol. 6, no. 1, p. 177, 2004.
[81] S. Y. Set *et al.*, "Mode-locked fiber lasers based on a saturable absorber incorporating carbon nanotubes," in *OFC 2003 Optical Fiber Communications Conference, 2003.*, 2003, pp. PD44-P1-3 vol.3.
[82] Q. Bao *et al.*, "Atomic-Layer Graphene as a Saturable Absorber for Ultrafast Pulsed Lasers," *Adv. Funct. Mater.*, vol. 19, no. 19, pp. 3077–3083, Oct. 2009.
[83] T. Hasan *et al.*, "Nanotube–Polymer Composites for Ultrafast Photonics," *Adv. Mater.*, vol. 21, no. 38–39, pp. 3874–3899, Oct. 2009.
[84] J. L. Boulnois, A. Van Lerberghe, P. Cottin, F. T. Arecchi, and G. P. Puccioni, "Self pulsing in a CO2 ring laser with an injected signal," *Opt. Commun.*, vol. 58, no. 2, pp. 124–129, May 1986.
[85] E. Brun, B. Derighetti, D. Meier, R. Holzner, and M. Ravani, "Observation of order and chaos in a nuclear spin–flip laser," *JOSA B*, vol. 2, no. 1, pp. 156–167, Jan. 1985.

[86] L. A. Lugiato, L. M. Narducci, D. K. Bandy, and C. A. Pennise, "Breathing, spiking and chaos in a laser with injected signal," *Opt. Commun.*, vol. 46, no. 1, pp. 64–68, Jun. 1983.
[87] J. R. Tredicce, F. T. Arecchi, G. L. Lippi, and G. P. Puccioni, "Instabilities in lasers with an injected signal," *JOSA B*, vol. 2, no. 1, pp. 173–183, Jan. 1985.
[88] R. Lang, "Injection locking properties of a semiconductor laser," *IEEE J. Quantum Electron.*, vol. 18, no. 6, pp. 976–983, Jun. 1982.
[89] E. G. Lariontsev, I. Zolotoverkh, P. Besnard, and G. M. Stéphan, "Injection locking properties of a microchip laser," *Eur. Phys. J. - At. Mol. Opt. Plasma Phys.*, vol. 5, no. 1, pp. 107–117, Jan. 1999.
[90] C. Weiss, E. Bava, A. D. Marchi, and A. Godone, "Injection locking of an optically pumped FIR laser," *IEEE J. Quantum Electron.*, vol. 16, no. 5, pp. 498–499, May 1980.
[91] S. Kobayashi and T. Kimura, "Injection locking characteristics of an AlGaAs semiconductor laser," *IEEE J. Quantum Electron.*, vol. 16, no. 9, pp. 915–917, Sep. 1980.
[92] F. Mogensen, H. Olesen, and G. Jacobsen, "FM noise suppression and linewidth reduction in an injection-locked semiconductor laser," *Electron. Lett.*, vol. 21, no. 16, pp. 696–697, Aug. 1985.
[93] M. Bondiou, R. Gabet, G. M. Stéphan, and P. Besnard, "Linewidth of an optically injected semiconductor laser," *J. Opt. B Quantum Semiclassical Opt.*, vol. 2, no. 1, p. 41, 2000.
[94] W. H. Chung, H. Y. Tam, L. Y. Chan, and P. K. A. Wai, "Single output polarization control of fiber DFB laser using injection locking," in *Optical Fiber Communication Conference and Exhibit*, 2002, pp. 650–651.
[95] T. Pawletko, M. Houssin, M. Knoop, M. Vedel, and F. Vedel, "High power broad-area diode laser at 794 nm injected by an external cavity laser," *Opt. Commun.*, vol. 174, no. 1, pp. 223–229, Jan. 2000.
[96] Y. Liu, H.-K. Liu, and Y. Braiman, "Simultaneous injection locking of couples of high-power broad-area lasers driven by a common current source," *Appl. Opt.*, vol. 41, no. 24, pp. 5036–5039, Aug. 2002.
[97] D. Y. Tang, L. M. Zhao, B. Zhao, and A. Q. Liu, "Mechanism of multisoliton formation and soliton energy quantization in passively mode-locked fiber lasers," *Phys. Rev. A*, vol. 72, no. 4, p. 043816, Oct. 2005.
[98] A. K. Komarov and K. P. Komarov, "Multistability and hysteresis phenomena in passive mode-locked lasers," *Phys. Rev. E*, vol. 62, pp. R7607–R7610, Dec. 2000.
[99] B. Ortaç, A. Hideur, G. Martel, and M. Brunel, "2-GHz passive harmonically mode-locked Yb-doped double-clad fiber laser," *Appl. Phys. B*, vol. 81, no. 4, pp. 507–509, Jun. 2005.
[100] G. Sobon, K. Krzempek, P. Kaczmarek, K. M. Abramski, and M. Nikodem, "10 GHz passive harmonic mode-locking in Er–Yb double-clad fiber laser," *Opt. Commun.*, vol. 284, no. 18, pp. 4203–4206, Aug. 2011.
[101] C. Lecaplain and P. Grelu, "Multi-gigahertz repetition-rate-selectable passive harmonic mode locking of a fiber laser," *Opt. Express*, vol. 21, no. 9, p. 10897, May 2013.
[102] H. Leblond, A. Niang, F. Amrani, M. Salhi, and F. Sanchez, "Motion of solitons of the complex Ginzburg-Landau equation: The effect of an external frequency-shifted source," *Phys. Rev. A*, vol. 88, p. 033809, 2013.
[103] A. Niang, F. Amrani, M. Salhi, H. Leblond, A. Komarov, and F. Sanchez, "Harmonic mode-locking in a fiber laser through continuous external optical injection," *Opt. Commun.*, vol. 312, pp. 1–6, Feb. 2014.
[104] G. H. M. van Tartwijk and D. Lenstra, "Semiconductor lasers with optical injection and feedback," *Quantum Semiclassical Opt. J. Eur. Opt. Soc. Part B*, vol. 7, no. 2, p. 87, 1995.

[105] S. Wieczorek, B. Krauskopf, T. B. Simpson, and D. Lenstra, "The dynamical complexity of optically injected semiconductor lasers," *Phys. Rep.*, vol. 416, no. 1–2, pp. 1–128, Sep. 2005.
[106] M. Margalit, M. Orenstein, and H. A. Haus, "Injection locking of a passively mode-locked laser," *IEEE J. Quantum Electron.*, vol. 32, no. 1, pp. 155–160, Jan. 1996.
[107] N. Rebrova, T. Habruseva, G. Huyet, and S. P. Hegarty, "Stabilization of a passively mode-locked laser by continuous wave optical injection," *Appl. Phys. Lett.*, vol. 97, no. 10, p. 101105, Sep. 2010.
[108] T. Habruseva, G. Huyet, and S. P. Hegarty, "Dynamics of Quantum-Dot Mode-Locked Lasers With Optical Injection," *IEEE J. Sel. Top. Quantum Electron.*, vol. 17, no. 5, pp. 1272–1279, Sep. 2011.
[109] M. Salhi, H. Leblond, and F. Sanchez, "High power tunable all fiber double-clad Er:Yb:silicate fiber laser," *Opt. Commun.*, vol. 247, no. 1–3, pp. 181–185, Mar. 2005.
[110] S. M. J. Kelly, "Characteristic sideband instability of periodically amplified average soliton," *Electron. Lett.*, vol. 28, no. 8, pp. 806–807, Apr. 1992.
[111] A. Niang, F. Amrani, M. Salhi, H. Leblond, A. Komarov, and F. Sanchez, "Harmonic mode-locking in a fiber laser through continuous external optical injection," *Opt. Commun.*, vol. 312, pp. 1–6, Feb. 2014.
[112] A. Komarov, K. Komarov, and F. Sanchez, "Quantization of binding energy of structural solitons in passive mode-locked fiber lasers," *Phys. Rev. A*, vol. 79, no. 3, p. 033807, Mar. 2009.
[113] *Dissipative Solitons | Nail Akhmediev | Springer*. .
[114] F. Amrani, A. Haboucha, M. Salhi, H. Leblond, A. Komarov, and F. Sanchez, "Dissipative solitons compounds in a fiber laser. Analogy with the states of the matter," *Appl. Phys. B*, vol. 99, no. 1–2, pp. 107–114, Oct. 2009.
[115] A. Komarov and F. Sanchez, "Structural dissipative solitons in passive mode-locked fiber lasers," *Phys. Rev. E*, vol. 77, no. 6, p. 066201, Jun. 2008.
[116] H. A. Haus, "Theory of mode locking with a fast saturable absorber," *J. Appl. Phys.*, vol. 46, no. 7, pp. 3049–3058, Jul. 1975.
[117] K. Komarov and H.-W. U. Department of Physics Edinburgh, Scotland, "Theory of stationary ultarshort pulses in solid-state laserswith passive mode locking," *Opt Spectrosc Engl Transl*, vol. 60:2, pp. 231–234, 1986.
[118] V. Ginzburg and L. Landau, "Toward the superconductivity theory," *Zhurnal Eksp Yheoret Phys.*, vol. 29, p. 1064, 1950.
[119] J. M. Soto-Crespo, N. N. Akhmediev, and V. V. Afanasjev, "Stability of the pulselike solutions of the quintic complex Ginzburg–Landau equation," *JOSA B*, vol. 13, no. 7, pp. 1439–1449, Jul. 1996.
[120] K. Tamura, E. P. Ippen, and H. A. Haus, "Pulse dynamics in stretched-pulse fiber lasers," *Appl. Phys. Lett.*, vol. 67, no. 2, pp. 158–160, Jul. 1995.
[121] V. L. Kalashnikov, E. Podivilov, A. Chernykh, and A. Apolonski, "Chirped-pulse oscillators: theory and experiment," *Appl. Phys. B*, vol. 83, no. 4, p. 503, Jun. 2006.
[122] W. H. Renninger, A. Chong, and F. W. Wise, "Giant-chirp oscillators for short-pulse fiber amplifiers," *Opt. Lett.*, vol. 33, no. 24, pp. 3025–3027, Dec. 2008.
[123] B. G. Bale, S. Boscolo, and S. K. Turitsyn, "Dissipative dispersion-managed solitons in mode-locked lasers," *Opt. Lett.*, vol. 34, no. 21, pp. 3286–3288, Nov. 2009.
[124] F. O. Ilday, J. R. Buckley, F. W. Wise, and W. G. Clark, "Self-Similar Evolution of Parabolic Pulses in a Laser," *Phys. Rev. Lett.*, vol. 92, no. 21, May 2004.
[125] J. An, D. Kim, J. W. Dawson, M. J. Messerly, and C. P. J. Barty, "Grating-less, fiber-based oscillator that generates 25 nJ pulses at 80 MHz, compressible to 150 fs," *Opt. Lett.*, vol. 32, no. 14, pp. 2010–2012, Jul. 2007.

[126] A. Hideur, T. Chartier, M. Brunel, S. Louis, C. Özkul, and F. Sanchez, "Generation of high energy femtosecond pulses from a side-pumped Yb-doped double-clad fiber laser," *Appl. Phys. Lett.*, vol. 79, no. 21, pp. 3389–3391, Nov. 2001.
[127] B. Ortaç, M. Baumgartl, J. Limpert, and A. Tünnermann, "Approaching microjoule-level pulse energy with mode-locked femtosecond fiber lasers," *Opt. Lett.*, vol. 34, no. 10, pp. 1585–1587, May 2009.
[128] E. J. R. Kelleher *et al.*, "Generation and direct measurement of giant chirp in a passively mode-locked laser," *Opt. Lett.*, vol. 34, no. 22, pp. 3526–3528, Nov. 2009.
[129] W. Chang, A. Ankiewicz, J. M. Soto-Crespo, and N. Akhmediev, "Dissipative soliton resonances," *Phys. Rev. A*, vol. 78, no. 2, p. 023830, août 2008.
[130] P. Grelu, W. Chang, A. Ankiewicz, J. M. Soto-Crespo, and N. Akhmediev, "Dissipative soliton resonance as a guideline for high-energy pulse laser oscillators," *J. Opt. Soc. Am. B*, vol. 27, no. 11, p. 2336, Nov. 2010.
[131] E. Ding, P. Grelu, and J. N. Kutz, "Dissipative soliton resonance in a passively mode-locked fiber laser," *Opt. Lett.*, vol. 36, no. 7, pp. 1146–1148, Apr. 2011.
[132] V. L. Kalashnikov, "Chirped dissipative solitons of the complex cubic-quintic nonlinear Ginzburg-Landau equation," *Phys. Rev. E*, vol. 80, no. 4, Oct. 2009.
[133] V. L. Kalashnikov and A. Apolonski, "Energy scalability of mode-locked oscillators: a completely analytical approach to analysis," *Opt. Express*, vol. 18, no. 25, pp. 25757–25770, Dec. 2010.
[134] X. Zhang *et al.*, "Square-wave pulse with ultra-wide tuning range in a passively mode-locked fiber laser," *Opt. Lett.*, vol. 37, no. 8, p. 1334, Apr. 2012.
[135] L. Duan, X. Liu, D. Mao, L. Wang, and G. Wang, "Experimental observation of dissipative soliton resonance in an anomalous-dispersion fiber laser," *Opt. Express*, vol. 20, no. 1, p. 265, Jan. 2012.
[136] Z.-C. Luo, W.-J. Cao, Z.-B. Lin, Z.-R. Cai, A.-P. Luo, and W.-C. Xu, "Pulse dynamics of dissipative soliton resonance with large duration-tuning range in a fiber ring laser," *Opt. Lett.*, vol. 37, no. 22, p. 4777, Nov. 2012.
[137] T. Liu, D. Jia, Y. Liu, Z. Wang, and T. Yang, "Generation of microseconds-duration square pulses in a passively mode-locked fiber laser," *Opt. Commun.*, vol. 356, pp. 416–420, Dec. 2015.
[138] L. Mei *et al.*, "Width and amplitude tunable square-wave pulse in dual-pump passively mode-locked fiber laser," *Opt. Lett.*, vol. 39, no. 11, p. 3235, Jun. 2014.
[139] X. Wu, D. Y. Tang, H. Zhang, and L. M. Zhao, "Dissipative soliton resonance in an all-normaldispersion erbium-doped fiber laser," *Opt. Express*, vol. 17, no. 7, p. 5580, Mar. 2009.
[140] J. h Yang *et al.*, "Observation of Dissipative Soliton Resonance in a Net-Normal Dispersion Figure-of-Eight Fiber Laser," *IEEE Photonics J.*, vol. 5, no. 3, pp. 1500806–1500806, Jun. 2013.
[141] S.-K. Wang, Q.-Y. Ning, A.-P. Luo, Z.-B. Lin, Z.-C. Luo, and W.-C. Xu, "Dissipative soliton resonance in a passively mode-locked figure-eight fiber laser," *Opt. Express*, vol. 21, no. 2, pp. 2402–2407, Jan. 2013.
[142] K. Krzempek, "Dissipative soliton resonances in all-fiber Er-Yb double clad figure-8 laser," *Opt. Express*, vol. 23, no. 24, p. 30651, Nov. 2015.
[143] G. Semaan, F. Ben Braham, M. Salhi, Y. Meng, F. Bahloul, and F. Sanchez, "Generation of high energy square-wave pulses in all anomalous dispersion Er:Yb passive mode locked fiber ring laser," *Opt. Express*, vol. 24, no. 8, p. 8399, Apr. 2016.
[144] G. Semaan, F. B. Braham, J. Fourmont, M. Salhi, F. Bahloul, and F. Sanchez, "10 µJ dissipative soliton resonance square pulse in a dual amplifier figure-of-eight double-clad Er:Yb mode-locked fiber laser," *Opt. Lett.*, vol. 41, no. 20, pp. 4767–4770, Oct. 2016.

[145] K. Krzempek, J. Sotor, and K. Abramski, "Compact all-fiber figure-9 dissipative soliton resonance mode-locked double-clad Er:Yb laser," *Opt. Lett.*, vol. 41, no. 21, pp. 4995–4998, Nov. 2016.
[146] X. Li *et al.*, "Long-cavity passively mode-locked fiber ring laser with high-energy rectangular-shape pulses in anomalous dispersion regime," *Opt. Lett.*, vol. 35, no. 19, pp. 3249–3251, Oct. 2010.
[147] P. Grelu, W. Chang, A. Ankiewicz, J. M. Soto-Crespo, and N. Akhmediev, "Dissipative soliton resonance as a guideline for high-energy pulse laser oscillators," *J. Opt. Soc. Am. B*, vol. 27, no. 11, p. 2336, Nov. 2010.
[148] F. Ben Braham, G. Semaan, F. Bahloul, M. Salhi, and F. Sanchez, "Experimental optimization of dissipative soliton resonance square pulses in all anomalous passively mode-locked fiber laser," *Journal of Optics*, p. Submitted.
[149] J. Liu *et al.*, "Generation and evolution of mode-locked noise-like square-wave pulses in a large-anomalous-dispersion Er-doped ring fiber laser," *Opt. Express*, vol. 23, no. 5, pp. 6418–6427, Mar. 2015.
[150] F. Bahloul, K. Guesmi, M. Salhi, F. Sanchez, and R. Attia, "Control of the square pulse properties in figure-of-eight microstructured fiber laser," *Opt. Eng.*, vol. 55, no. 2, p. 026102, Feb. 2016.
[151] L. Liu *et al.*, "Wave-breaking-free pulse in an all-fiber normal-dispersion Yb-doped fiber laser under dissipative soliton resonance condition," *Opt. Express*, vol. 21, no. 22, pp. 27087–27092, Nov. 2013.
[152] Y. Xu *et al.*, "Dissipative Soliton Resonance in a Wavelength-Tunable Thulium-Doped Fiber Laser With Net-Normal Dispersion," *IEEE Photonics J.*, vol. 7, no. 3, pp. 1–7, Jun. 2015.
[153] H. Yu, R. Tao, X. Wang, P. Zhou, and J. Chen, "240 W high-average-power square-shaped nanosecond all-fiber-integrated laser with near diffraction-limited beam quality," *Appl. Opt.*, vol. 53, no. 28, pp. 6409–6413, Oct. 2014.
[154] J. Zhao *et al.*, "100 W dissipative soliton resonances from a thulium-doped double-clad all-fiber-format MOPA system," *Opt. Express*, vol. 24, no. 11, pp. 12072–12081, May 2016.
[155] T. Du *et al.*, "1.2-W average-power, 700-W peak-power, 100-ps dissipative soliton resonance in a compact Er:Yb co-doped double-clad fiber laser," *Opt. Lett.*, vol. 42, no. 3, pp. 462–465, Feb. 2017.
[156] A. Komarov, A. Dmitriev, K. Komarov, D. Meshcheriakov, and F. Sanchez, "Spectral-doublet rectangular pulses in passive mode-locked fiber lasers with anomalous dispersion," *Phys. Rev. A*, vol. 94, no. 4, p. 043827, Oct. 2016.
[157] G. Semaan, F. B. Braham, J. Fourmont, M. Salhi, F. Bahloul, and F. Sanchez, "10 µJ dissipative soliton resonance square pulse in a dual amplifier figure-of-eight double-clad Er:Yb mode-locked fiber laser," *Opt. Lett.*, vol. 41, no. 20, pp. 4767–4770, Oct. 2016.
[158] G. Semaan, A. Niang, M. Salhi, and F. Sanchez, "Harmonic dissipative soliton resonance square pulses in an anomalous dispersion passively mode-locked fiber ring laser," *Laser Phys. Lett.*, vol. 14, no. 5, p. 055401, 2017.
[159] T. R. Taha and M. I. Ablowitz, "Analytical and numerical aspects of certain nonlinear evolution equations. II. Numerical, nonlinear Schrödinger equation," *J. Comput. Phys.*, vol. 55, no. 2, pp. 203–230, Aug. 1984.
[160] "Principles of Laser Dynamics - 1st Edition." [Online]. Available: https://www.elsevier.com/books/principles-of-laser-dynamics/khanin/978-0-444-89696-4. [Accessed: 06-Feb-2017].
[161] A. K. Komarov, K. P. Komarov, and F. M. Mitschke, "Phase-modulation bistability and threshold self-start of laser passive mode locking," *Phys. Rev. A*, vol. 65, no. 5, p. 053803, Apr. 2002.

[162] A. Komarov and F. Sanchez, "Structural dissipative solitons in passive mode-locked fiber lasers," *Phys. Rev. E*, vol. 77, no. 6, p. 066201, Jun. 2008.
[163] K. S. Novoselov *et al.*, "Two-dimensional gas of massless Dirac fermions in graphene," *Nature*, vol. 438, no. 7065, pp. 197–200, Nov. 2005.
[164] K. S. Novoselov *et al.*, "Two-dimensional atomic crystals," *Proc. Natl. Acad. Sci. U. S. A.*, vol. 102, no. 30, pp. 10451–10453, Jul. 2005.
[165] K. S. Novoselov *et al.*, "Electric Field Effect in Atomically Thin Carbon Films," *Science*, vol. 306, no. 5696, pp. 666–669, Oct. 2004.
[166] A. K. Geim and I. V. Grigorieva, "Van der Waals heterostructures," *Nature*, vol. 499, no. 7459, pp. 419–425, Jul. 2013.
[167] P. Rivera *et al.*, "Observation of long-lived interlayer excitons in monolayer MoSe2–WSe2 heterostructures," *Nat. Commun.*, vol. 6, p. 6242, Feb. 2015.
[168] C. R. Dean *et al.*, "Boron nitride substrates for high-quality graphene electronics," *Nat. Nanotechnol.*, vol. 5, no. 10, pp. 722–726, Oct. 2010.
[169] B. Hunt *et al.*, "Massive Dirac Fermions and Hofstadter Butterfly in a van der Waals Heterostructure," *Science*, vol. 340, no. 6139, pp. 1427–1430, Jun. 2013.
[170] U. Keller, "Recent developments in compact ultrafast lasers," *Nature*, vol. 424, no. 6950, pp. 831–838, Aug. 2003.
[171] U. Keller, "Ultrafast solid-state lasers," vol. 46, B.-P. in Optics, Ed. Elsevier, 2004, pp. 1–115.
[172] O. E. Martinez, R. L. Fork, and J. P. Gordon, "Theory of passively mode-locked lasers for the case of a nonlinear complex-propagation coefficient," *J. Opt. Soc. Am. B Opt. Phys.*, vol. 2, pp. 753–760, May 1985.
[173] N. N. Akhmediev, A. Ankiewicz, M. J. Lederer, and B. Luther-Davies, "Ultrashort pulses generated by mode-locked lasers with either a slow or a fast saturable-absorber response," *Opt. Lett.*, vol. 23, no. 4, pp. 280–282, Feb. 1998.
[174] V. L. Kalashnikov, D. O. Krimer, I. G. Poloyko, and V. P. Mikhailov, "Ultrashort pulse generation in cw solid-state lasers with semiconductor saturable absorber in the presence of the absorption linewidth enhancement," *Opt. Commun.*, vol. 159, no. 4–6, pp. 237–242, Jan. 1999.
[175] F. X. Kurtner, J. A. der Au, and U. Keller, "Mode-locking with slow and fast saturable absorbers-what's the difference?," *IEEE J. Sel. Top. Quantum Electron.*, vol. 4, no. 2, pp. 159–168, Mar. 1998.
[176] E. Ugolotti, A. Schmidt, V. Petrov, J. Wan Kim, D.-I. Yeom, and F. Rotermund, "Graphene mode-locked femtosecond Yb:KLuW laser," *Appl. Phys. Lett.*, vol. 101, no. 16, p. 161112, Oct. 2012.
[177] S. D. D. D. Cafiso *et al.*, "Sub-100-fs Cr:YAG laser mode-locked by monolayer graphene saturable absorber," *Opt. Lett.*, vol. 38, no. 10, pp. 1745–1747, May 2013.
[178] I. H. Baek *et al.*, "Efficient Mode-Locking of Sub-70-fs Ti:Sapphire Laser by Graphene Saturable Absorber," *Appl. Phys. Express*, vol. 5, no. 3, p. 032701, Feb. 2012.
[179] C. Zhao *et al.*, "Ultra-short pulse generation by a topological insulator based saturable absorber," *Appl. Phys. Lett.*, vol. 101, no. 21, p. 211106, Nov. 2012.
[180] J. Xu, J. Liu, S. Wu, Q.-H. Yang, and P. Wang, "Graphene oxide mode-locked femtosecond erbium-doped fiber lasers," *Opt. Express*, vol. 20, no. 14, p. 15474, Jul. 2012.
[181] J. Xu *et al.*, "Dissipative soliton generation from a graphene oxide mode-locked Er-doped fiber laser," *Opt. Express*, vol. 20, no. 21, pp. 23653–23658, Oct. 2012.
[182] B. V. Cunning, C. L. Brown, and D. Kielpinski, "Low-loss flake-graphene saturable absorber mirror for laser mode-locking at sub-200-fs pulse duration," *Appl. Phys. Lett.*, vol. 99, no. 26, p. 261109, Dec. 2011.

[183] F. Lou *et al.*, "High-efficiency femtosecond Yb:$Gd_3Al_{0.5}Ga_{4.5}O_{12}$ mode-locked laser based on reduced graphene oxide," *Opt. Lett.*, vol. 38, no. 20, pp. 4189–4192, Oct. 2013.
[184] J.-L. Xu, X.-L. Li, Y.-Z. Wu, X.-P. Hao, J.-L. He, and K.-J. Yang, "Graphene saturable absorber mirror for ultra-fast-pulse solid-state laser," *Opt. Lett.*, vol. 36, no. 10, pp. 1948–1950, May 2011.
[185] X. Jin-Long *et al.*, "Performance of large-area few-layer graphene saturable absorber in femtosecond bulk laser," *Appl. Phys. Lett.*, vol. 99, no. 26, p. 261107, Dec. 2011.
[186] J. Ma *et al.*, "Generation of 30 fs pulses from a diode-pumped graphene mode-locked Yb:$CaYAlO_4$ laser," *Opt. Lett.*, vol. 41, no. 5, pp. 890–893, Mar. 2016.
[187] J. Sotor, G. Sobon, W. Macherzynski, P. Paletko, K. Grodecki, and K. M. Abramski, "Mode-locking in Er-doped fiber laser based on mechanically exfoliated Sb_2Te_3 saturable absorber," *Opt. Mater. Express*, vol. 4, no. 1, p. 1, Jan. 2014.
[188] H. Zhang *et al.*, "Molybdenum disulfide (MoS_2) as a broadband saturable absorber for ultra-fast photonics," *Opt. Express*, vol. 22, no. 6, pp. 7249–7260, Mar. 2014.
[189] H. Liu *et al.*, "Femtosecond pulse erbium-doped fiber laser by a few-layer MoS_2 saturable absorber," *Opt. Lett.*, vol. 39, no. 15, pp. 4591–4594, Aug. 2014.
[190] J. Sotor, G. Sobon, M. Kowalczyk, W. Macherzynski, P. Paletko, and K. M. Abramski, "Ultrafast thulium-doped fiber laser mode locked with black phosphorus," *Opt. Lett.*, vol. 40, no. 16, pp. 3885–3888, Aug. 2015.
[191] Y.-W. Song, S. Yamashita, C. S. Goh, and S. Y. Set, "Carbon nanotube mode lockers with enhanced nonlinearity via evanescent field interaction in D-shaped fibers," *Opt. Lett.*, vol. 32, no. 2, pp. 148–150, Jan. 2007.
[192] Y.-W. Song, S.-Y. Jang, W. Han, and M.-K. Bae, "Graphene mode-lockers for fiber lasers functioned with evanescent field interaction," *Appl. Phys. Lett.*, vol. 96, no. 5, p. 051122, Feb. 2010.
[193] J. Sotor, G. Sobon, K. Grodecki, and K. M. Abramski, "Mode-locked erbium-doped fiber laser based on evanescent field interaction with Sb_2Te_3 topological insulator," *Appl. Phys. Lett.*, vol. 104, no. 25, p. 251112, Jun. 2014.
[194] J. Wang *et al.*, "Evanescent-Light Deposition of Graphene Onto Tapered Fibers for Passive Q-Switch and Mode-Locker," *IEEE Photonics J.*, vol. 4, no. 5, pp. 1295–1305, Oct. 2012.
[195] H. Wang *et al.*, "Ethanol catalytic deposition of MoS_2 on tapered fiber," *Photonics Res.*, vol. 3, no. 3, p. A102, Jun. 2015.
[196] W. Liu *et al.*, "70-fs mode-locked erbium-doped fiber laser with topological insulator," *Sci. Rep.*, vol. 6, p. 19997, Jan. 2016.
[197] J. Sotor, G. Sobon, and K. M. Abramski, "Sub-130 fs mode-locked Er-doped fiber laser based on topological insulator," *Opt. Express*, vol. 22, no. 11, p. 13244, Jun. 2014.
[198] M. Jung *et al.*, "Mode-locked pulse generation from an all-fiberized, Tm-Ho-codoped fiber laser incorporating a graphene oxide-deposited side-polished fiber," *Opt. Express*, vol. 21, no. 17, pp. 20062–20072, Aug. 2013.
[199] N. H. Park, H. Jeong, S. Y. Choi, M. H. Kim, F. Rotermund, and D.-I. Yeom, "Monolayer graphene saturable absorbers with strongly enhanced evanescent-field interaction for ultrafast fiber laser mode-locking," *Opt. Express*, vol. 23, no. 15, pp. 19806–19812, Jul. 2015.
[200] J. Bogusławski *et al.*, "Investigation on pulse shaping in fiber laser hybrid mode-locked by Sb_2Te_3 saturable absorber," *Opt. Express*, vol. 23, no. 22, pp. 29014–29023, Nov. 2015.
[201] J. D. Zapata, D. Steinberg, L. A. M. Saito, R. E. P. de Oliveira, A. M. Cárdenas, and E. A. T. de Souza, "Efficient graphene saturable absorbers on D-shaped optical fiber for ultrashort pulse generation," *Sci. Rep.*, vol. 6, p. 20644, Feb. 2016.
[202] A. Martinez and S. Yamashita, "10 GHz fundamental mode fiber laser using a graphene saturable absorber," *Appl. Phys. Lett.*, vol. 101, no. 4, p. 041118, Jul. 2012.

[203] T. Chen, C. Liao, D. N. Wang, and Y. Wang, "Passively mode-locked fiber laser by using monolayer chemical vapor deposition of graphene on D-shaped fiber," *Appl. Opt.*, vol. 53, no. 13, pp. 2828–2832, May 2014.
[204] K. Wu, X. Zhang, J. Wang, and J. Chen, "463-MHz fundamental mode-locked fiber laser based on few-layer MoS_2 saturable absorber," *Opt. Lett.*, vol. 40, no. 7, pp. 1374–1377, Apr. 2015.
[205] L.-N. Duan, Y.-L. Su, Y.-G. Wang, L. Li, X. Wang, and Y.-S. Wang, "Passively mode-locked erbium-doped fiber laser via a D-shape-fiber-based MoS 2 saturable absorber with a very low nonsaturable loss," *Chin. Phys. B*, vol. 25, no. 2, p. 024206, 2016.
[206] M. Liu *et al.*, "Microfiber-based few-layer MoS_2 saturable absorber for 2.5 GHz passively harmonic mode-locked fiber laser," *Opt. Express*, vol. 22, no. 19, pp. 22841–22846, Sep. 2014.
[207] Z. Tian *et al.*, "Mode-locked thulium fiber laser with MoS 2," *Laser Phys. Lett.*, vol. 12, no. 6, p. 065104, 2015.
[208] L. Li *et al.*, "WS_2/fluorine mica (FM) saturable absorbers for all-normal-dispersion mode-locked fiber laser," *Opt. Express*, vol. 23, no. 22, pp. 28698–28706, Nov. 2015.
[209] D. Mao *et al.*, "WS_2 mode-locked ultrafast fiber laser," *Sci. Rep.*, vol. 5, p. srep07965, Jan. 2015.
[210] H. Chen, I. L. Li, S. Ruan, T. Guo, and P. Yan, "Fiber-integrated tungsten disulfide saturable absorber (mirror) for pulsed fiber lasers," *Opt. Eng.*, vol. 55, no. 8, pp. 081318–081318, 2016.
[211] R. Khazaeinezhad *et al.*, "Ultrafast Pulsed All-Fiber Laser Based on Tapered Fiber Enclosed by Few-Layer WS2 Nanosheets," *IEEE Photonics Technol. Lett.*, vol. 27, no. 15, pp. 1581–1584, Aug. 2015.
[212] M. H. M. Ahmed, A. A. Latiff, H. Arof, and S. W. Harun, "Ultrafast erbium-doped fiber laser mode-locked with a black phosphorus saturable absorber," *Laser Phys. Lett.*, vol. 13, no. 9, p. 095104, 2016.
[213] Z.-C. Luo *et al.*, "Microfiber-based few-layer black phosphorus saturable absorber for ultra-fast fiber laser," *Opt. Express*, vol. 23, no. 15, pp. 20030–20039, Jul. 2015.
[214] X. Su *et al.*, "Femtosecond solid-state laser based on a few-layered black phosphorus saturable absorber," *Opt. Lett.*, vol. 41, no. 9, pp. 1945–1948, May 2016.
[215] Z.-C. Luo *et al.*, "2 GHz passively harmonic mode-locked fiber laser by a microfiber-based topological insulator saturable absorber," *Opt. Lett.*, vol. 38, no. 24, p. 5212, Dec. 2013.
[216] L. Gao, T. Zhu, W. Huang, and Z. Luo, "Stable, Ultrafast Pulse Mode-Locked by Topological Insulator $\rm Bi_2\rm Se_3 $ Nanosheets Interacting With Photonic Crystal Fiber: From Anomalous Dispersion to Normal Dispersion," *IEEE Photonics J.*, vol. 7, no. 1, pp. 1–8, Feb. 2015.
[217] H.-R. Chen *et al.*, "High-quality and Large-size Topological Insulator Bi_2Te_3-Gold Saturable Absorber Mirror for Mode-Locking Fiber Laser," *Sci. Rep.*, vol. 6, p. srep38444, Dec. 2016.
[218] L. Li, Y. Wang, X. Wang, T. Lin, and H. Sun, "High energy mode-locked Yb-doped fiber laser with Bi2Te3 deposited on tapered-fiber," *Opt. - Int. J. Light Electron Opt.*, vol. 142, pp. 470–474, Aug. 2017.
[219] J. Lee, J. Koo, Y. M. Jhon, and J. H. Lee, "A femtosecond pulse erbium fiber laser incorporating a saturable absorber based on bulk-structured Bi_2Te_3 topological insulator," *Opt. Express*, vol. 22, no. 5, pp. 6165–6173, Mar. 2014.
[220] M. Kowalczyk *et al.*, "Sb_2Te_3-deposited D-shaped fiber as a saturable absorber for mode-locked Yb-doped fiber lasers," *Opt. Mater. Express*, vol. 6, no. 7, pp. 2273–2282, Jul. 2016.

[221] J. Sotor, G. Sobon, W. Macherzynski, and K. M. Abramski, "Harmonically mode-locked Er-doped fiber laser based on a Sb_2Te_3 topological insulator saturable absorber," *Laser Phys. Lett.*, vol. 11, no. 5, p. 055102, 2014.
[222] K. Wu *et al.*, "High-performance mode-locked and Q-switched fiber lasers based on novel 2D materials of topological insulators, transition metal dichalcogenides and black phosphorus: review and perspective (invited)," *Opt. Commun.*
[223] R. Wei *et al.*, "Ultra-broadband nonlinear saturable absorption of high-yield MoS 2 nanosheets," *Nanotechnology*, vol. 27, no. 30, p. 305203, 2016.
[224] H. Yu *et al.*, "Topological insulator as an optical modulator for pulsed solid-state lasers," *Laser Photonics Rev.*, vol. 7, no. 6, pp. L77–L83, Nov. 2013.
[225] Z. Wang, H. Mu, C. Zhao, Q. Bao, and H. Zhang, "Harmonic mode-locking and wavelength-tunable Q-switching operation in the graphene–Bi2Te3 heterostructure saturable absorber-based fiber laser," *Opt. Eng.*, vol. 55, no. 8, pp. 081314–081314, 2016.
[226] J. Liu *et al.*, "Polarization domain wall pulses in a microfiber-based topological insulator fiber laser," *Sci. Rep.*, vol. 6, p. srep29128, Jul. 2016.
[227] J. Lee, J. Lee, J. Koo, H. Chung, and J. H. Lee, "Linearly polarized, Q-switched, erbium-doped fiber laser incorporating a bulk-structured bismuth telluride/polyvinyl alcohol saturable absorber," *Opt. Eng.*, vol. 55, no. 7, pp. 076109–076109, 2016.
[228] C. A. Zaugg *et al.*, "Ultrafast and widely tuneable vertical-external-cavity surface-emitting laser, mode-locked by a graphene-integrated distributed Bragg reflector," *Opt. Express*, vol. 21, no. 25, pp. 31548–31559, Dec. 2013.
[229] T. R. Schibli, E. R. Thoen, F. X. Kärtner, and E. P. Ippen, "Suppression of Q-switched mode locking and break-up into multiple pulses by inverse saturable absorption," *Appl. Phys. B*, vol. 70, no. 1, pp. S41–S49, Jun. 2000.
[230] A. Marini, J. D. Cox, and F. J. G. de Abajo, "Theory of graphene saturable absorption," *Phys. Rev. B*, vol. 95, no. 12, Mar. 2017.
[231] H.-R. Chen, C.-Y. Tsai, H.-M. Cheng, K.-H. Lin, and W.-F. Hsieh, "Passive mode locking of ytterbium- and erbium-doped all-fiber lasers using graphene oxide saturable absorbers," *Opt. Express*, vol. 22, no. 11, pp. 12880–12889, Jun. 2014.
[232] T. Mueller, F. Xia, and P. Avouris, "Graphene photodetectors for high-speed optical communications," *Nat. Photonics*, vol. 4, no. 5, pp. 297–301, May 2010.
[233] M. Liu *et al.*, "A graphene-based broadband optical modulator," *Nature*, vol. 474, no. 7349, pp. 64–67, Jun. 2011.
[234] J. T. Kim and C.-G. Choi, "Graphene-based polymer waveguide polarizer," *Opt. Express*, vol. 20, no. 4, pp. 3556–3562, Feb. 2012.
[235] Y. Shao, J. Wang, H. Wu, J. Liu, I. A. Aksay, and Y. Lin, "Graphene Based Electrochemical Sensors and Biosensors: A Review," *Electroanalysis*, vol. 22, no. 10, pp. 1027–1036, May 2010.
[236] X. Wang, L. Zhi, and K. Müllen, "Transparent, Conductive Graphene Electrodes for Dye-Sensitized Solar Cells," *Nano Lett.*, vol. 8, no. 1, pp. 323–327, Jan. 2008.
[237] A. H. Castro Neto, F. Guinea, N. M. R. Peres, K. S. Novoselov, and A. K. Geim, "The electronic properties of graphene," *Rev. Mod. Phys.*, vol. 81, no. 1, pp. 109–162, Jan. 2009.
[238] Q. Bao *et al.*, "Atomic-Layer Graphene as a Saturable Absorber for Ultrafast Pulsed Lasers," *Adv. Funct. Mater.*, vol. 19, no. 19, pp. 3077–3083, Oct. 2009.
[239] Q. Bao *et al.*, "Monolayer graphene as a saturable absorber in a mode-locked laser," *Nano Res.*, vol. 4, no. 3, pp. 297–307, Mar. 2011.
[240] H. Zhang, D. Y. Tang, L. M. Zhao, Q. L. Bao, and K. P. Loh, "Large energy mode locking of an erbium-doped fiber laser with atomic layer graphene," *Opt. Express*, vol. 17, no. 20, p. 17630, Sep. 2009.

[241] Z. Sun *et al.*, "Graphene Mode-Locked Ultrafast Laser," *ACS Nano*, vol. 4, no. 2, pp. 803–810, Feb. 2010.
[242] H. Ahmad, F. D. Muhammad, M. Z. Zulkifli, and S. W. Harun, "Graphene-Oxide-Based Saturable Absorber for All-Fiber Q-Switching With a Simple Optical Deposition Technique," *IEEE Photonics J.*, vol. 4, no. 6, pp. 2205–2213, Dec. 2012.
[243] G. Sobon, J. Sotor, and K. M. Abramski, "Passive harmonic mode-locking in Er-doped fiber laser based on graphene saturable absorber with repetition rates scalable to 2.22 GHz," *Appl. Phys. Lett.*, vol. 100, no. 16, p. 161109, Apr. 2012.
[244] G. Q. Xie *et al.*, "Graphene saturable absorber for Q-switching and mode locking at 2 μm wavelength [Invited]," *Opt. Mater. Express*, vol. 2, no. 6, pp. 878–883, Jun. 2012.
[245] M. Han, S. Zhang, X. Li, H. Zhang, H. Yang, and T. Yuan, "Polarization dynamic patterns of vector solitons in a graphene mode-locked fiber laser," *Opt. Express*, vol. 23, no. 3, pp. 2424–2435, Feb. 2015.
[246] L. B. Modesto-López, M. Miettinen, T. Torvela, A. Lähde, and J. Jokiniemi, "Direct deposition of graphene nanomaterial films on polymer-coated glass by ultrasonic spraying," *Thin Solid Films*, vol. 578, pp. 45–52, Mar. 2015.
[247] J. Park, K. Park, D. Spoor, B. Hall, and Y.-W. Song, "Hand-manageable graphene sticker for ultrafast mode-locked fiber lasers," *Opt. Express*, vol. 23, no. 6, p. 7940, Mar. 2015.
[248] G. Sobon, "Mode-locking of fiber lasers using novel two-dimensional nanomaterials: graphene and topological insulators [Invited]," *Photonics Res.*, vol. 3, no. 2, p. A56, Apr. 2015.
[249] X. M. Liu *et al.*, "Graphene-clad microfibre saturable absorber for ultrafast fibre lasers," *Sci. Rep.*, vol. 6, p. 26024, May 2016.
[250] R. M. Gerosa, D. Steinberg, F. N. Pellicer, S. H. Domingues, T. A. D. Souza, and L. A. Saito, "300-fs mode-locked Erbium doped fiber laser using evanescent field interaction through graphene oxide saturable absorber in D-shaped fibers," in *Latin America Optics and Photonics Conference (2016), paper LTh2A.5*, 2016, p. LTh2A.5.
[251] Z.-C. Luo, W.-J. Cao, A.-P. Luo, and W.-C. Xu*, "Optical Deposition of Graphene Saturable Absorber Integrated in a Fiber Laser Using a Slot Collimator for Passive Mode-Locking," *Appl. Phys. Express*, vol. 5, no. 5, p. 055103, May 2012.
[252] T. Chen, H. Chen, and D. N. Wang, "Graphene Saturable Absorber Based on Slightly Tapered Fiber With Inner Air-Cavity," *J. Light. Technol.*, vol. 33, no. 11, pp. 2332–2336, Jun. 2015.
[253] P. Mouchel, G. Semaan, A. Niang, M. Salhi, M. Le Flohic, and F. Sanchez, "High power passively mode-locked fiber laser based on graphene nanocoated optical taper," *Applied Physics Letters*, p. In progress, 2017.
[254] T. A. Birks and Y. W. Li, "The shape of fiber tapers," *J. Light. Technol.*, vol. 10, no. 4, pp. 432–438, 1992.
[255] S. W. Harun, K. S. Lim, C. K. Tio, K. Dimyati, and H. Ahmad, "Theoretical analysis and fabrication of tapered fiber," *Opt. - Int. J. Light Electron Opt.*, vol. 124, no. 6, pp. 538–543, Mar. 2013.
[256] A. J. Fielding, K. Edinger, and C. C. Davis, "Experimental observation of mode evolution in single-mode tapered optical fibers," *J. Light. Technol.*, vol. 17, no. 9, pp. 1649–1656, Sep. 1999.
[257] D. T. Cassidy, D. C. Johnson, and K. O. Hill, "Wavelength-dependent transmission of monomode optical fiber tapers," *Appl. Opt.*, vol. 24, no. 7, pp. 945–950, Apr. 1985.
[258] G. Xing, H. Guo, X. Zhang, T. C. Sum, and C. H. A. Huan, "The Physics of ultrafast saturable absorption in graphene," *Opt. Express*, vol. 18, no. 5, pp. 4564–4573, Mar. 2010.
[259] R. W. Newson, J. Dean, B. Schmidt, and H. M. van Driel, "Ultrafast carrier kinetics in exfoliated graphene and thin graphite films," *Opt. Express*, vol. 17, no. 4, pp. 2326–2333, Feb. 2009.

[260] J. M. Dawlaty, S. Shivaraman, M. Chandrashekhar, F. Rana, and M. G. Spencer, "Measurement of Ultrafast Carrier Dynamics in Epitaxial Graphene," *Appl. Phys. Lett.*, vol. 92, no. 4, p. 042116, Jan. 2008.
[261] R. R. Nair *et al.*, "Fine Structure Constant Defines Visual Transparency of Graphene," *Science*, vol. 320, no. 5881, pp. 1308–1308, Jun. 2008.
[262] D. Popa, Z. Sun, F. Torrisi, T. Hasan, F. Wang, and A. C. Ferrari, "Sub 200 fs pulse generation from a graphene mode-locked fiber laser," *Appl. Phys. Lett.*, vol. 97, p. 203106, Nov. 2010.
[263] M. Hajlaoui *et al.*, "Ultrafast Surface Carrier Dynamics in the Topological Insulator Bi_2Te_3," *Nano Lett.*, vol. 12, no. 7, pp. 3532–3536, Jul. 2012.
[264] N. Kumar *et al.*, "Spatially resolved femtosecond pump-probe study of topological insulator Bi_2Se_3," *Phys. Rev. B*, vol. 83, no. 23, p. 235306, Jun. 2011.
[265] D. Hsieh, F. Mahmood, J. W. McIver, D. R. Gardner, Y. S. Lee, and N. Gedik, "Selective probing of photo-induced charge and spin dynamics in the bulk and surface of a topological insulator," *Phys. Rev. Lett.*, vol. 107, no. 7, Aug. 2011.
[266] J. E. Moore, "The birth of topological insulators," *Nature*, vol. 464, no. 7286, pp. 194–198, Mar. 2010.
[267] J. Moore, "Topological insulators: The next generation," *Nat. Phys.*, vol. 5, no. 6, pp. 378–380, Jun. 2009.
[268] D. Kong *et al.*, "Few-Layer Nanoplates of Bi_2Se_3 and Bi_2Te_3 with Highly Tunable Chemical Potential," *Nano Lett.*, vol. 10, no. 6, pp. 2245–2250, Jun. 2010.
[269] L. Fidkowski, "Entanglement spectrum of topological insulators and superconductors," *Phys. Rev. Lett.*, vol. 104, no. 13, Apr. 2010.
[270] H. Zhang, C.-X. Liu, X.-L. Qi, X. Dai, Z. Fang, and S.-C. Zhang, "Topological insulators in Bi_2Se_3, Bi_2Te_3 and Sb_2Te_3 with a single Dirac cone on the surface," *Nat. Phys.*, vol. 5, no. 6, pp. 438–442, Jun. 2009.
[271] null Kulbachinskii *et al.*, "Valence-band energy spectrum of solid solutions of narrow-gap-semiconductor Bi_2-xSnxTe_3 single crystals," *Phys. Rev. B Condens. Matter*, vol. 50, no. 23, pp. 16921–16930, Dec. 1994.
[272] Y. Wang *et al.*, "Ultra-broadband Nonlinear Saturable Absorption for Two-dimensional $Bi_2Te_xSe_{3-x}$ Nanosheets," *Sci. Rep.*, vol. 6, p. srep33070, Sep. 2016.
[273] S. Lu *et al.*, "Third order nonlinear optical property of Bi_2Se_3," *Opt. Express*, vol. 21, no. 2, p. 2072, Jan. 2013.
[274] C. Zhao *et al.*, "Wavelength-tunable picosecond soliton fiber laser with Topological Insulator: Bi_2Se_3 as a mode locker," *Opt. Express*, vol. 20, no. 25, p. 27888, Dec. 2012.
[275] L. Ren *et al.*, "Large-scale production of ultrathin topological insulator bismuth telluride nanosheets by a hydrothermal intercalation and exfoliation route," *J. Mater. Chem.*, vol. 22, no. 11, p. 4921, 2012.
[276] S. M. Block, "Making light work with optical tweezers," *Nature*, vol. 360, no. 6403, pp. 493–495, Dec. 1992.
[277] Y. Meng, M. Salhi, A. Niang, K. Guesmi, G. Semaan, and F. Sanchez, "Mode-locked Er:Yb-doped double-clad fiber laser with 75-nm tuning range," *Opt. Lett.*, vol. 40, no. 7, pp. 1153–1156, Apr. 2015.
[278] G.-R. Lin, J.-Y. Chang, Y.-S. Liao, and H.-H. Lu, "L-band erbium-doped fiber laser with coupling-ratio controlled wavelength tunability," *Opt. Express*, vol. 14, no. 21, p. 9743, 2006.
[279] G.-R. Lin and J.-Y. Chang, "Femtosecond mode-locked Erbium-doped fiber ring laser with intra-cavity loss controlled full L-band wavelength tunability," *Opt. Express*, vol. 15, no. 1, pp. 97–103, Jan. 2007.

[280] H. Lin, C. Guo, S. Ruan, and J. Yang, "Dissipative soliton resonance in an all-normal-dispersion Yb-doped figure-eight fibre laser with tunable output," *Laser Phys. Lett.*, vol. 11, no. 8, p. 085102, 2014.

UNIVERSITE BRETAGNE LOIRE

université angers

Thèse de Doctorat

Georges SEMAAN

Dynamiques des solitons dans les lasers à fibre: du soliton dissipatif jusqu'à la résonance

Soliton dynamics in fiber lasers: from dissipative soliton to dissipative soliton resonance

Résumé

Dans cette thèse, nous étudions expérimentalement la génération d'impulsions carrées très énergétiques et accordable à l'échelle nanosecondes et d'impulsions ultra-courtes à haute puissance moyenne de sortie dans les lasers à fibre utilisant les nanomatériaux comme absorbant saturable. Tout d'abord, puisque la dynamique des impulsions est dominée par l'interaction de la non linéarité et de la dispersion chromatique cubique de la fibre avec un mécanisme de discrimination d'intensité appelé absorbant saturable, la stabilité d'une distribution harmonique en mode verrouillé est étudiée par injection externe d'une onde continue.

Deuxièmement, une étude expérimentale de la génération des impulsions carrées très énergétiques est mise en évidence. Deux cavités laser ont été construites, l'une basée sur la rotation non linéaire de la polarisation RNLP et l'autre sur le miroir à boucle non linéaire amplifiée (NALM) en configuration laser en forme de huit. Avec la RNLP, nous avons démontré la génération d'impulsions carrées fonctionnant dans le régime de la résonance des solitons dissipatifs (DSR), ayant 2,27 µJ comme énergie avec une durée accordable dans les nanosecondes. Dans la configuration NALM, nous avons présenté la possibilité d'émettre des impulsions carrées DSR jusqu'à 10 µJ d'énergie par impulsion tout en contrôlant la durée et la puissance crête. On aussi mis en évidence qu'en modifiant les paramètres de la cavité, des instabilités pourraient se produire, formant une répartition harmonique des impulsions carrées dans un cas et modifiant la structure de l'impulsion carrée dans d'autres cas pour générer des impulsions d'escalier.

Enfin, nous avons utilisés des absorbant saturable à base de nanomatériaux déposés sur des tapers optiques dans les lasers à fibre pour générer des impulsions ultra-courtes avec une puissance de sortie moyenne élevée.

Mots clés

Optique non linéaire, lasers à fibre, génération d'impulsions ultra-courtes, résonance de soliton dissipative, impulsions à haute énergie, graphène, tapers optiques, blocage de mode, isolants topologiques, stabilité

Abstract

In this thesis, we investigate experimentally the generation of high energy nanosecond tunable square pulses and high output power ultrashort pulses in fiber lasers. First, since pulse dynamics are dominated by the interaction of the fiber's cubic Kerr nonlinearity and chromatic dispersion with an intensity-discriminating mechanism referred to as a saturable absorber, the stability of a harmonic mode-locked distribution is studied by external injection of a continuous wave.

Second, a comprehensive study of energy scaling in fiber laser cavities mode-locked by a saturable absorber is presented in this thesis. Two laser cavities have been constructed, one based on the non-linear polarization evolution (NPE) and the other based on the nonlinear amplified loop mirror (NALM) in a figure-eight laser configuration. With the NPE, we demonstrated the generation of 2.27 µJ energy square pulses in the nanoseconds range operating in the dissipative soliton resonance DSR. In the NALM configuration and while using dual amplifiers, we presented the possibility of emitting up to 10 µJ of width and peak power tunable DSR square pulses. However, it is shown that by modifying the cavity parameters, multi-pulsing instabilities could occur in such cavities, forming a harmonic distribution of square pulses in one case, and modifying the structure of the square pulse in other cases to generate staircase pulses.

Finally, we implemented nanomaterial based saturable absorbers in fiber laser configuration to generate ultrashort pulses with high average output power. Different techniques of achieving such components are explicitly detailed: ultrashort pulse generation in ring cavities where graphene and topological insulators are deposited on optical tapers to form a saturable absorber.

Key Words

Nonlinear optics, Fiber lasers, ultra-short pulse generation, dissipative soliton resonance, high energy pulses, graphene, optical tapers, mode-locking, topological insulators, optical stability.